TÉCNICO LISBOA

Inverse Dynamics of a Swimmer Multibody Model: An Analysis of the Lower Limbs During Front Crawl

Mariana Fabião Ribeiro de Brito Sequeira

Thesis to obtain the Master of Science Degree in

Mechanical Engineering

Supervisors: Prof. Carlos Miguel Fernandes Quental

Prof. João Paulo Vilas-Boas Soares Campos

Examination Committee

Chairperson: Prof. Paulo Rui Alves Fernandes

Supervisor: Prof. Carlos Miguel Fernandes Quental

Member of the Committee: Prof. Leandro José Rodrigues Machado

January 2021

Abstract

The aim of this study is to propose a full body model representation of the human body to conduct an inverse dynamic analysis of the lower limbs during swimming activities. Considering multibody dynamics, a three-dimensional biomechanical model using Cartesian coordinates is presented. The anatomical articulations are approximated by ideal kinematic joints, which are controlled by rotational driver actuators.

Kinematic data were collected at the Porto Biomechanics Laboratory for a front crawl swimming stroke and external forces describing the interactions between the human body and surrounding environment were estimated using a computer simulation method available in the literature. An interface between the full body biomechanical model and the simulation software is developed to perform (1) the conversion of body geometry specifications and motion data, that is given as input to the simulation, and (2) the processing of the simulation output data containing the external forces, that are addressed to the full body model. Inverse dynamic analyses are performed considering the full body biomechanical model actuated upon by driver actuators, referred to as determinate problem, to evaluate the joint torques and intersegmental joint forces acting on the human lower limbs.

The kinematic results, which are generally in good agreement with the literature, show the alternate rhythmical movement upwards and downwards performed by the lower limbs. However, as far as the interface developed is concerned, the results show some discrepancies on the force magnitudes acting upon the feet during some phases of the stroke cycle. It is expected that these discrepancies have impact on the intersegmental joint forces and joint torques of the lower limbs, although the lack of literature in this field of research does not allow a complete validation of results. Nevertheless, the results of the determinate problem are presented and discussed for the anatomical joints of the human lower limbs.

Keywords: Biomechanics, Front crawl stroke, Hydrodynamic forces, Inverse dynamics, Joint torques, Lower limbs, Multibody dynamics, Swimming analysis.

Resumo

Neste trabalho é desenvolvido um modelo completo do corpo humano para realizar a análise dinâmica inversa de um movimento de natação. No contexto de dinâmica multicorpo, é apresentado um modelo biomecânico tridimensional cuja formulação utiliza coordenadas Cartesianas. As articulações anatómicas são representadas por juntas mecânicas, cujos graus de liberdade são controlados por atuadores de junta ao longo do movimento realizado. Embora a análise seja conduzida para o corpo humano completo, este estudo foca-se apenas na dinâmica nos membros inferiores.

A recolha de dados cinemáticos do movimento de natação *crawl* foi realizada no Laboratório de Biomecânica da Universidade do Porto. Relativamente às forças externas, no contexto de natação estas correspondem às interações mútuas entre o corpo em movimento e o meio envolvente. Uma vez que não é possível utilizar placas de força para medir as forças instantâneas e respetivos pontos de aplicação, as forças hidrodinâmicas foram obtidas através de um programa computacional de simulação disponível na literatura. Para isso, foi desenvolvida uma interface entre o modelo biomecânico em estudo e o programa de simulação de forma a realizar (1) a conversão dos dados geométricos e cinemática do modelo que representa o corpo humano, de forma a assegurar a correspondência correta dos mesmos, e (2) o processamento dos dados que resultam da simulação, que correspondem às forças externas aplicadas sobre o corpo. É então realizada a análise dinâmica inversa com atuadores de juntas, que permite a obtenção das forças e momentos intersegmentares dos membros inferiores.

Os resultados da análise cinemática mostram-se concordantes com a literatura. Estes permitem aferir quanto ao movimento rítmico alternado dos membros inferiores, descrito como batidas sucessivas ascendentes e descendentes. No que diz respeito à interface implementada, durante algumas fases do ciclo de *crawl*, a magnitude das forças externas obtidas nos pés através do programa de simulação revela discrepância relativamente ao valor que seria esperado encontrar. É possível que estas divergências tenham posteriormente impacto nos resultados da análise dinâmica inversa, apesar de não ser possível concluir quanto à validade dos mesmos dada a falta de literatura nesta área. De qualquer forma, os valores obtidos para as forças intersegmentares e momentos articulares são apresentados e discutidos para as articulações dos membros inferiores.

Palavras-chave: Biomecânica, Técnica de nado *crawl*, Forças hidrodinâmicas, Dinâmica inversa, Momentos articulares, Membros inferiores, Dinâmica de sistemas multicorpo, Análise de natação.

Acknowledgments

Aos Professores Carlos Quental, João Paulo Vilas-Boas e Jorge Ambrósio. Um acompanhamento e suporte absolutamente incansáveis e estimulantes. Por me terem dado a oportunidade de trabalhar numa área que se tem revelado fascinante para mim. Por terem alimentado uma disciplina e compromisso entre todo o grupo de trabalho desde o primeiro dia. Ao Professor Carlos Quental, pela paciência (enorme!) e serenidade. Pela disponibilidade total, e por me ajudar a manter os pés bem assentes no chão quando a preocupação e angústia gritaram mais alto. Ao Professor Jorge Ambrósio, apesar de não ser meu orientador científico, pela boa disposição e energia durante as manhãs de reunião, pelo gosto de conversar e pensar, e pelas viagens mundo feitas no seu ecrã de computador. Ao Professor João Paulo Vilas-Boas e ao Engenheiro Pedro Fonseca, do LABIOMEP-UP, que apesar das voltas que este ano nos deu, e que impossibilitou a tão desejada ida ao Porto, em vez alguma se viu comprometida a total disponibilidade por parte de ambos no esclarecimento de dúvidas.

To Professor Motomu Nakashima from the Tokyo Institute of Technology, I would like to thank the support and the authorisation to use the images of the Swumsuit force model in this dissertation.

À Kika, que no último dia de inscrições, do último semestre, do último ano do curso, me sugeriu a UC de Biomecânica do Movimento. E isso, como se vê, ditou tudo daí para a frente. Mas mais ainda, pela companhia e suporte mútuo nas reuniões quase diárias via Skype durante uns bons meses, quando o mundo quase parou, e esta foi a melhor, e única, forma possível de puxarmos uns pelos outros. O hit de verão 2020 nunca será esquecido! E aos tantos amigos que o curso me deu (ou me trouxe de volta da infância), em especial à Xana, Alda, Chico, Hélder (e heterónimos!), Diogo, Pinho, Mariana. Que bom que isto foi com vocês por perto.

À Mariana e ao Vasco. Que, sobretudo nesta fase, me mostraram sempre tanto apoio e conforto.

À Adriana, desde o dia um. Que num segundo mudou toda e qualquer ideia que eu poderia ter tirado daquela franjinha e sapato raso na lama do Arco do Cego, naquilo que era o primeiro dia de “aulas” de faculdade. Mas que agora não troco nem por nada. Vou contigo até à última edição de Ramalhete, seja onde for. E à Carolina, que um ano mais tarde, no mesmo lugar, nos veio mostrar que não há duas sem três. De cara (quase sempre) trancada, mas que das melhores sabe o que me vai na cabeça.

Ao Pedro, que tomou todos os meus desafios como os dele. Que nunca me deixou baixar armas, que acreditou sempre, e com tanta força. Pelo carinho, paciência e motivação.

À Mariana (a primeira de todas na minha vida). A amiga-casa, com quem cresci, e que muitas vezes sabe melhor de mim do que eu própria. A mais paciente e generosa das pessoas.

Por fim, à minha família, porque são o apoio de sempre, de todas as circunstâncias, e de todos os lugares. Mãe, Pai, Carolina, Pedro, Miguel, Avó, e ao mais recente membro que em tão pouco tempo já nos pertence há tanto, Joaquim. Um por todos, e todos por um. Sempre.

Obrigada a vocês. Vai deixar muitas saudades.

Contents

List of Figures

List of Tables

List of Acronyms

AC	Acromion
APW	Anterior pelvic width
ARP	Anatomical reference position
ASIS	Anterior superior iliac spine
BSIP	Body segment inertial parameter
C7	7th cervical vertebrae
CFD	Computational Fluid Dynamics
CJC	Cervical joint centre
COM	Centre of mass
DOF	Degrees of freedom
FD	Finite Differences
FEM	Finite Element Method
GUI	Graphical User Interface
HJC	Hip joint centre
ISB	International Society of Biomechanics
LABIOMEP-UP	Porto Biomechanics Laboratory (University of Porto)
LHBM	Lisbon Human Body Model
LJC	Lumbar joint centre
LL	Leg length
MA	Medial malleolus
MK	Medial epicondyle of the femur
OJC	Atlanto-occipital joint centre
PD	Pelvic depth
PSIS	Posterior superior iliac spine
SJC	Shoulder joint centre
SPH	Smoothed-Particle Hydrodynamics
ST1	Sternum cluster marker 1
SWUM	Swimming Human Model
Swumsuit	Swimming Human Model with Synthetic User Interface Tools

List of Symbols

Convention

a, A, α	Scalar
$\mathbf{a}$	Vector
$\mathbf{A}$	Matrix

Over script

$\dot{\mathbf{a}}$	First time derivative
$\ddot{\mathbf{a}}$	Second time derivative
$\tilde{\mathbf{a}}$	3×3 skew-symmetric matrix

Superscript

$\mathbf{a}^{\mathrm{T}}, \mathbf{A}^{\mathrm{T}}$	Transpose of a vector or matrix
$\mathbf{a}'$	Quantity expressed in the body-fixed (or local) reference frame

Latin Symbols

$\mathbf{A}_i$	Rotation matrix for body *i*
C_a	Added mass coefficient
C_D	Drag coefficient
C_L	Lift coefficient
C_m	Inertial coefficient
$\mathbf{G}_i$	3×4 global transformation matrix for body *i*
$\mathbf{I}$	Identity matrix
$\mathbf{L}_i$	3×4 local transformation matrix for body *i*
$\mathbf{M}$	Mass matrix for a system
$\mathbf{q}, \dot{\mathbf{q}}, \ddot{\mathbf{q}}$	Vector of generalised coordinates, velocities, and accelerations
X, Y, Z	Global Cartesian coordinates (LHBM)
x, y, z	Absolute coordinate system (SWUM)
x_b, y_b, z_b	Body coordinate system (SWUM)
x_c, y_c, z_c	Camera coordinate system (SWUM)

Greek Symbols

$\boldsymbol{\gamma}$	Right-hand side vector of the acceleration constraint equations
$\boldsymbol{\lambda}$	Vector of Lagrange multipliers
$\boldsymbol{\nu}$	Right-hand side vector of the velocity constraint equations
ρ	Density of the fluid
$\boldsymbol{\Phi}$	Generalised vector of constraints
$\boldsymbol{\Phi_q}$	Jacobian matrix of the constraints
$\boldsymbol{\omega}$	Angular velocity vector
$\dot{\boldsymbol{\omega}}$	Angular acceleration vector
ξ, η, ζ	Body-fixed (or local) coordinates (LHBM)

1. Introduction

1.1. Motivation and Objectives

Biomechanics is the field of science that describes, analyses, and assesses the physiology of living structures and animals using the laws of mechanics. Human motion is one of the objects of study in biomechanics (Winter, 2009), which involves complex interactions between the neuromuscular and skeletal systems. Understanding these interactions is necessary for the diagnosis and treatment of patients with motor deficiencies and to enhance performance of able-bodied individuals (Rajagopal et al., 2016).

While some components of human motion, such as body segment kinematics, ground reaction forces, and muscle activity can be measured using non-invasive tools including motion capture systems, force plates, and electromyography, more invasive means are necessary to measure muscle-tendon (Ishikawa et al., 2005) and joint contact forces (Bergmann et al., 2001). Computational biomechanical models based on multibody dynamics are powerful tools that enable the evaluation of these quantities in the human body, whose *in vivo* or *in vitro* measurement is, when possible, extremely difficult (Quental et al., 2015). In the context of human swimming, current biomechanical models are mostly based on simplified models of specific parts of the human body (Cohen et al., 2015; Lauer et al., 2016). Due to limitations on motion acquisition, especially in the air-water interface, they are kept simple and are hardly able to simulate the broad range of motion of many of the anatomical segments relevant to swimming. Another fundamental data for the evaluation of internal forces are the external forces acting on the human body during swimming, herein referred to as hydrodynamic forces, which cannot be acquired with sufficient accuracy using current experimental methods (Takagi et al., 2015). These shortcomings limit the evaluation of the internal forces in the human body, even when only joint torques are required.

This work aims to contribute to the development of more representative biomechanical models focused on the dynamics of human swimming motion, by combining different fields of knowledge, such as the biomechanics, medical sciences, sports performance, and fluid dynamics. The main objective of the present dissertation is to evaluate the dynamic response of the multibody system of the human lower limbs during a six-beat front crawl swimming motion. To achieve this, a three-dimensional full body biomechanical model of the human body is proposed, the Lisbon Human Body Model (LHBM). The modelling anthropometric measurements are given as input to the inverse dynamic analysis program alongside the motion kinematic and kinetic data of the subject under analysis. The multibody system representing the entire human body is actuated upon by joint torques. However, the determination of the kinetic data in the context of human swimming cannot be obtained by means of conventional tools, such as force plates. Instead, the hydrodynamic forces exerted in the human subject during the stroke cycle are accounted for using a simulation software available in the literature, the Swimming Human Model with Synthetic User Interface Tools (Swumsuit) (Nakashima et al., 2007). The second aim of this work is to develop an interface between the simulation software and the LHBM that performs the

adjustment on the software inputs and outputs to properly fit the characteristics between the LHBM and the simulation Swimming Human Model (SWUM). The interface is developed on a general basis to allow future studies to be conducted for front crawl or any other swimming technique supported by Swumsuit.

1.2. State of the Art

Modelling human body motion requires the understanding of biological and physical principles that provide a realistic representation of the mechanical behaviour of living systems. The ability to predict how the whole body moves and how it exchanges forces with the surrounding has been shown to provide valuable information in areas such as orthopaedics, ergonomics, forensics, sports science, and medical rehabilitation (Xiao and Fu, 2016). The potential of this type of analysis is ever increasing as, over the last decades, with the increase in computational power, numerical models of the human body have undergone enormous improvements (Rajagopal et al., 2016).

1.2.1. Multibody Biomechanical Modelling

Musculoskeletal models support with data computational methodologies instrumented for biomechanical analysis, in which the skeletal system consisting of rigid body segments connected by kinematic joints moves their body according to a dynamic activation of sets of muscles. When the modelling does not contemplate the muscle apparatus system, these are simply referred to as biomechanical or multibody models. Human biomechanical models can cover the whole body modelling (Rajagopal et al., 2016; Silva and Ambrósio, 2003) or only a part of it (Horsman et al., 2007; Quental et al., 2015). The mathematical formulation and level of discretisation of the biomechanical model depend upon the area of research, the objective of the analysis, and the results expected (Silva, 2003). For instance, finite element methods are usually used to analyse in detail the localised structural deformations or the mechanical behaviour of structures (Quental, 2013). On the other hand, multibody models are well suited to conduct large body displacements and complex interactions with the surrounding (Silva, 2003).

The study of multibody systems is particularly useful in the prediction of the mechanical behaviour of the human body during daily activities, providing valuable information concerning the intersegmental joint contact forces between the rigid bodies that compose the biomechanical system. These results can be obtained either by a forward or an inverse dynamic analysis. In a forward dynamic analysis, the motion is predicted when the applied forces and torques are known, whereas in an inverse dynamic analysis the intersegmental forces are predicted for a prescribed or acquired motion. Despite both types of analyses being attractive in the study of the upper limb dynamics, most models, including the one presented in this work, mainly focus on inverse dynamic analyses because they are much more efficient computationally (Quental, 2013).

A large number of biomechanical models are available in the literature. Horsman et al. (2007) and Cleather and Bull (2015) developed a complete dataset of the human lower limbs. Commercial programs, such as the AnyBody Modelling System (AnyBody Technology A/S, Aalborg, Denmark) (Lund et al., 2015) and the OpenSim (Simbios, Stanford, CA, USA) (Rajagopal et al., 2016) contain several modelling systems for a wide range of activities (Langholz et al., 2016). Quental et al. (2015) focus the

modelling on the detailed representation of the shoulder complex. Other studies model the full human body, mostly envisaging gait analysis (Pàmies-Vilà, 2012; Rajagopal et al., 2016; Silva, 2003). The modelling requirements of a biomechanical model mostly depend upon the motion under analysis and the available data. If the objective of the analysis only concerns the mechanical response of a specific limb, a partial description of the human body can be more efficient and less computational demanding than a whole-body description. Usually in swimming applications, due to the complexity of undertaking simulation analyses to determine the external forces, models are composed of detailed parts of the human body (Cohen et al., 2010; Lauer et al., 2016). Nevertheless, one purpose of this work is to implement a full body model that can be used to take into consideration the influence of the motion of the upper limbs and involve the results of the simulation of the hydrodynamic forces developed during swimming. Therefore, the anthropometric data of the biomechanical model applied is based on the dataset of Dumas et al. (2007a, 2007b). Dumas et al. (2007a) developed, for both males and females, a complete dataset of scaling equations for the computation of body segment inertial parameters (BSIPs), directly applicable in the conventional segment coordinate systems (Wu et al., 2002, 2005) and without restraining the position of the centre of mass (COM) and the orientation of the principal axes of inertia. The dataset of Dumas et al. (2007a) does not require further scaling procedures to match the characteristics of the anthropometric model and those of the subject whose kinematic data was collected.

1.2.2. Swimming Analysis

Human swimming is a highly competitive sport where performance has a complex dependence on technique, fluid dynamics, biomechanics, and physiology (Cohen et al., 2010). Several aspects contribute to enhance performance of swimming motion and prevent injury. A few essential components that help proper the swimming technique are related with body position, breathing pattern, stroke technique, fingers spacing, and wall turns (Hall, 2012; Wei et al., 2014). In order to quantity the effect of all these aspects, research have been made in the development of more kinematic and kinetic analyses of swimming motions.

Aquatic movements pose unique challenges with the medium of water increasing the complexity in the measurement of performance and by the continuously changing nature of the geometry of the human body (Honda et al., 2012). A swimmer moves forward using hydrodynamic forces created with their own movements in water, while locomotion on land uses ground reaction force (Matsuda et al., 2016). Unlike terrestrial motion where these ground reaction forces are easily measured using force platforms, the determination of the external forces in water is very difficult (Lauer et al., 2016). Takagi and Sanders (2002) computed the fluid forces acting on the swimmer's hand by direct pressure measurement. However, such tools only provide the hydrodynamic forces acting upon specific parts of the human body being inexistant today any experimental apparatus able to acquire the hydrodynamic forces on the complete human body during swimming activities.

Initial investigations into swimming propulsion were strictly experimental, and conducted for simplified models of specific parts of the human body (Jensen and McIlwain, 1979). However, all predictions were

limited by the fact that they tend to constraint several parameters, such as body geometry, motion data, or fluid properties. Over the last decades, the use of computational fluid dynamics (CFD) has emerged in aquatic locomotion research as a promising alternative of determining all the important quantities and thus provide insight into swimming hydrodynamics. CFD is a numerical simulation technique for solving the Navier-Stokes equations of fluid flow (Takagi et al., 2015). The advantage of CFD simulations in the context of human swimming lie in the treatment of (1) the complicated and transient movements of a flexible body shape in the water; (2) the dynamically changing shape, with rotations of many body segments about multiple axes; and (3) the large deformation of the water surface (Takagi et al., 2015). The first applications of CFD to swimming were conducted under steady state conditions of fixed bodies (Bixler and Riewald, 2002). However, with the arising interest of the scientific community over more complex swimming analyses, a variety of CFD simulations incorporating the moving body of the swimmer were developed: Von Loebbecke et al. (2009) computed the drag past a streamlined swimmer during dolphin kick; Keys (2010) studied several swimming techniques, namely the dolphin kick, the freestyle, or front crawl, and the freestyle and breaststroke kick considering the full body model; Samson et al. (2017) performed the simulation in front crawl swimming to analyse the propulsive forces generated by the hand and forearm; Lauer et al. (2016) simulated the underwater sculling motion of the upper limbs.

More recently, smoothed-particle hydrodynamics (SPH) methods emerged to answer to more complex questions regarding the splashing fluid effects and refractions at the free surface during swimming strokes, such as the front crawl swimming (Cleary et al., 2013; Cohen et al., 2009, 2015). However, computer simulation based on CFD and SPH methods is time-consuming not efficient to conduct large-scale parameter studies (Takagi et al., 2015). Therefore, an alternative computer simulation method that requires much less computation time has been developed by Nakashima et al. (2007). The simulation software, called Swumsuit, offers the possibility of conduct human swimming simulations without solving the flow field while still providing good results and considering the unsteady fluid effects. Swumsuit is a freely available software capable of perform simulations of various swimming motions, including the front crawl swimming, backstroke, breaststroke, among others (Nakashima et al., 2013; Takagi et al., 2015). These simulations have provided practical information for adjusting swimming movements and to enable swimmers to move faster and more efficiently. Moreover, Swumsuit was utilised not only for swimming performance analysis, but also for a transfemoral prosthesis of lower limb amputees (Nakashima et al., 2015). Of fundamental importance for the work developed in this dissertation is that Swumsuit estimates and outputs a representation of the hydrodynamic forces in all anatomical segments of the swimmer body model, thus providing the missing link for the inverse dynamic analysis.

1.2.3. Application Case

Fundamental quantities of interest in human motion research are the intersegmental forces and moments acting at the joints, which represent the net loads that act at each biomechanical joint. Due to the nature of human motion research, direct measurements techniques are rarely available and often inadequate to measure internal loading during activities of daily living and exercise (Derrick et al., 2020). The exception is the work of Bergmann et al. (2001) with instrumented prosthesis, but cannot be used

in a broad range of activities (Bergmann et al., 2001). Inverse dynamics analyses represent an alternative of estimate these quantities. To perform an inverse dynamic analysis, the motion of the multibody system must be known in advance as well as the externally applied forces so that the only unknowns are the internal forces of the system (Nikravesh, 1988).

For several swimming techniques, such as the front crawl stroke, the experimental data acquisition presents technical difficulties when compared with data acquisition for terrestrial motions. For instance, the air-water interface reduces marker visibility, and normal splashing produces a large amount of reflections that made tracking of some of the markers difficult (Andersen, 2019). Also, a recent work evaluated the changes in swimming motion performance and velocity induced by motion capture systems (Washino et al., 2019). Washino et al. (2019) showed that the effect of the reflective markers attached to the swimmer's surface reduces swimming velocity and produces drag, thus contributing negatively to swimming performance. Developments on the assessment of 3D motion kinematics specific to the area of swimming are expected to contribute to augment the analysis potential in the context of swimming (Ceccon et al., 2013; Honda et al., 2012).

In this work, the multibody biomechanical model of the full human body is applied in an inverse dynamics methodology to evaluate the intersegmental joint forces and joint torques of the human lower limbs during a front crawl swimming stroke. The kinematic data of the swimming motion performed by a male subject were provided by the Porto Biomechanics Laboratory (LABIOMEP-UP). The simulation software Swumsuit is used to estimate the external hydrodynamic forces during front crawl swimming.

Regarding the front crawl swimming stroke technique, the propulsive force is mainly created by the upper limbs, and thus the majority of studies in the literature have examined the movements of the upper limbs (Cohen et al., 2015; Harrison et al., 2014). The only study found in the literature in which the hip joint torques were determined for a front crawl swimming motion was developed by Nakashima et al. (2015). The work aimed to investigate the effect of knee joint motion on the swimming performance of an individual with a transfemoral prosthesis. Nevertheless, the contribution of the kicking action of the lower limbs is thought to improve the arm stroke technique, contribute to propulsion, and help to keep the body in a streamlined position, thus reducing the resistive drag (Gourgoulis et al., 2013). The present dissertation focuses on the analysis of the intersegmental forces and joint moments of the human lower limbs.

1.3. Dissertation Outline

This dissertation is organised in two main parts: the first part, Chapters 1 through 5, addresses the background literature, methods, and biomechanical data required for the dynamic analysis of swimming; the second part focuses on the kinetic data acquisition, or computation, and on the analysis of a swimming activity.

Chapter 1 introduces the background to the dissertation indicating the aims and general motivation behind the study, and reviews the current developments in biomechanical modelling, as well as in inverse dynamic analysis of biomechanical models in the context of swimming. Chapter 2 exposes the

work methodology to accomplish the dissertation's objectives. Chapter 3 describes the topology of the full-body biomechanical model, LHBM, and lists all the anatomical data of the human subject under analysis. Chapter 4 describes the principles for the implementation of the biomechanical model using a multibody formulation based on fully Cartesian coordinates. Chapter 5 outlines the methodology followed in the kinematic data acquisition of the swimming motion for a front crawl swimming stroke, and respective processing of data. The joint angles of the human lower limbs and the swimmer's body rotation about its longitudinal axis in terms of shoulder roll and hip roll are compared with the literature to validate the kinematic analysis and the biomechanical model formulation.

Chapter 6 addresses the computation of the hydrodynamic forces generated over the swimmer's body during swimming, using a simulation software Swumsuit developed by Nakashima et al. (2007). An interface between the simulation software and the biomechanical model presented in Chapter 3 is created to perform the conversion between modelling specifications. Some results of the fluid forces acting on the lower limbs are compared with Nakashima et al. (2007) to validate the applied methodology. Chapter 7 develops the determinate inverse dynamic analysis of the swimming motion. The degrees of freedom of the multibody system are actuated by driving joint actuators. A discussion of results regarding the intersegmental forces and joint torques obtained for the lower extremity of the biomechanical model is performed.

Chapter 8 summarises the thesis and addresses future developments in the field of human swimming. In Appendix A, the markers setup protocol used in the kinematic data acquisition is presented. Appendix B shows the layout of LABIOMEP-UP facilities, in which the experimental data acquisition was conducted. Appendix C contains the description of the input data files that are given to the simulation program to estimate the hydrodynamic forces.

1.4. Novel Aspects of the Work

The present dissertation develops a full body biomechanical model to study the human swimming motion of a front crawl swimming stroke. The biomechanical modelling data is based on the dataset of Dumas et al. (2007a, 2007b) that provides scaling equations for the computation of BSIPs. The work of Pàmies-Vilà (2012) is used to assess data for the head and neck, as two different body segments. The kinematic data acquisition was conducted in LABIOMEP-UP for a male subject and provided to the current work.

Regarding the front crawl swimming stroke, the role played by the upper and lower limbs is unbalanced since the upper limbs contribute with the most part of the total body propulsion (Guignard et al., 2019). Therefore, several studies in the literature are focused on the study of the arm stroke to understand the effects of fluid dynamics on the swimmer's performance. However, leg kicking is very important as well to ensure stability and help to maintain the body in an optimal position, thus reducing the resistive drag (Davies et al., 2009). In this work, the analysis is concentrated on the motion dynamics of the human lower limbs.

There have been few studies of the multibody dynamic analysis of human swimming because external forces are very difficult to obtain. CFD and SPH modelling offer quantitively insight into fluid forces.

However, the computational time cost becomes enormous for a single subject-specific analysis. Swumsuit offers the possibility of conduct human swimming simulations without solving the flow field (so the computational cost decreases) while still providing good results (Nakashima et al., 2007; Takagi et al., 2015). The integration of Swumsuit in a computational routine that performs kinematic data processing, kinematic analysis, and solves the inverse dynamic analysis is performed.

2. Methodology

The present dissertation studies the dynamics of motion of a healthy human subject performing a front crawl swimming stroke. To this end, the proposed methodology uses a general 3D multibody formulation in Cartesian coordinates to describe the position of the anatomical segments and the topological structure of the human body. By means of an inverse dynamic analysis, quantitative information on the resultant joint torques and intersegmental forces produced during the swimming stroke cycle is provided.

The methodological approach employed in this work is coded in MATLAB (Mathworks, Natick, MA). The data flow of the computational implementation, shown in Figure 2-1, is described in the following main steps of the analysis:

1. Development of a biomechanical human body model

Biomechanical models consist in mathematical representations that describe the physics and physiology of human body movement. For a wide variety of motions, biomechanical models are described as an open kinematic chain composed of several rigid bodies, that are interconnected by kinematic pairs, or joints, and acted upon by externally applied forces. Each rigid body represents an anatomical segment of the human body, holding the respective physical characteristics (mass, length, tensor of inertia, and position of the centre of mass in a local coordinate system), and the kinematic joints correspond to the anatomical articulations that constrain the relative motion between body segments. The externally applied forces set the dynamic interaction between the rigid bodies and the surrounding. For the sake of simplicity, anatomical segments are assumed to be infinitely rigid and the articulations to be ideal kinematic joints.

From the numerical point of view, the development of biomechanical models to study and analyse the structures of the human body is quite challenging due to the complexity and non-linear nature of the equations involved. Therefore, there has been a considerable effort to develop not only more accurate biomechanical models but also more efficient formulations that allow a simpler and systematic solution of the equations (Quental, 2013).

According to the type of motion being studied, the requirements on the discretisation level of detail of the biomechanical model may change. In this work, a full body biomechanical model was developed to study the front crawl swimming motion. The numerical methodology used in the definition of the biomechanical model followed a multibody formulation. By means of a Cartesian formulation, the position and orientation of each body segment was determined at each instant of time.

2. Experimental setup and data acquisition

In an inverse dynamics approach, the externally applied forces and the full-body system kinematics are given as input to the computational program. Regarding the experimental data acquisition,

motion capture systems represent the most common method for obtaining kinematic data in aquatic motion (Honda et al., 2012).

Data acquisition for the front crawl swimming stroke was conducted in LABIOMEP-UP using a three-dimensional motion capture system. Given the nature of the motion, the capture system comprised a set of underwater and above-water cameras. Reflective markers were attached to anatomical landmarks of the subject's body, following the protocol described in Appendix A. Due to the COVID-19 pandemic no complementary kinematic data acquisitions were performed during this dissertation. Instead, data taken previously for a male subject performing a hip-driven front crawl swimming stroke was provided by LABIOMEP-UP to be used in this work.

3. Data treatment and processing

Due to the inherent difficulties in an aquatic environment, especially in the air-water interface, the kinematic data acquisition by means of a motion capture system is associated with inaccuracy issues. The reliability of these measurements is proved to have an extreme impact on the goodness of the results of an inverse dynamic analysis (Honda et al., 2012). For that reason, experimental data were filtered for noise removal, and processed kinematically to obtain a suitable data set for the inverse dynamic analysis, ensuring that the motion reconstruction is consistent with the biomechanical model at every time instants of the stroke cycle, i.e., that the positions, velocities, and accelerations of the anatomical segments of the biomechanical model are consistent with the kinematic constraint equations of the biomechanical model and their derivatives.

4. Estimation of the hydrodynamic forces

Unlike other human motions (e.g. gait, jumping, running), in swimming there are no biomechanical equipment tools to acquire the external forces acting on each body segment. Takagi and Sanders (2002) computed the fluid forces acting on the hand by direct pressure measurements at a swimmer's hand surface using micro pressure sensors. Other studies (Arellano et al., 2000; Benjanuvatra et al., 2007; Jesus et al., 2019) made use of force plates to detect the external forces in swimming starts and turns. However, such tools do not allow the computation of the hydrodynamic forces acting on all body segments of the human body, for the entire swimming stroke cycle.

Numerical methods combined with experimental investigations are used to predict the hydrodynamic forces developed during swimming motions (Takagi et al., 2015). Computer simulation based on CFD and SPH methods has proven to be very powerful to this end. However, such methods are computationally and time expensive, given the complexity of simulating human swimming. Nakashima et al. (2007) developed an alternative computer simulation tool that requires much less computation time. The human body model is called SWUM and the simulation software in which the hydrodynamic forces are computed, based on simplified geometries of the swimmer anatomical segments moving on a fluid environment, is called Swumsuit. The software is available for free download and is used in the estimation of the hydrodynamic forces developed during the front crawl swimming stroke studied in this dissertation.

5. Implementation of an inverse dynamic analysis

The dynamics of a multibody system can be solved by means of an inverse or a forward dynamic analysis. The latter is used to predict the system's kinematics when the applied forces and joint torques are known, but not the subject motion. Although it is a more powerful alternative since in its formulation the availability of experimental data is not always necessary, a forward dynamic analysis is very often impractical in the computational cost point of view due to its very high computational costs and eventual lack of adherence between the computed movement and a realistic motion (Quental et al., 2016). For these reasons, the inverse dynamics approach is preferred for biomechanical system analyses. The intersegmental forces and joint torques are determined from the solution of the system of non-linear equations of the multibody system. In this dissertation, an inverse dynamic analysis of the human body system is performed for a front crawl swimming stroke cycle. The multibody system is actuated upon by joint torques.

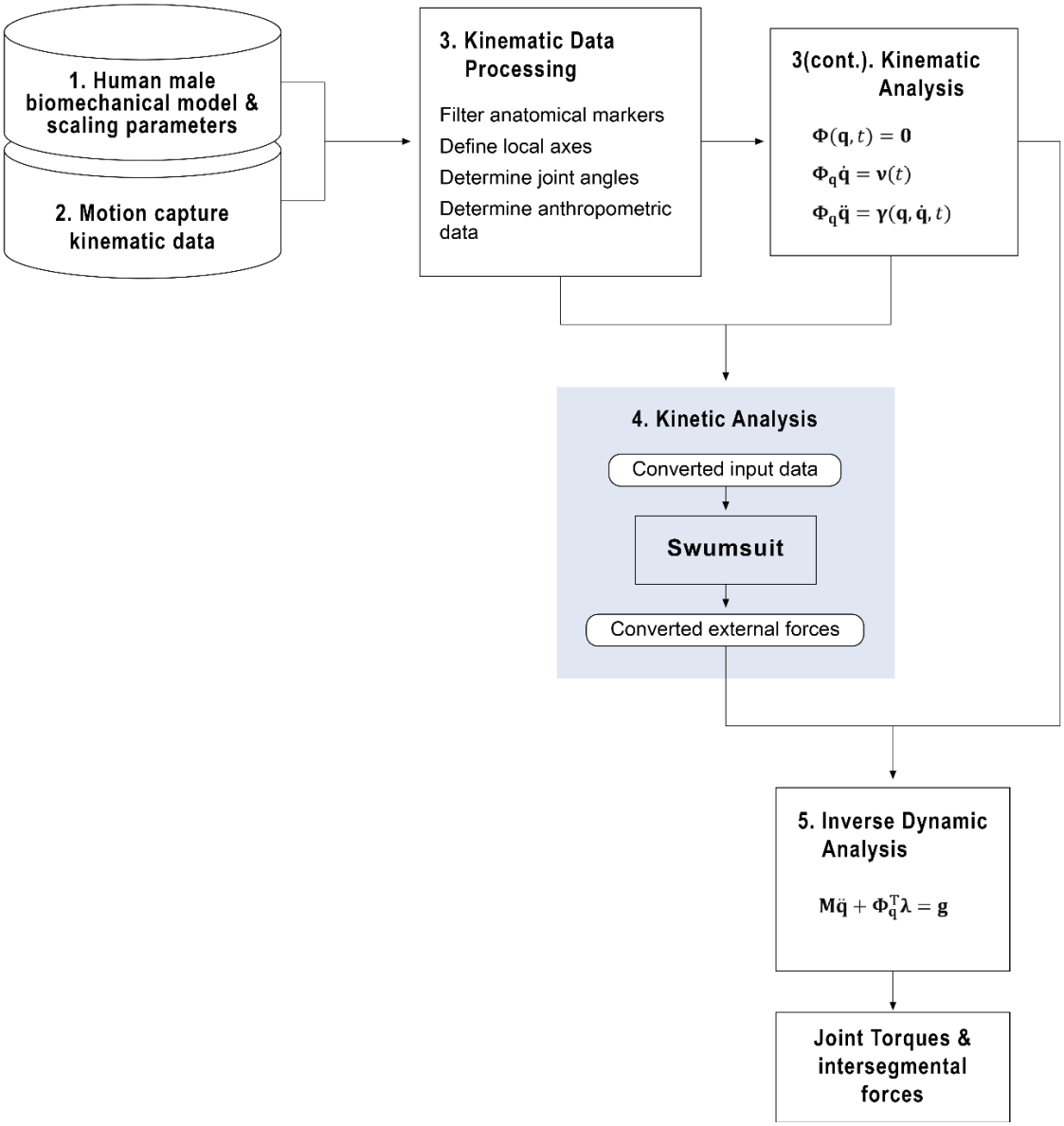

Figure 2-1: Flowchart of the MATLAB program implemented to perform inverse dynamic analyses of human motions. The steps highlighted in blue are further detailed in Chapter 6.

3. Biomechanical Model Formulation

In this chapter, the 3D multibody biomechanical model developed to study front crawl swimming is described. The modelling parameters, such as anthropometric data, and definition of the different body segments are based on scaling equations defined by Dumas et al. (2007a; 2007b), except for the head and neck, whose data is taken from Pàmies-Vilà (2012). Regarding the motion of body segments, the biomechanical model includes the definition of the articular structure of the full body model (Oliveira, 2016; Silva and Ambrósio, 2002).

3.1. Skeletal System

The study of human motion requires the formulation of biomechanical models composed of rigid bodies with proper physical and physiological properties. Since the definition of anthropometric data for every single individual is infeasible, linear regressions such as scaling equations, based on total body mass and segment length, are commonly used to obtain all the necessary BSIPs. Dumas et al. (2007a) developed, for both males and females, a complete dataset of scaling equations for the computation of BSIPs. In their work, data taken originally from McConville et al. (1980), who studied 31 adult males (mean age 27.5 years old, mean weight 80.5 kg, mean stature 1.77 m), were adjusted in order to provide BSIPs directly applicable in the conventional segment coordinate systems (Wu et al., 2002, 2005) and without restraining the position of the centre of mass (COM) and the orientation of the principal axes of inertia.

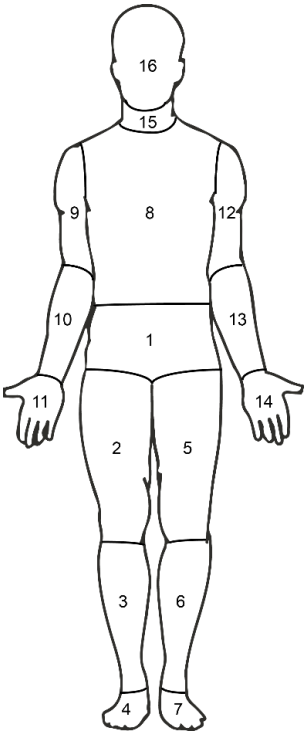

ID	Rigid Body	Description
1	Pelvis	From the 1st lumbar vertebra to the pelvic bone
2	Right Thigh	From right hip to right knee
3	Right Leg	From right knee to right ankle
4	Right Foot	From right ankle to midpoint between 1st and 5th right metatarsals
5	Left Thigh	From left hip to left knee
6	Left Leg	From left knee to left ankle
7	Left Foot	From left ankle to midpoint between 1st and 5th left metatarsals
8	Torso	From the 1st to the 12th thoracic vertebra
9	Right Arm	From right shoulder to right elbow
10	Right Forearm	From right elbow to right wrist
11	Right Hand	From right wrist to midpoint between 2nd and 5th right metacarpals
12	Left Arm	From left shoulder to left elbow
13	Left Forearm	From left elbow to left wrist
14	Left Hand	From left wrist to midpoint between 2nd and 5th left metacarpals
15	Neck	From the 1st to the 7th cervical vertebra
16	Head	Cranium, upper and lower jaws

Figure 3-1: Schematic representation of the full body biomechanical model of the human body and definition of the respective anatomical segments.

The 3D biomechanical model proposed here follows the human body topology considered by Dumas et al. (2007a), being composed of sixteen anatomical segments: pelvis, torso, neck, head, and right and left thighs, legs, feet, arms, forearms, and hands. The head and neck body segments are considered as two different bodies according to Pàmies-Vilà (2012). Given the complexity of the motion under analysis, all limbs play an important role on the body propulsion and lifting. For that reason, the biomechanical model is a full body representation of the human body. Figure 3-1 illustrates the skeletal structure and the description of each anatomical segment.

3.1.1. Anthropometric Measurements

The kinematic data provided by LABIOMEP-UP are obtained for a 25-year-old male swimmer with 70.3 kg, and 1.80 m, whose anthropometry is within the population considered for the development of the scaling equations proposed by Dumas et al. (2007a; 2007b). The resulting anthropometric measurements considered for the swimmer subject are listed in Table 3-1. The adjustment procedures and BSIPs scaling equations described in the dataset of Dumas et al. (2007a; 2007b) follow the recommendations of the *International Society of Biomechanics* (ISB) (Wu et al., 2002, 2005).

Table 3-1: Anthropometric data of the sixteen anatomical segments of the developed biomechanical model. The ID corresponds to the numeration in Figure 3-1. The COM, moments of inertia, and products of inertia are described in the respective body's local reference frame (with the origin at the proximal joint).

ID	Length [m]	COM in local frame [m]			Mass [kg]	Moments of Inertia [10^{-2} kg·m^2]					
		ξ	η	ζ		$I_{\xi\xi}$	$I_{\eta\eta}$	$I_{\zeta\zeta}$	$I_{\xi\eta}$	$I_{\xi\zeta}$	$I_{\eta\zeta}$
1	0.2591[1]	-0.0871	-0.0386	-7.7727e-04	9.9826	68.36	75.29	60.48	4.19	0.96	0.43
2	0.4689	-0.0192	-0.2011	0.0155	8.6469	15.99	4.28	17.11	0.93	0.08	0.93
3	0.3927	-0.0189	-0.1610	0.0027	3.3744	4.08	0.52	4.08	0.08	0.02	0.13
4	0.1311	0.0501	-0.0198	0.0034	0.8436	0.04	0.20	0.19	0.02	0.01	0
5	0.4687	-0.0192	-0.2011	-0.0155	8.6469	15.98	4.27	17.10	0.93	0.08	0.93
6	0.4065	-0.0195	-0.1667	-0.0028	3.3744	4.37	0.56	4.37	0.09	0.02	0.14
7	0.1158	0.0442	-0.0175	-0.0030	0.8436	0.03	0.15	0.15	0.02	0.01	0
8	0.4055	-0.0146	-0.1703	-0.0008	23.4099	28.06	24.06	30.18	12.47	0.15	0.62
9	0.3066	0.0052	-0.1386	-8.1097e-04	1.6872	1.52	0.31	1.62	0.06	0.04	0.01
10	0.2659	0.0027	-0.1109	0.0037	1.1951	0.66	0.10	0.62	0.01	0	0.05
11	0.0920	0.0075	-0.0772	0.0068	0.4218	0.13	0.05	0.11	0.02	0.01	0.01
12	0.3075	0.0052	-0.1390	0.0080	1.6872	1.53	0.31	1.63	0.06	0.04	0.01
13	0.2613	0.0026	-0.1090	-0.0037	1.1951	0.64	0.10	0.59	0.01	0	0.05
14	0.0988	0.0081	-0.0829	-0.0073	0.4218	0.15	0.06	0.13	0.02	0.01	0.02
15	0.1444	0	0.0570	0	0.9420	0.15	0.09	0.18	0.01	0	0
16	0.1733	0.0791	0.0303	0	3.7681	0.89	0.50	1.02	0.06	0	0.01

[1]For pelvis, see Figure 3-2 for length definition and origin of local reference frame.

Apart from the pelvis body segment, all anatomical lengths correspond to the description in Figure 3-1, and the position of the COM, moments of inertia, and products of inertia are expressed in the body local

reference frame (ξ, η, ζ) (with the origin at the proximal joint). Regarding the pelvis body segment, Dumas et al. (2007a) proposed an alternative definition, consisting in the distance between the right anterior superior iliac spine (RASIS) to left anterior superior iliac spine (LASIS). Following this alternative, the origin of the pelvis local reference frame is the midpoint between RASIS to LASIS. The alternative body length definition and origin of the local reference frame are illustrated in Figure 3-2.

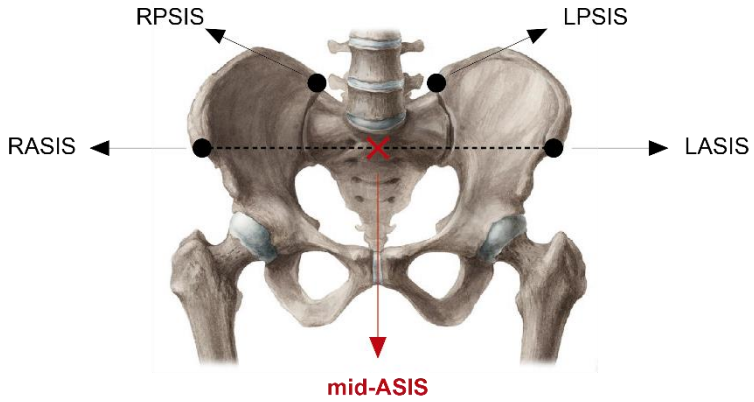

Figure 3-2: Frontal view of the pelvic bone (adapted from *Lower extremity: Anatomy study course | Kenhub*), showing the right and left anterior superior iliac spine and right and left posterior superior iliac spine (RASIS, LASIS, RPSIS, and RPSIS, respectively) anatomical landmarks. The midpoint between the RASIS and LASIS is displayed in red.

3.2. Articular System

The sixteen anatomical segments are linked by fifteen anatomical joints: eight spherical joints represent the cervical, lumbar, and right and left hip, shoulder, and ankle joints; four universal joints represent the right and left elbow and wrist joints; and three revolute joints represent the right and left knee, and the atlanto-occipital joints (Oliveira, 2016). Figure 3-3 illustrates the topology of the articular system of the biomechanical model.

For most swimming stroke techniques, the range of motion between body segments is higher than the common motions studied in the literature, especially regarding the shoulder complex. Considering the model topology described before, the level of discretisation of the biomechanical model may be considered insufficient to study the dynamics of motion of the upper limbs. However, and since the aim of this study is to analyse the dynamics of the lower limbs during a front crawl swimming stroke, the formulation of the articular system is deemed suitable for the motion under analysis (Nakashima et al., 2007).

The type of anatomical joint dictates the number of constrained degrees of freedom (DOF). The remaining, unconstrained, DOF define the total DOF of the multibody system. The 3D biomechanical model developed includes 41 DOF: six describe the position and orientation of the pelvis with respect to the global reference frame, which is responsible for the motion of the human body model as one whole; the remaining 35 DOF are related to the relative motion of the anatomical segments at the kinematic joints: 24 for the rotation of the cervical, lumbar, and right and left hip, shoulder, and ankle joints; 8 for the rotation of the right and left elbow and wrist joints, and 3 for the rotation of the right and

left knee, and the atlanto-occipital joints. Figure 3-3(b) illustrates the 41 DOF of the articular system of the biomechanical model.

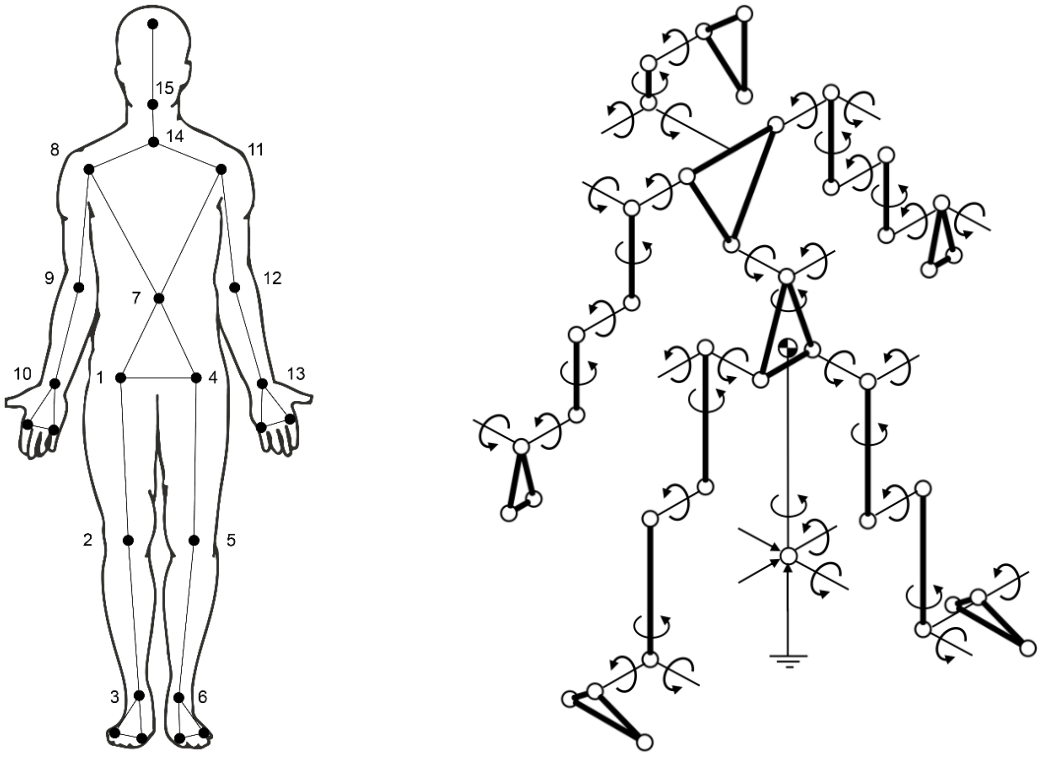

(a) (b)

Figure 3-3: Schematic representation of kinematic joints of the full body biomechanical model: (a) topology of the articular system and (b) exploded view of the full body biomechanical model. The 41 DOF are represented by circular arrows.

Considering a Cartesian coordinates formulation, to be detailed in Chapter 4, the joint centres of rotation and other anatomical reference points are defined in body-fixed reference frames (ξ, η, ζ). The origin of each local reference frame is the COM of the respective body segment, and the corresponding orientations of the local axes are defined according to the ISB recommendations (Wu et al., 2002, 2005).

Table 3-2 contains all the data regarding the fifteen kinematic joints. Each joint is described in the local reference frame of the proximal and distal bodies. Spherical joints are fully described by their centre of rotation since no constraints exist on the rotation. Universal and revolute joints require the definition of axes of rotation about which the bodies rotate. *In vivo* measurements allow the estimation of biological axes of rotation, offering a more accurate and consistent dataset (Horsman et al., 2007). However, in this study the axes of rotation of the universal and revolute joints were determined as being the same as the local direction axes, i.e., the rotation axes are aligned with the body-fixed reference frame.

Table 3-2: Coordinates of the centres of rotation of the 15 kinematic joints in the biomechanical model developed. The ID corresponds to the numeration in Figure 3-3. All coordinates are described in the respective body's local reference frame.

ID	Joint	Type	Proxi-mal Body	Distal Body	Local centre of rotation in the proximal body [m]			Local centre of rotation in the distal body [m]		
					ξ	η	ζ	ξ	η	ζ
1	Right Hip	Spherical	Pelvis	Right Thigh	0.0613	-0.0567	0.0937	0.0192	0.2011	-0.0155
2	Right Knee	Revolute	Right Thigh	Right Leg	0.0195	-0.2675	-0.0152	0.0189	0.1610	-0.0027
3	Right Ankle	Spherical	Right Leg	Right Foot	0.0190	-0.2317	-0.0027	-0.0501	0.0198	-0.0034
4	Left Hip	Spherical	Pelvis	Left Thigh	0.0613	-0.0567	-0.0937	-0.0192	0.2011	-0.0155
5	Left Knee	Revolute	Left Thigh	Left Leg	-0.0195	-0.2674	-0.0152	-0.0195	0.1667	-0.0028
6	Left Ankle	Spherical	Left Leg	Left Foot	-0.0197	-0.2399	-0.0028	0.0442	0.0175	-0.0030
7	Lumbar	Spherical	Pelvis	Torso	-0.0035	0.0301	0	0.0145	-0.2355	8.5008e-04
8	Right Shoulder	Spherical	Torso	Right Arm	0.0323	0.1088	0.1785	-0.0052	0.1386	0.0080
9	Right Elbow	Universal	Right Arm	Right Forearm	-0.0057	-0.1618	0.0079	-0.0027	0.1109	-0.0037
10	Right Wrist	Universal	Right Forearm	Right Hand	-0.0028	-0.1560	-0.0038	-0.0075	0.0772	-0.0068
11	Left Shoulder	Spherical	Torso	Left Arm	0.0323	0.1088	-0.1785	0.0052	0.1390	0.0080
12	Left Elbow	Universal	Left Arm	Left Forearm	0.0057	-0.1623	0.0079	0.0026	0.1090	-0.0037
13	Left Wrist	Universal	Left Forearm	Left Hand	0.0028	-0.1533	-0.0037	0.0081	0.0829	-0.0073
14	Cervical	Spherical	Torso	Neck	0.0146	0.1703	8.1097e-04	0	-0.0570	0
15	Atlanto-occipital	Revolute	Neck	Head	0	0.0875	0	-0.0791	-0.0303	0

4. Multibody Dynamics Overview

In this chapter, the methods based on multibody dynamics used to study the human motion, including the formulation required to perform kinematic and inverse dynamic analyses, are introduced. The methodology and notation adopted in this work follows that of Nikravesh (1988), being the system described using a set of Cartesian coordinates.

4.1. Cartesian Coordinates

The development of general-purpose programs is of great interest in biomechanics, since the governing equations addressed to a mechanical system can be replicated to another. The computational efficiency of a general-purpose program depends upon several factors, one of which is the choice of coordinates (Nikravesh, 1988). However, the computational efficiency might not be the decisive factor for all analyses. Regarding multibody dynamics applied to inverse dynamic analyses, a Cartesian coordinates formulation is a common methodology used. Even though it is a less computationally efficient method than others based on minimal coordinates, the low order of nonlinearity and the simplicity in deriving the equations of motion becomes an enormous advantage when compared to other types of coordinates, such as generalized and relative coordinates (Nikravesh, 1988). Therefore, Cartesian coordinates are adopted in this work to describe the multibody system. When using this type of coordinates, body-fixed reference frames are considered embedded in each body segment of the multibody system so that their position and orientation can be defined about a global, stationary reference frame, at every instant of time of the analysis, as illustrated in Figure 4-1.

In the three-dimensional domain, an unconstrained body requires 6 independent coordinates to describe its configuration, i.e., in 3 translations and 3 rotations. These coordinates define the Cartesian coordinate system that is fixed in the body, meaning that the translational coordinates locate the origin of the body-fixed, or local, reference frame relative to the global reference frame, and the rotational coordinates define the orientation of the respective local axes.

For large-scale computer programs dealing with the angular orientation of rigid bodies, an alternative to the three angles defining the body orientation, for instance Euler angles, consists in the definition of a set of four orientational coordinates, known as Euler parameters, which are normalised quaternions. These coordinates are related by the relationship $\mathbf{p}^{\mathrm{T}}\mathbf{p} = 1$, where $\mathbf{p}$ is a vector containing the four Euler parameters. Note that this alternative also describes 3 rotations only. Although both formulations lead to the same rotational matrix $\mathbf{A}$, their physical meaning is different: Euler angles represent three consecutive rotations while Euler parameters represent a single rotation about a specific axis. The application of Euler parameters is preferred over the Euler angles since the former drastically simplifies the mathematical formulation involved in large-scale multibody programs, and is free of some deficiencies, such as singularity issues (Nikravesh, 1988).

Considering the Cartesian coordinates formulation, the coordinates of a point *P*, defined in the local reference frame of a body *i*, are given in the global reference frame by the expression:

$$\mathbf{r}^P = \mathbf{r}_i + \mathbf{A}_i \mathbf{s}'^P_i \tag{4-1}$$

where $\mathbf{r}^P$ are the global coordinates of point *P*, $\mathbf{r}_i$ are the translational coordinates of body *i*, $\mathbf{A}_i$ is the rotation matrix of body *i*, defined by its Euler parameters, and $\mathbf{s}'^P_i$ are the coordinates of point *P* in the local reference frame of body *i*. Note that any vector defined in the local reference frame of a body is represented with a superscripted apostrophe.

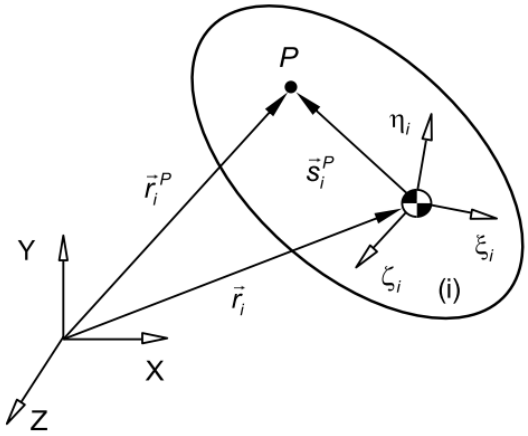

Figure 4-1: Location of point *P* in the global (XYZ) and local (ξ, η, ζ) reference frames.

Considering a multibody system composed of n bodies, in which the position and orientation of each body at every instant of time is defined in a column vector of generalised coordinates $\mathbf{q}$, the overall vector of coordinates has $(7 \times n)$ entries, and is written as

$$\mathbf{q} = [\mathbf{q}_1^{\mathrm{T}},\ \mathbf{q}_2^{\mathrm{T}}, \dots\ \mathbf{q}_n^{\mathrm{T}}]^{\mathrm{T}}, \text{ with } \mathbf{q}_i = \{\mathbf{r}_i^{\mathrm{T}}, \mathbf{p}_i^{\mathrm{T}}\} = \{x, y, z, e_0, e_1, e_2, e_3\}_i^{\mathrm{T}} \tag{4-2}$$

where $\mathbf{r} = \{x, y, z\}$ represent the translational coordinates, and $\mathbf{p} = \{e_0, e_1, e_2, e_3\}$ represent the Euler parameters of a body.

The multibody system configuration is not independent since kinematic joints constrain the relative motion of adjacent body segments. Besides, driver actuators are responsible for guiding the body system according to the motion performed, in particular for biomechanical applications. The relationships between the coordinates at every instant of time are introduced in the form of algebraic equations, grouped as a vector of constraint equations, $\mathbf{\Phi}$. The number of DOF of the multibody system decreases by the same number of independent constraint equations. From the kinematic point of view, all constraints must be fulfilled for every instant of time, which is reflected by:

$$\mathbf{\Phi}(\mathbf{q}, t) = [\mathbf{\Phi}_1(\mathbf{q}), \dots \mathbf{\Phi}_{ns}(\mathbf{q}), \dots \mathbf{\Phi}_1(\mathbf{q}, t), \dots \mathbf{\Phi}_{nr}(\mathbf{q}, t)]^{\mathrm{T}} = \mathbf{0} \tag{4-3}$$

where $\boldsymbol{\Phi}_i$ is the i^{th} kinematic constraint equation, *ns* is the total number of scleronomic constraints, *nr* is the total number of rheonomic constraints, and $\mathbf{0}$ is a null vector. Scleronomic constraints are time independent, i.e., the time variable does not appear explicitly in them, while rheonomic constraints are time dependent. The first type is associated with the equation constraints of the kinematic joints, such as spherical, revolute, or universal joints, while the latter is mostly associated to driver constraint equations (Silva, 2003).

4.2. Kinematic Consistency

From the mechanical formulation point of view, the motion of a multibody system is considered fully known when the consistency between its motion and the kinematic constraints is achieved. The fulfilment of the kinematic constraints can be ensured via a kinematic analysis. A kinematic analysis consists in the study of motion independently of the forces responsible for modifying the dynamic behaviour of the system. Instead, the positions, velocities and accelerations are calculated according to the topology of the mechanical system. Considering the multibody system guided by driving elements, the kinematic consistent positions, for every instant of time of the analysis, are obtained by solving Equation (*4-3*) with respect to the vector of generalised coordinates $\mathbf{q}$.

The system of constraint equations yields to a set of non-linear equations that must be solved using an appropriate optimization method. The most common and frequently used solution method for nonlinear equations is the Newton-Raphson method (Nikravesh, 1988). By following the approach of Newton-Raphson, the solution of the system is based in the linearization of Equation (*4-3*), i.e., by replacing the system of equations with the two first terms of its expansion in a Taylor series, evaluated at an initial approximation $\mathbf{q}_i$. By doing so, Equation (*4-3*) becomes:

$$\boldsymbol{\Phi}(\mathbf{q}, t) \cong \boldsymbol{\Phi}(\mathbf{q}_i, t) + \boldsymbol{\Phi}_{\mathbf{q}}(\mathbf{q}_i)(\mathbf{q} - \mathbf{q}_i) = \mathbf{0} \tag{4-4}$$

where $\boldsymbol{\Phi}_{\mathbf{q}}(\mathbf{q}_i)$ is the Jacobian matrix of the constraints, evaluated at the approximated solution $\mathbf{q}_i$. The iterative procedure stops when the residual for the actual iteration, defined as $\Delta\mathbf{q}_i = \mathbf{q}_{i+1} - \mathbf{q}_i$, is less than a predefined tolerance.

The Jacobian matrix of the constraints is defined by the partial derivatives of each kinematic constraint with respect to the vector of generalised coordinates, given as:

$$\boldsymbol{\Phi}_{\mathbf{q}}(\mathbf{q}) = \begin{bmatrix} \dfrac{\partial \boldsymbol{\Phi}_1}{\partial \mathbf{q}_1} & \cdots & \dfrac{\partial \boldsymbol{\Phi}_1}{\partial \mathbf{q}_{nc}} \\ \vdots & \ddots & \vdots \\ \dfrac{\partial \boldsymbol{\Phi}_{nh}}{\partial \mathbf{q}_1} & \cdots & \dfrac{\partial \boldsymbol{\Phi}_{nh}}{\partial \mathbf{q}_{nc}} \end{bmatrix} \tag{4-5}$$

where *nc* is the number of rigid bodies, and *nh* is the number of constraint equations.

Once the consistency of the system positions is achieved, the velocities and accelerations can be determined using the velocity and acceleration constraint equations, respectively. The velocity vector of constraint equations, $\dot{\mathbf{\Phi}}$, is obtained by differentiating Equation (*4-3*) with respect to time:

$$\dot{\mathbf{\Phi}}(\mathbf{q}, \dot{\mathbf{q}}, t) = \frac{\partial \mathbf{\Phi}(\mathbf{q}, t)}{\partial t} + \frac{\partial \mathbf{\Phi}(\mathbf{q}, t)}{\partial \mathbf{q}} \dot{\mathbf{q}} = \mathbf{0} \tag{4-6}$$

where $\partial \mathbf{\Phi}(\mathbf{q}, t)/\partial t$ is the vector of partial derivatives of the constraints with respect to time, $\partial \mathbf{\Phi}(\mathbf{q}, t)/\partial \mathbf{q}$ is the Jacobian matrix of the constraints, and $\dot{\mathbf{q}}$ is the vector of generalised velocities. If $\boldsymbol{\nu}(t)$ is defined as the right-hand side vector of the velocity constraint equations, the consistent velocities of the system are obtained by the solution of the following system of equations:

$$\mathbf{\Phi}_{\mathbf{q}} \dot{\mathbf{q}} = \boldsymbol{\nu}(t), \quad with \quad \boldsymbol{\nu}(t) = -\frac{\partial \mathbf{\Phi}(\mathbf{q}, t)}{\partial t} \tag{4-7}$$

Similarly, the acceleration vector of constraint equations, $\ddot{\mathbf{\Phi}}$, is determined by differentiating Equation *(4-6*) with respect to time, which is analogous to the second differentiation of Equation (*4-3*) also with respect to time. The following expression for $\ddot{\mathbf{\Phi}}$ is obtained:

$$\ddot{\mathbf{\Phi}}(\mathbf{q}, \dot{\mathbf{q}}, \ddot{\mathbf{q}}, t) = \mathbf{\Phi}_{\mathbf{q}} \ddot{\mathbf{q}} + \left(\mathbf{\Phi}_{\mathbf{q}} \dot{\mathbf{q}}\right)_{\mathbf{q}} \dot{\mathbf{q}} - \dot{\boldsymbol{\nu}}(t) = \mathbf{0} \tag{4-8}$$

where $\ddot{\mathbf{q}}$ is the vector of generalised accelerations. Defining $\boldsymbol{\gamma}(\mathbf{q}, \dot{\mathbf{q}}, t)$ as the right-hand side of the acceleration constraint equations, Equation (*4-8*) can be rewritten to:

$$\mathbf{\Phi}_{\mathbf{q}} \ddot{\mathbf{q}} = \boldsymbol{\gamma}(\mathbf{q}, \dot{\mathbf{q}}, t), \quad with \quad \boldsymbol{\gamma}(\mathbf{q}, \dot{\mathbf{q}}, t) = \dot{\boldsymbol{\nu}}(t) - \left(\mathbf{\Phi}_{\mathbf{q}} \dot{\mathbf{q}}\right)_{\mathbf{q}} \dot{\mathbf{q}} \tag{4-9}$$

The solution of Equations (*4-4*), (*4-7*), and (*4-9*) leads to the consistent positions, velocities, and accelerations of the multibody system, respectively. It should be noted that, in the presence of redundant constraint equations, i.e., when the number of equations is greater than the number of DOF, linearly dependent lines appear in the system. In order to solve this, a least squares formulation is adopted (Silva, 2003).

In biomechanical literature, it is common to find applications in which the system velocities and accelerations are obtained by performing time derivatives as a spline interpolation of the positions. Although the errors in the velocities and accelerations obtained by spline differentiation may be under control, these velocities are deemed as non-consistent with the constraint equations (Silva and Ambrósio, 2002).

4.3. Kinematic Constraints

The coordinates in vector $\mathbf{q}$ are usually not independent, being their relations described by kinematic constraints. Several types of constraint equations exist to describe the relationship between the overall

coordinates of a multibody system. In this section, only the kinematic constraints required to define the multibody model described in Chapter 3 are introduced.

Two types of kinematic constraints can be essentially identified when using Cartesian coordinates: joint constraints that are applied to impose the relative motion between two adjacent body segments, such as those associated with spherical, universal, and revolute kinematic joints; and driver constraints that prescribe changes in the motion of the system over time. The complete description of each kinematic constraint includes the algebraic equation constraining the DOF, the contribution to the Jacobian matrix, and the right-hand side vectors of velocity and acceleration constraint equations.

Before addressing the different types of kinematic constraints, it should be noticed that although the use of Euler parameters is presented as the better alternative to define the angular orientation of a body in the three-dimensional space, more equations are generated when using their time derivatives (Nikravesh, 1988). Therefore, the Jacobian matrix and the right-hand side vectors of the velocity and acceleration constraint equations are modified to be described with respect to three local angular velocities and accelerations, denoted as $\boldsymbol{\omega}'$ and $\dot{\boldsymbol{\omega}}'$, respectively. By doing so, the number of equations is reduced without any conflict with the definition of body orientations by means of Euler parameters (Nikravesh, 1988). As a result of this modification, the vector of generalised velocities and accelerations, $\dot{\mathbf{q}}$ and $\ddot{\mathbf{q}}$, respectively, reduces to six entries per rigid body, instead of seven as is the case of the vector of generalised positions $\mathbf{q}$.

4.3.1. Spherical Joint

A spherical, or ball-and-socket, joint between two rigid bodies *i* and *j* is established by three algebraic equations that constrain the position of a shared point *P*, locally defined in the body-fixed reference frames of bodies *i* and *j*, as depicted in Figure 4-2. Accordingly, only rotational movements are allowed about the given point *P*, defined as the centre of rotation. The vector of constraint equations is expressed as:

$$\boldsymbol{\Phi}^{(s,3)} = \mathbf{r}_i + \mathbf{A}_i \mathbf{s}'^{P}_i - \mathbf{r}_j - \mathbf{A}_j \mathbf{s}'^{P}_j = \mathbf{0} \tag{4-10}$$

where the superscripts in $\boldsymbol{\Phi}$ indicate the type of joint and the number of constraint equations, $\mathbf{r}$ is the global position vector, $\mathbf{A}$ is the rotation matrix, and $\mathbf{s}'^{P}$ is the position vector of point *P* in the local reference frame of bodies *i* and *j*.

The Jacobian matrix and the right-hand side vectors of the velocity and acceleration constraint equations are modified to be written with respect to the local angular velocities and local angular accelerations. Thus, the differentiation of Equation (*4-10*) with respect to time yields:

$$\begin{aligned} \dot{\boldsymbol{\Phi}}^{(s,3)} &= \frac{\partial \boldsymbol{\Phi}^{(s,3)}}{\partial \mathbf{r}_i}\dot{\mathbf{r}}_i + \frac{\partial \boldsymbol{\Phi}^{(s,3)}}{\partial \mathbf{p}_i}\dot{\mathbf{p}}_i + \frac{\partial \boldsymbol{\Phi}^{(s,3)}}{\partial \mathbf{r}_j}\dot{\mathbf{r}}_j + \frac{\partial \boldsymbol{\Phi}^{(s,3)}}{\partial \mathbf{p}_j}\dot{\mathbf{p}}_j = \\ &= \frac{\partial \boldsymbol{\Phi}^{(s,3)}}{\partial \mathbf{r}_i}\dot{\mathbf{r}}_i + \frac{1}{2}\frac{\partial \boldsymbol{\Phi}^{(s,3)}}{\partial \mathbf{p}_i}\mathbf{L}_i^{\mathrm{T}}\boldsymbol{\omega}'_i + \frac{\partial \boldsymbol{\Phi}^{(s,3)}}{\partial \mathbf{r}_j}\dot{\mathbf{r}}_j + \frac{1}{2}\frac{\partial \boldsymbol{\Phi}^{(s,3)}}{\partial \mathbf{p}_j}\mathbf{L}_j^{\mathrm{T}}\boldsymbol{\omega}'_j \end{aligned} \tag{4-11}$$

where $\partial\mathbf{\Phi}^{(s,3)}/\partial\mathbf{r}$ and $\partial\mathbf{\Phi}^{(s,3)}/\partial\mathbf{p}$ are the vectors containing the partial derivatives of the constraints with respect to $\mathbf{r}$ and $\mathbf{p}$, respectively, and $\mathbf{L}$ is the local transformation matrix for bodies *i* and *j*, given by:

$$\mathbf{L} = \begin{bmatrix} -e_1 & e_0 & e_3 & -e_2 \\ -e_2 & -e_3 & e_0 & e_1 \\ -e_3 & e_2 & -e_1 & e_0 \end{bmatrix} \tag{4-12}$$

where e_0, e_1, e_2, and e_3 are the Euler parameters. The contribution of the spherical joint to the Jacobian matrix and to the right-hand side vector of the velocity constraint equations is given by:

$$\begin{array}{cccccccccccc} & \dot{\mathbf{r}}_1 & \boldsymbol{\omega}'_1 & \ldots & \dot{\mathbf{r}}_i & \boldsymbol{\omega}'_i & \ldots & \dot{\mathbf{r}}_j & \boldsymbol{\omega}'_j & \ldots & \dot{\mathbf{r}}_n & \boldsymbol{\omega}'_n \\ \mathbf{\Phi}_{\mathbf{q}}^{(s,3)} = \big[& \mathbf{0} & \mathbf{0} & \ldots & \mathbf{I} & -\tilde{\mathbf{s}}_i^P \mathbf{A}_i & \ldots & -\mathbf{I} & \tilde{\mathbf{s}}_j^P \mathbf{A}_j & \ldots & \mathbf{0} & \mathbf{0} \big] \end{array} \tag{4-13}$$

$$\boldsymbol{\nu}^{(s,3)} = \mathbf{0}$$

where $\mathbf{I}$ is the (3×3) identity matrix, and $\tilde{\mathbf{s}}^P$ is the skew-symmetric matrix of the vector $\mathbf{s}^P$ of either body *i* or body *j*. References to the translational and rotational velocities of each body are presented in Equation (*4-13*), above the Jacobian matrix, to help identify the position of the non-null entries of the Jacobian matrix.

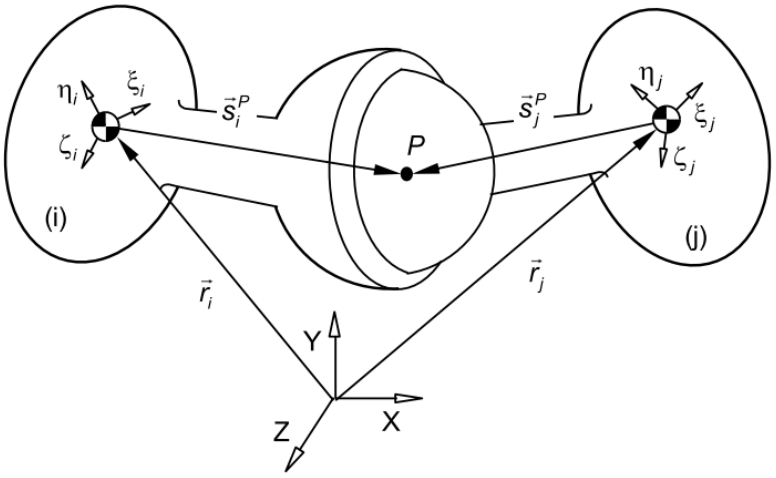

Figure 4-2: Spherical joint between bodies *i* and *j*.

Similarly, the second time differentiation of Equation *(4-10*) leads to the acceleration equations. The right-hand side vector of the acceleration constraint equations is given as:

$$\boldsymbol{\gamma}^{(s,3)} = -\tilde{\boldsymbol{\omega}}_i \dot{\mathbf{s}}_i^P + \tilde{\boldsymbol{\omega}}_j \dot{\mathbf{s}}_j^P, \text{ with } \dot{\mathbf{s}}^P = \tilde{\boldsymbol{\omega}} \mathbf{s}^P \tag{4-14}$$

where $\tilde{\boldsymbol{\omega}}$ is the skew-symmetric matrix of the global angular velocity and $\dot{\mathbf{s}}^P$ is the first-time derivative of vector $\mathbf{s}^P$.

4.3.2. Universal Joint

A universal joint connecting bodies *i* and *j* is illustrated in Figure 4-3. Analogously to the spherical joint, *P* is a point that simultaneously belongs to bodies *i* and *j*, being locally defined in both body-fixed reference frames. Therefore, the same set of equations defined in Equation (*4-10*) are valid to constrain the 3 translational DOF of the universal joint. The cross in the middle of the two bodies results in the definition of two axes of rotation that intersect at point *P*, meaning that 1 rotational DOF is also constrained.

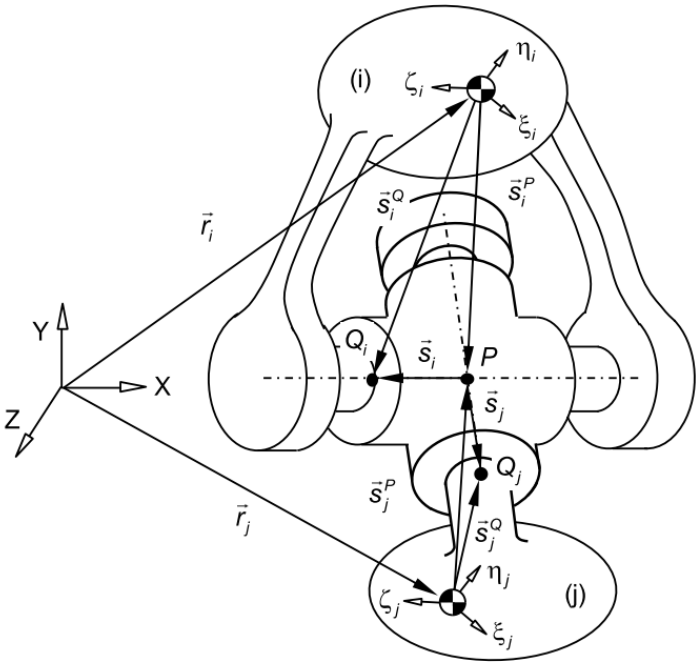

Figure 4-3: Universal joint between bodies *i* and *j*. The vector $\boldsymbol{s}_i$ is perpendicular to $\boldsymbol{s}_j$.

Considering $\mathbf{s}_i$ as the vector defining the joint axis of rotation from the configuration of body *i*, and $\mathbf{s}_j$ the vector defining the joint axis of rotation from the configuration of body *j*, the rotational constraint equation states that these two vectors must always remain perpendicular (Nikravesh, 1988). The vector of constraint equations of the universal joint is given by:

$$\boldsymbol{\Phi}^{(u,4)} = \begin{bmatrix} \boldsymbol{\Phi}^{(s,3)} \\ \mathbf{s}_i^{\mathrm{T}}\mathbf{s}_j \end{bmatrix} = \mathbf{0} \tag{4-15}$$

The contribution to the Jacobian matrix and to the right-hand side vectors of the velocity and acceleration constraint equations is given by:

$$\boldsymbol{\Phi}_{\mathbf{q}}^{(u,4)} = \begin{bmatrix} & & & & & \boldsymbol{\Phi}_{\mathbf{q}}^{(s,3)} & & & & \\ \mathbf{0} & \mathbf{0} & \dots & \mathbf{0} & -\mathbf{s}_j^{\mathrm{T}}\tilde{\mathbf{s}}_i\mathbf{A}_i & \dots & \mathbf{0} & -\mathbf{s}_i^{T}\tilde{\mathbf{s}}_j\mathbf{A}_j & \dots & \mathbf{0} & \mathbf{0} \end{bmatrix}$$

$$\boldsymbol{\nu}^{(u,4)} = \mathbf{0} \tag{4-16}$$

$$\boldsymbol{\gamma}^{(u,4)} = \begin{bmatrix} \boldsymbol{\gamma}^{(s,3)} \\ -2\dot{\mathbf{s}}_i^{\mathrm{T}}\dot{\mathbf{s}}_j + \dot{\mathbf{s}}_i^{\mathrm{T}}\tilde{\boldsymbol{\omega}}_i\mathbf{s}_j + \dot{\mathbf{s}}_j^{\mathrm{T}}\tilde{\boldsymbol{\omega}}_j\mathbf{s}_i \end{bmatrix}$$

4.3.3. Revolute Joint

A revolute, or hinge, joint between bodies *i* and *j* is shown is Figure 4-4. The revolute joint can be regarded as an extension of the spherical joint, meaning that all translational DOF are constrained. However, the motion of a revolute joint occurs about a single specific axis, which means that the remaining 2 rotational DOF are also constrained.

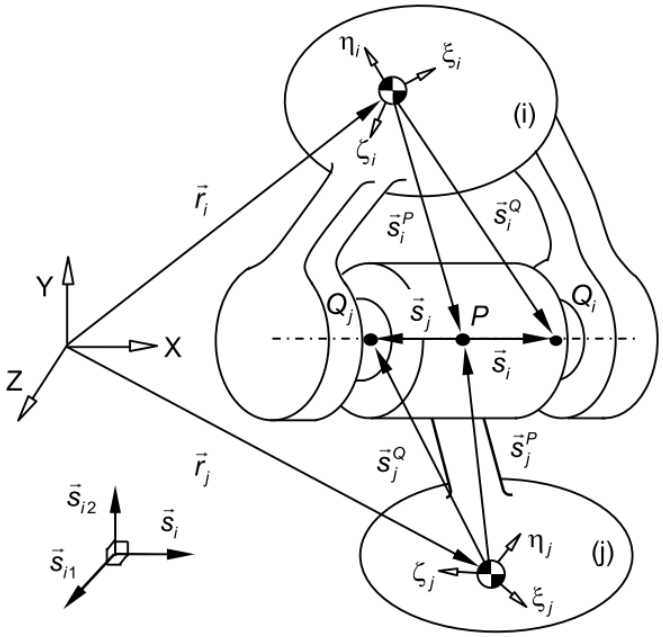

Figure 4-4: Revolute joint between bodies *i* and *j*. The vectors $\boldsymbol{s}_{i1}$ and $\boldsymbol{s}_{i2}$ represented in the left low corner are simultaneously perpendicular to $\boldsymbol{s}_i$ and to each other, and $\boldsymbol{s}_i$ is the vector defining the joint axis of rotation from the configuration of body *i*.

Considering the same $\mathbf{s}_i$ and $\mathbf{s}_j$ vectors described for the universal joint, the rotational constraint equations must ensure that $\mathbf{s}_i$ and $\mathbf{s}_j$ are always parallel to each other. According to Nikravesh (1988), this is accomplished by performing the cross product between $\mathbf{s}_i$ and $\mathbf{s}_j$. However, this leads to three constraint equations, one of which is linearly dependent of the remaining. The formulation used to overcome this indeterminacy consists in the application of two dot products instead of one cross product (Quental, 2013). Defining two vectors, $\mathbf{s}_{i1}$ and $\mathbf{s}_{i2}$, simultaneously perpendicular to $\mathbf{s}_i$ and to each other (represented in the left low corner of Figure 4-4), the constraint equations of the revolute joint can be written as:

$$\boldsymbol{\Phi}^{(r,5)} = \begin{bmatrix} \boldsymbol{\Phi}^{(s,3)} \\ \mathbf{s}_{i1}^{\mathrm{T}}\mathbf{s}_j \\ \mathbf{s}_{i2}^{\mathrm{T}}\mathbf{s}_j \end{bmatrix} = \mathbf{0} \tag{4-17}$$

The contribution of the revolute joint to the Jacobian matrix and to the right-hand side vectors of the velocity and acceleration constraint equations is given by:

$$\boldsymbol{\Phi}_{\mathbf{q}}^{(r,5)} = \begin{bmatrix} & & & & & \boldsymbol{\Phi}_{\mathbf{q}}^{(s,3)} & & & & & \\ \mathbf{0} & \mathbf{0} & \dots & \mathbf{0} & -\mathbf{s}_j^{\mathrm{T}}\tilde{\mathbf{s}}_{i1}\mathbf{A}_i & \dots & \mathbf{0} & -\mathbf{s}_{i1}^{\mathrm{T}}\tilde{\mathbf{s}}_j\mathbf{A}_j & \dots & \mathbf{0} & \mathbf{0} \\ \mathbf{0} & \mathbf{0} & \dots & \mathbf{0} & -\mathbf{s}_j^{\mathrm{T}}\tilde{\mathbf{s}}_{i2}\mathbf{A}_i & \dots & \mathbf{0} & -\mathbf{s}_{i2}^{\mathrm{T}}\tilde{\mathbf{s}}_j\mathbf{A}_j & \dots & \mathbf{0} & \mathbf{0} \end{bmatrix}$$

$$\boldsymbol{\nu}^{(r,5)} = \mathbf{0} \tag{4-18}$$

$$\boldsymbol{\gamma}^{(r,5)} = \begin{bmatrix} \boldsymbol{\gamma}^{(s,3)} \\ -2\dot{\mathbf{s}}_i^{\mathrm{T}}\dot{\mathbf{s}}_j + \dot{\mathbf{s}}_i^{\mathrm{T}}\tilde{\boldsymbol{\omega}}_i\mathbf{s}_j + \dot{\mathbf{s}}_j^{\mathrm{T}}\tilde{\boldsymbol{\omega}}_j\mathbf{s}_i \\ -2\dot{\mathbf{s}}_i^{\mathrm{T}}\dot{\mathbf{s}}_j + \dot{\mathbf{s}}_i^{\mathrm{T}}\tilde{\boldsymbol{\omega}}_i\mathbf{s}_j + \dot{\mathbf{s}}_j^{\mathrm{T}}\tilde{\boldsymbol{\omega}}_j\mathbf{s}_i \end{bmatrix}$$

4.3.4. Prescribed Motion Constraint

In the three-dimensional space, the absolute motion of the multibody system can be mathematically described by means of driving constraints that guide the position and orientation of a reference body belonging to the multibody system, over time, as illustrated in Figure 4-5.

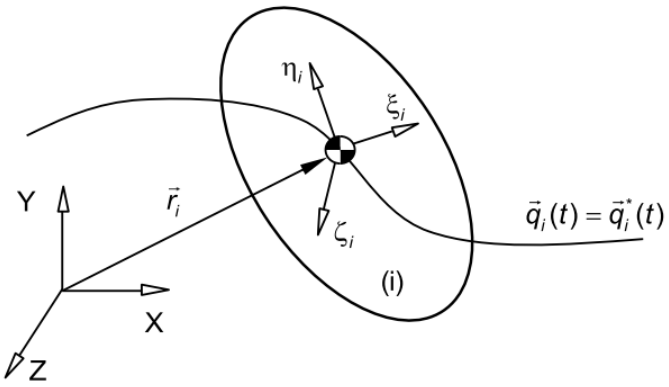

Figure 4-5: Prescribed motion constraint applied to body *i*.

The driving, or base, body is the reference for the whole multibody system. Considering the biomechanical model described in Chapter 3, the pelvis is the assigned driving element. The configuration of the driving body over time is described in Cartesian coordinates by 7 coordinates: 3 of translation and 4 Euler parameters to define the body orientation. Therefore, seven constraint equations are used to define the prescribed motion constraint:

$$\boldsymbol{\Phi}^{(pmc,7)} = \mathbf{q}_i - \mathbf{q}_i^*(t) = \mathbf{0} \tag{4-19}$$

where $\mathbf{q}_i^*(t)$ is the actual position vector of body *i* at time t.

The contribution of the prescribed motion constraint to the Jacobian matrix and to the right-hand side vectors of the velocity and acceleration constraint equations is given by:

$$\mathbf{\Phi}_{\mathbf{q}}^{(pmc,7)} = \begin{bmatrix} \mathbf{0} & \mathbf{0} & \dots & \mathbf{I} & \mathbf{0} & \dots & \mathbf{0} & \mathbf{0} \\ \mathbf{0} & \mathbf{0} & \dots & \mathbf{0} & \frac{1}{2}\mathbf{L}_i^{\mathrm{T}} & \dots & \mathbf{0} & \mathbf{0} \end{bmatrix}$$

$$\boldsymbol{\nu}^{(pmc,7)} = \dot{\mathbf{q}}_i^*(t) \tag{4-20}$$

$$\boldsymbol{\gamma}^{(pmc,7)} = \begin{bmatrix} \ddot{\mathbf{r}}_i^*(t) \\ \ddot{\mathbf{p}}_i^*(t) + \frac{1}{4}(\boldsymbol{\omega}'^{\mathrm{T}}_i \boldsymbol{\omega}'_i)\mathbf{p}_i \end{bmatrix}$$

where $\dot{\mathbf{q}}_i^*(t)$, $\ddot{\mathbf{r}}_i^*(t)$, and $\ddot{\mathbf{p}}_i^*(t)$ are the experimentally measured time dependent vectors of generalised velocities, translational accelerations, and second time derivatives of the Euler parameters of body *i*, respectively. These vectors are determined by interpolating the prescribed motion vector $\mathbf{q}_i^*(t)$ using cubic splines, for instance, and by differentiating these once and twice with respect to time to obtain, respectively, velocity and acceleration.

4.3.5. Rotational Driver

While the kinematic joints in Sections 4.3.1 to 4.3.3 constrain the relative motion of adjacent body segments, the rotational driver constraint guides the DOF of those kinematic pairs. Figure 4-6 illustrates the rotational driver constraint between bodies *i* and *j* for a given instant of time.

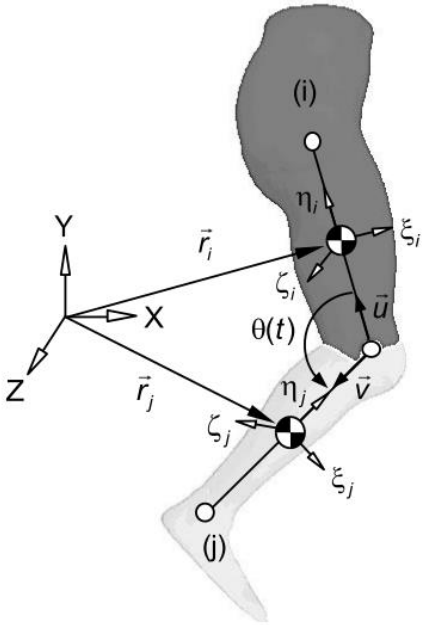

Figure 4-6: Rotational driver constraint applied between bodies *i* and *j*.

Considering the example in Figure 4-6, the mechanical motion of the human knee can be described by a revolute joint (5 DOF constrained) and a single rotational driver (the remaining DOF). The kinematic joint only allows the knee to flex and extend, and the driver controls the rotating angle variation given by $\theta(t)$. Before performing a kinematic analysis, $\mathbf{u}$ and $\mathbf{v}$ are defined at every instant of time as unitary

vectors aligned with the η_i and η_j local axes of bodies *i* and *j*, respectively, and $\theta(t)$ is determined as the angle variation between them. Since both vectors are unitary, the dot product between $\mathbf{u}$ and $\mathbf{v}$ is equal to the cosine of the angle between them. Hence, the constraint equation becomes:

$$\mathbf{\Phi}^{(rd,1)} = \mathbf{u}^{\mathrm{T}}\mathbf{v} - cos(\theta(t)) = 0, \text{ with } \theta(t) = \langle \mathbf{u}, \mathbf{v} \rangle(t) \tag{4-21}$$

The number of constraint equations increases by the same number of DOF of the kinematic pair. The contribution of the rotational driver constraints to the Jacobian matrix and to the right-hand side vectors of the velocity and acceleration constraint equations is given by:

$$\begin{aligned} \mathbf{\Phi}_{\mathbf{q}}^{(rd,1)} &= \begin{bmatrix} \mathbf{0} & \mathbf{0} & \dots & \mathbf{0} & -\mathbf{v}^{\mathrm{T}}\tilde{\mathbf{u}}\mathbf{A}_i & \dots & \mathbf{0} & -\mathbf{u}^{\mathrm{T}}\tilde{\mathbf{v}}\mathbf{A}_j & \dots & \mathbf{0} & \mathbf{0} \end{bmatrix} \\ \boldsymbol{\nu}^{(rd,1)} &= -sin(\theta(t)) \cdot \dot{\theta}(t) \\ \boldsymbol{\gamma}^{(rd,1)} &= -2\dot{\mathbf{u}}^{\mathrm{T}}\dot{\mathbf{v}} + \dot{\mathbf{u}}^{\mathrm{T}}\tilde{\boldsymbol{\omega}}_i\mathbf{v} + \dot{\mathbf{v}}^{\mathrm{T}}\tilde{\boldsymbol{\omega}}_j\mathbf{u} - cos(\theta(t)) \cdot \dot{\theta}(t)^2 - sin(\theta(t)) \cdot \ddot{\theta}(t) \end{aligned} \tag{4-22}$$

where $\dot{\theta}(t)$ and $\ddot{\theta}(t)$ are, respectively, the first and second derivatives of a cubic spline interpolation of the rotating angle variation $\theta(t)$.

4.4. Dynamic Analysis

The dynamic analysis of a multibody system consists in the study of motion when the system is subjected to externally applied forces that modify the dynamic behaviour of its components. In the field of biomechanics, dynamic analyses are performed to obtain the intersegmental joint forces, joint moments-of-force, and muscle forces of the biomechanical model. The determination of those quantities requires the establishment of the mechanical principles of a constrained multibody system in the three-dimensional space.

4.4.1. Joint Contact Forces

Each kinematic joint introduces reaction forces, also known as constraint forces, between the connected body segments. These forces can be expressed in terms of the constraint equations of the multibody system as long as they are defined with respect to the same coordinate system as the vector of generalised positions, $\mathbf{q}$ (Nikravesh, 1988). This relationship is obtained using the Lagrange multipliers method defined in Nikravesh (1988), and expressed by:

$$\mathbf{g}^{(c)} = -\mathbf{\Phi}_{\mathbf{q}}^{\mathrm{T}}\boldsymbol{\lambda} \tag{4-23}$$

where $\mathbf{g}^{(c)}$ is the generalised vector of internal contact forces, and $\boldsymbol{\lambda}$ is the vector of Lagrange multipliers. From the physical point of view, the rows of the Jacobian matrix define the direction of the constraint forces while the Lagrange multipliers define their unknown magnitudes.

4.4.2. Equations of Motion

For a general constrained multibody system, the equations of motion are given by:

$$\mathbf{M}\ddot{\mathbf{q}} = \mathbf{g} + \mathbf{g}^{(c)} \tag{4-24}$$

where $\mathbf{M}$ is the mass matrix of the system, containing the body masses and the moments of inertia of each individual anatomical segment, $\ddot{\mathbf{q}}$ is the vector of generalised accelerations, and $\mathbf{g}$ is the vector of external forces. By substituting Equation (*4-23*) into Equation (*4-24*), the equations of motion become:

$$\mathbf{M}\ddot{\mathbf{q}} + \boldsymbol{\Phi}_{\mathbf{q}}^{\mathrm{T}}\boldsymbol{\lambda} = \mathbf{g} \tag{4-25}$$

In an inverse dynamic analysis, in which the kinematic data are fully known, the equations of motion are solved for the unknown Lagrange multipliers, which are directly associated with the intersegmental joint forces and joint torques of the human body model (Silva and Ambrósio, 2003), which is further explained in Chapter 7.

The set of equations of motion of a multibody system has the vector of kinematic consistent accelerations written explicitly, as given by Equation (*4-25*). Since in an inverse dynamic analysis the kinematic data are given as input, accurate motion information is determinant in the goodness of the results obtained (Andersen et al., 2009). The methodology followed to provide the kinematic data required for an inverse dynamic analysis is described in Chapter 5.

5. Data Acquisition and Processing

When performing an inverse dynamic analysis of a complex human motion, the acquisition of three distinct types of information is required to give as input to the analysis program: anthropometric information regarding the subject performing the motion, described in Chapter 3; kinematic information, characterised by a set of trajectories of markers placed on relevant palpable bony landmarks, which is used to describe the motion of the anatomical segments, to be introduced in the current chapter; and kinetic information concerning all external forces applied on anatomical segments, including their application points, to be presented in Chapter 6.

In this dissertation, experimental data taken for a front crawl swimming motion, captured by three-dimensional motion tracking systems at the LABIOMEP-UP, is used. The data provided, containing the static and dynamic trials of the swimming motion are processed and provided as input to the LHBM for motion reconstruction. Finally, the verification of the kinematic consistency between the experimental measurements and the biomechanical model used in this work is addressed in the last section of this chapter.

5.1. Kinematic Data Acquisition

Although the kinematic data acquisition was not performed during the period of this dissertation, a brief description of the experimental setup is provided here (Andersen, 2019; Lauer et al., 2016). The experimental data collected includes the positions of anatomical landmarks of a 25-year-old male, with a height of 1.80 m, and weighing 70.3 kg, performing a front crawl swimming stroke. The subject is a healthy regional level swimmer.

The testing is conducted in a 25 m indoor swimming pool by automatically tracking the swimmer's motion with a Qualisys Track Manager system (Qualisys, Gothenburg, Sweden) at 100 Hz, using 12 above water cameras (3x Oqus 310+, and 9x Oqus 400) and 10 underwater cameras (4x Oqus 300+u, 4x Oqus 700+u, and 2x Oqus 310+u). The placement of the 22 cameras along the swimming pool is illustrated in Figure 5-1. A three-step calibration process is performed in order to synchronise the above and underwater cameras, as well as the air-water interface (Andersen, 2019). The space of interest results in a volume of approximately 28 m^3 (7 m in length, 2 m in width, 2 m in height) positioned in the middle of the swimming pool, which corresponds to the coloured rectangle in Figure 5-1. Only markers passing through the calibrated volume are detected. The global frame origin is in the midsection of the calibrated volume, at the water surface level, i.e., $Z = 0$. The orthogonal axes of the global frame define X in the lateral direction, Y in the direction of swim, and Z in the vertical direction.

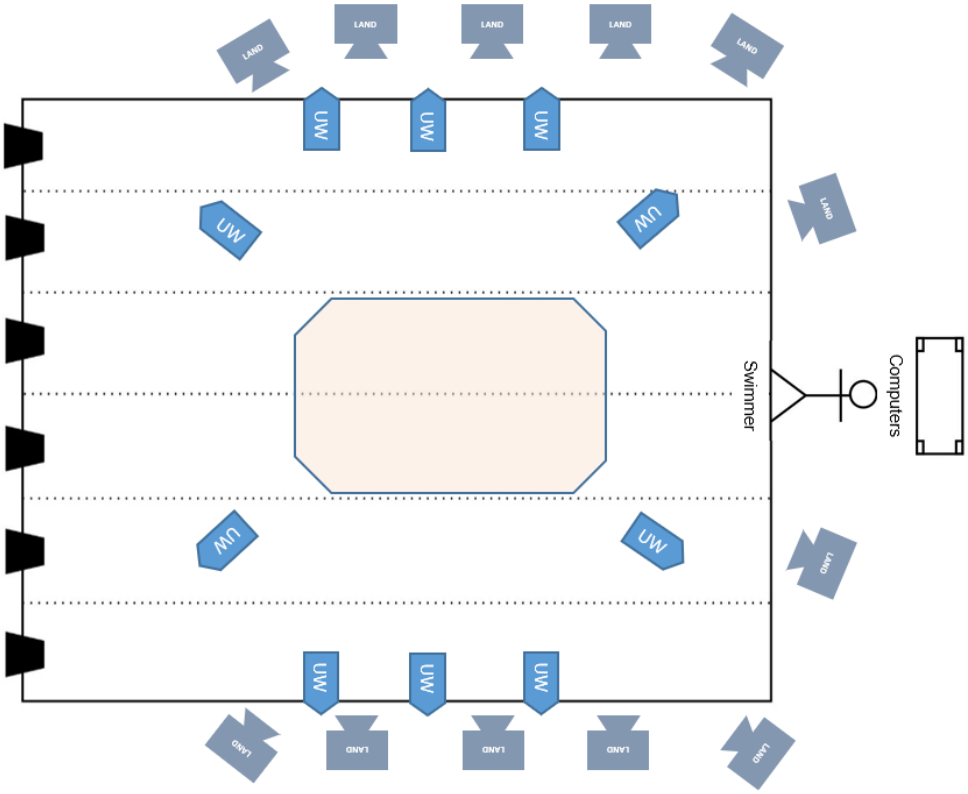

Figure 5-1: Top view configuration of the LABIOMEP-UP layout. UW stands for underwater cameras, and LAND stands for above water cameras. The coloured rectangle in the centre of the swimming pool corresponds to the calibrated volume covered by the 22 cameras.

The motion of the swimmer performing a front crawl swimming stroke is captured by tracking 66 reflective markers' trajectories placed on anatomical bony landmarks. These points consist in easily palpable places of the subject's skin, where the underlying bones are normally close to the surface. The markers set protocol used in the experimental data acquisition is fully described in Appendix A. Due to the increased drag created by the water in swimming motion applications, besides the double sided tape used to place the markers on surface skin, these are additionally fixed with an hydrophobic tape (Euroderm) to ensure resistance, and are finally covered with an adhesive tape (Omnitape) (Cascais et al., 2014).

The experimental data acquisition consists in 1) a static trial and 2) a trial containing the kinematic data of the motion under analysis:

1. The static trial consists in the collection of kinematic data of the swimmer standing in the anatomical reference position (ARP). For that, a metal frame is positioned in the middle of the calibrated volume, inside the swimming pool, where the swimmer stands stationary until data is collected. The lower limbs, including the pelvis are submersed, while the torso and upper limbs are above water. This trial is used for calibration of the experimental data and further construction of the swimmer's biomechanical model (Section 5.3).
2. The dynamic trial contains the 3D kinematic data of the front crawl swimming motion that are given as input to the kinematic analysis.

It is usual to detect some gaps in the experimental data obtained by swimming motion capture systems. One of the reasons for that is the falling of a marker from the swimmer due to the water flow. Another, more concerning, reason is associated with missing marker visibility, when a body part is blocking a marker from being recorded, or at the air-water interface as a result of the splashing (Andersen et al., 2009). In this case, spline filtering algorithms in the Qualisys Track Manager software are used to fill the missing markers trajectories (Andersen, 2019). However, it must be noted that the gap-filling may not be possible if the gap is very long, or if it occurs in the beginning or ending of the calibrated volume data acquisition.

5.2. Data Filtering

The accuracy of the motion data captured experimentally has a major impact on the output of a dynamic analysis (Andersen et al., 2009). However, experimental procedures and motion tracking systems are naturally susceptible to noise and kinematic deviations. Despite the errors associated with the measurement equipment, the main source of noise occurs due to soft tissue artefacts, which consist in the sliding of markers with the skin relative to the bones. The presence of this high-frequency noise in the kinematic positions is even more problematic when considering the double differentiation of the vector of consistent positions to obtain the accelerations of the multibody system, since it appears directly in the equations of motion (Winter, 2009). Therefore, instead of the double differentiation referred, the velocities and accelerations are obtained, in this work, via the velocity and acceleration constraint equations.

The kinematic data are filtered to reduce the noise without affecting the description of the motion performed. The data provided by LABIOMEP-UP are already filtered in the Qualisys Track Manager software with a 5-frame moving average filtering technique. Nonetheless, considering the works of Andersen (2019) and Lauer et al. (2016), an additional filtering is performed. Thus, the kinematic data are filtered using a 2^{nd} order Butterworth low-pass filter, and the cut-off frequencies are determined through a residual analysis (Winter, 2009). This allows the selection of the optimal cut-off frequency that better suits the noise level of each marker.

5.3. Motion Reconstruction

Consistency between both laboratorial and model data must be guaranteed to ensure a proper simulation of the acquired data. The anthropometric measurements listed in Table 3-1 were obtained by applying the anatomical information of the swimmer subject to the scaling equations of Dumas et al. (2007a, 2007b).

Considering the experimental setup protocol followed in LABIOMEP-UP (Figure A-1), markers are usually placed in the human body near anatomical articulations and extremities of body segments. Therefore, the kinematic data containing the positions of the markers are used to define the joint centres of the biomechanical model. The body-fixed reference frames are defined according to the ISB

recommendations (Wu et al., 2002, 2005), where at least three markers are used to define each body orientation.

As discussed in Chapter 2, the kinematic data provided by LABIOMEP-UP were acquired before the development of this dissertation, with the purpose of creating a realistic 3D avatar performing the front crawl swimming motion. However, in this work, the kinematic data are required to define the joint centres and extremities of body segments. Therefore, from the total of 66 reflective markers measured in the laboratory, only 38 are used to define the biomechanical model, according to Table A-1 which contains the information about the markers to be used. The elbow, wrist, knee, and ankle joint centres are estimated as the midpoint between two reflective markers (Dumas et al., 2007a, 2007b). The same procedure is used to determine the distal points of the hands and feet. The distal point of the head is given by the position of the marker labelled as HEADTOP. For the joints of the human skeleton that cannot be accessed by palpation, such as the hip, lumbar, cervical, shoulder, and atlanto-occipital joints, their centres are determined by means of predictive equations. Predictive methods consist of non-invasive ways of determining anatomical joint centres using anthropometry based regression equations (Murphy et al., 2011). Naturally, the selection of a predictive method over another depends on the experimental data available.

Dumas et al. (2007a) recommended the estimation of the hip joint centre (HJC), lumbar joint centre (LJC), cervical joint centre (CJC), and shoulder joint centre (SJC) based on the regressions defined by Reed et al. (1999). These equations are preferred over other methods since they are all based on the same anatomical landmarks as those of McConville et al. (1980), from which the anthropometric scaling equations were determined. Furthermore, they make distinctions between genders. However, because not all anatomical landmarks required for the estimation of the HJC, LJC, and SJC are available in the experimental data provided by LABIOMEP-UP, only the estimation of the CJC follows the definition of Reed et al. (1999).

5.3.1. Estimation of the Hip Joint Centre

The location of the HJC is an important aspect of biomechanical modelling for several human movements since it is the origin point for hip rotation. Accordingly, the prediction accuracy has a direct repercussion in the interpretation of kinematic results and internal contact forces (Hara et al., 2016). Hara et al. (2016) propose a set of regression equations to estimate the location of the HJC. The study evaluate whether the accuracy of the hip contact forces is improved by considering different anthropometric measurement predictors.

Leg length, defined as the distance from ASIS to medial malleolus passing through the medial epicondyle of the femur, is found to be the best single predictor. Hara et al. (2016) identify this measurement as the less affected by the thickness of soft tissues when compared to the pelvic depth and pelvic width used by other authors (Harrington et al., 2007). The leg length measurement is depicted in Figure 5-2.

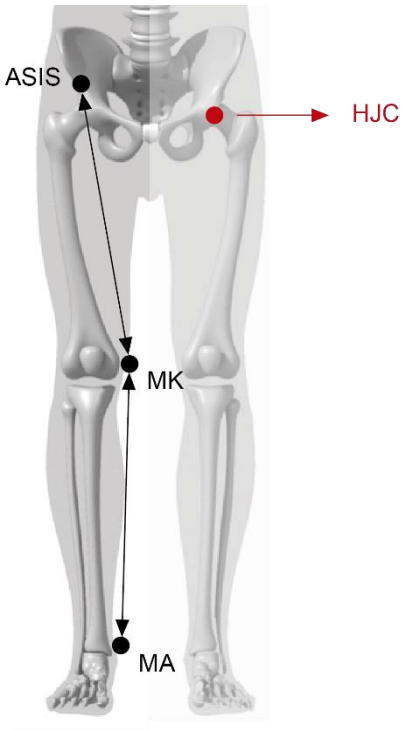

Figure 5-2: Estimation of the hip joint centre. Leg length as the distance from ASIS to medial malleolus (MA) passing through the medial epicondyle of the femur (MK).

Consequently, the estimation of the HJC in the pelvis body-fixed reference frame is given by Equation (*5-1*):

$$\begin{aligned} &\text{Posterior-anterior direction:} && HJC_{\xi} = 11 - 0.063LL \\ &\text{Inferior-superior direction:} && HJC_{\eta} = -9 - 0.078LL \\ &\text{Medial-lateral direction:} && HJC_{\zeta} = 8 + 0.086LL \end{aligned} \tag{5-1}$$

where LL is the leg length measured in millimetres, and ξ, η, and ζ are the direction axes of the pelvis coordinate system according to (Wu et al., 2002). Note that Hara et al. (2016) defines the origin of the pelvis coordinate system as the midpoint between RASIS and LASIS, similar to the definition in this work, as seen in Figure 3-2.

5.3.2. Estimation of the Lumbar Joint Centre

The understanding of the kinematics and internal kinetics of the pelvis-lumbar complex is of great interest for the prevention of lower back pain injuries (Murphy et al., 2011). Moreover, for swimming applications, the pelvis and torso anatomical segments play an important role with respect to body coordination, posture, and spine stability to enhance performance during motion (Andersen, 2019).

Murphy et al. (2011) proposed two sets of regression equations to predict the location of the LJC via a non-invasive protocol. Both proposals consider the location of palpable surface landmarks on the pelvic bone, which are used to define three distances in the body local axis system: pelvic depth is the distance from the midpoint between RASIS and LASIS to the midpoint between RPSIS and LPSIS; anterior pelvic width is the distance from RASIS to LASIS; and posterior pelvic width is the distance from RPSIS to

LPSIS. The authors found that the most effective way to estimate the LJC utilised pelvic depth and anterior pelvic width, which are represented in Figure 5-3.

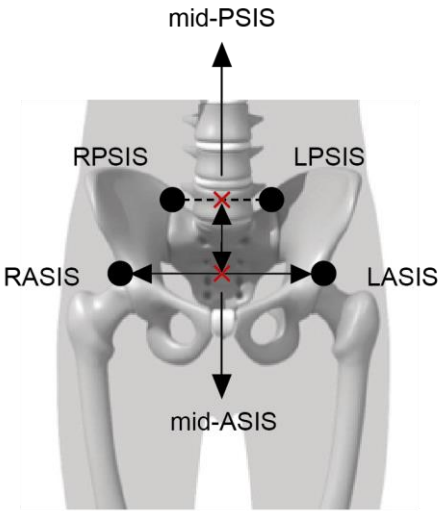

Figure 5-3: Pelvic depth as the distance from the midpoint between RASIS and LASIS to the midpoint between RPSIS and LPSIS, and anterior pelvic width as the distance from RASIS to LASIS.

The resulting equations, described in the pelvis body-fixed reference frame, are given by:

$$\begin{aligned} &\text{Posterior-anterior direction:} && LJC_{\xi} = -0.7006PD \\ &\text{Inferior-superior direction:} && LJC_{\eta} = 0.0349APW \\ &\text{Medial-lateral direction:} && LJC_{\zeta} = -0.0045PD \end{aligned} \tag{5-2}$$

where PD is the pelvic depth, APW is the anterior pelvic width, and ξ, η, and ζ are the direction axes of the pelvis coordinate system according to Wu et al. (2002). Like in this work (Figure 3-2), Murphy et al. (2011) defines the origin of the pelvis coordinate system as the midpoint between RASIS and LASIS.

5.3.3. Estimation of the Cervical Joint Centre

The estimation of the CJC follows the calculation methods of Reed et al. (1999). Contrary to the methods used for the estimation of the HJC and JLC, the method proposed by Reed et al. (1999) is not defined locally. Instead, its calculation is obtained using the markers of the 7th cervical vertebrae (C7) and the first marker of the sternum cluster (ST1) measured in the global reference frame.

Reed et al. (1999) assume the location of the CJC to be symmetric in the sagittal plane, which means that the component in X is the average between the X coordinates of the C7 and ST1 surface landmarks. Regarding the Z and Y components of the CJC, they are obtained by rotating the vector that goes from C7 to ST1 in the sagittal plane upward by 8º. Then, this vector is scaled to have a length equal to 55% of the measured distance from C7 to ST1, as shown in Figure 5-4.

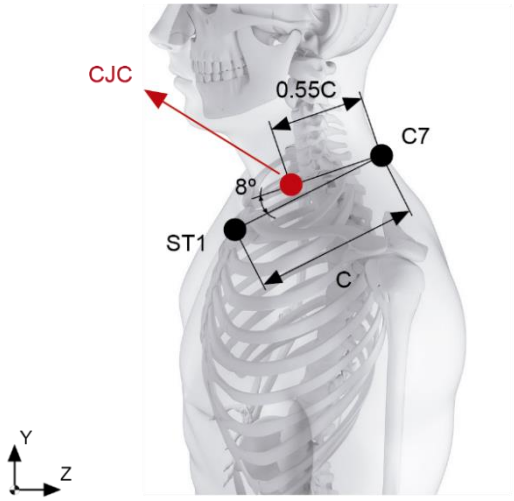

Figure 5-4: Estimation of the cervical joint centre on the sagittal plane, measured in the global reference frame.

5.3.4. Estimation of the Shoulder Joint Centre

Pàmies-Vilà (2012) developed a complete set of equations to determine the joint centres of rotation of the entire 3D biomechanical model. However, in this work, only the SJC and OJC are determined based on the equations of Pàmies-Vilà (2012), since the remaining HJC, LJC, and CJC require the position of markers that are not used in the protocol of LABIOMEP-UP. The estimation of the right and left SJC uses the markers of the right and left acromion, RAC and LAC, respectively, and the estimation of the LJC, as depicted in Figure 5-5.

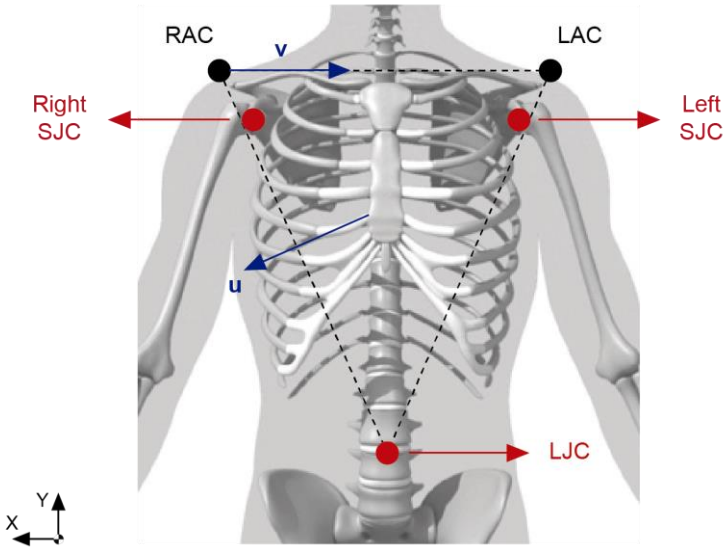

Figure 5-5: Estimation of the shoulder joint centre in the global reference frame. The vector $\mathbf{v}$ goes from RAC to LAC, and $\mathbf{u}$ is the vector perpendicular to the plane defined by LJC, LAC, and RAC. $\mathbf{u}$ and $\mathbf{v}$ are unitary vectors.

The expression used to compute the right and left SJC in the global frame is given by:

$$\begin{aligned} &\text{Right SJC:} && \mathbf{SJC} = \mathbf{r}_{RAC} - 0.02\mathbf{v} - 0.05\mathbf{w} \\ &\text{Left SJC:} && \mathbf{SJC} = \mathbf{r}_{LAC} + 0.02\mathbf{v} - 0.05\mathbf{w} \end{aligned} \tag{5-3}$$

where $\mathbf{r}_{RAC}$ and $\mathbf{r}_{LAC}$ are the coordinates of the RAC and LAC markers, respectively, and $\mathbf{u}$, $\mathbf{v}$, and $\mathbf{w}$ are unitary vectors. The vector $\mathbf{v}$ goes from RAC to LAC, $\mathbf{u}$ is the vector perpendicular to the plane defined by LJC, LAC, and RAC, and $\mathbf{w}$ is the cross product between $\mathbf{u}$ and $\mathbf{v}$.

5.3.5. Estimation of the Atlanto-occipital Joint Centre

Similarly to the estimation of the SJC, the location of the OJC is computed according to the set of regression equations defined by Pàmies-Vilà (2012). The calculation method uses the markers of the top of the head, right head, and left head, represented in Figure 5-6.

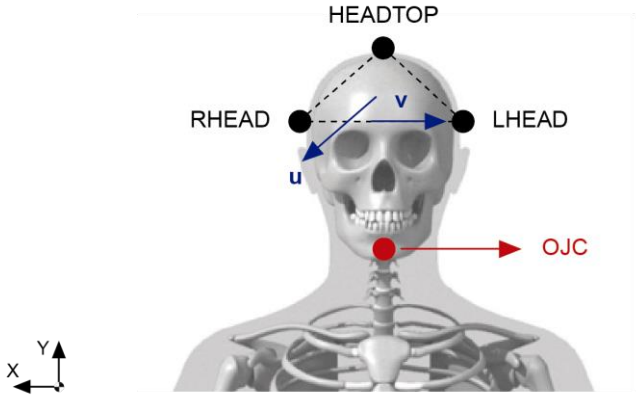

Figure 5-6: Estimation of the atlanto-occipital joint centre in the global reference frame. The vector $\mathbf{v}$ goes from RHEAD to LHEAD, and $\mathbf{u}$ is the vector perpendicular to the plane defined by HEADTOP, RHEAD, and LHEAD. $\mathbf{u}$ and $\mathbf{v}$ are unitary vectors.

Accordingly, the position of the OJC is given by:

$$\mathbf{OJC} = 0.5(\mathbf{r}_{RHEAD} + \mathbf{r}_{LHEAD}) - 0.04\mathbf{u} - 0.1\mathbf{w} \tag{5-4}$$

where $\mathbf{r}_{RHEAD}$ and $\mathbf{r}_{LHEAD}$ are the coordinates of the RHEAD and LHEAD markers, respectively, $\mathbf{u}$, $\mathbf{v}$, and $\mathbf{w}$ are unitary vectors. The vector $\mathbf{v}$ goes from RHEAD to LHEAD, $\mathbf{u}$ is the vector perpendicular to the plane defined by HEADTOP, RHEAD, and LHEAD, and $\mathbf{w}$ is the cross product between $\mathbf{u}$ and $\mathbf{v}$.

5.4. Application to the Front Crawl Swimming Stroke

In front crawl swimming, one stroke cycle is defined as the period between consecutive entries of one same hand into the water (Andersen, 2019). Each stroke cycle is typically divided into three phases: pull, push, and recovery. The pull phase is further divided into two events (entry and stretch, and downsweep), as well as the push phase (insweep and upsweep) (Davies et al., 2009; Samson et al., 2017). The segmentation of the stroke cycle uses the position of the hand relative to the swimmer's

body or to the water surface to identify the different phases (Cortesi et al., 2019). The characteristics of each event are as follows:

- **Entry and Stretch:** the entry and stretch is the initial event of the stroke during which the swimmer sets up the arms and body to develop as much thrust as possible. The hand palm is pointed straight down at the bottom of the swimming pool to initiate the pull (Wei et al., 2014).
- **Downsweep:** immediately after entering the water, the swimmer's hand moves backwards and downwards until reaching the deepest point.
- **Insweep:** the insweep begins with the hand at its deepest position. The arm, forearm, and hand are vertically positioned with respect to the swimming direction, resulting in more work developed in propelling the body forward using the resistance of the water (Davies et al., 2009; Samson et al., 2017).
- **Upsweep:** the upsweep is the second most propulsive phase (Samson et al., 2017). It is initiated when the hand starts moving outwards until leaving the water.
- **Recovery:** the stroke cycle ends by moving the hand forward, overhead out of the water, to initiate the next stroke. During the recovery phase the swimmer rolls the body to the same side of the arm stroke and breathing occurs by slightly turning the head to the side. The rotation is used to propel the body forward.

The complete front crawl stroke cycle is illustrated in Figure 5-7. During the entire stroke, the lower limbs perform an alternate rhythmical movement upwards and downwards, denoted as flutter or leg kick (Guignard et al., 2019). The downbeat consists in the motion towards the bottom of the swimming pool and begins with the flexion at the hip, followed by extension at the knee. In a wave-like motion, the thigh moves down first, followed by the leg and then the foot. Right before the transition to the ascending movement, the foot reaches the deepest point of its path at maximum plantarflexion. The upbeat is initiated again with the thigh moving upwards and creating a slight hyperflexion in the knee (Keys, 2010).

Entry and Stretch	**Downsweep**	**Insweep**	**Upsweep**	**Recovery**
Pull Phase (Underwater)		Push Phase (Underwater)		Recovery Phase (Above water)
65%				35%

Figure 5-7: Front crawl swimming stroke phases. The figure illustrates one full stroke cycle for the right hand (adapted from Ceccon et al. (2013)).

The front crawl technique is characterised by several aspects, such as on the underwater movement of the hand during the propulsive phase, which can present an "S"-shaped or an "I"-shaped path (Sanders et al., 2017; Takagi et al., 2015; Wei et al., 2014), the frequency between upper and lower limb coordinated movements, i.e., number of leg kicks per number of arm strokes (Guignard et al., 2019), or even the swimming stroke rate (Matsuda et al., 2016). In front crawl swimming, swimmers change their

velocity and stroke rate according to the swimming distance. For training and long-distance races, more energy-efficient techniques are preferred over those performed on sprint races (Hall, 2020). A shoulder-driven technique enables swimmers to swim at a much higher stroke rate and therefore move at a higher speed for a short duration. The forearm is released much quicker from the water surface with very low rotation of the torso which leads to higher stresses on the shoulders (Walker, 2020). To reduce the risk of injury, a hip-driven technique is used alternatively to a shoulder-driven technique whenever possible. Although it is not the fastest technique, it helps taking pressure off the shoulders. During the hip-driven front crawl swimming, the hip is kept near the water surface which leads to less water resistance (TritonWear, 2020; Walker, 2020). To compensate for the lower stroke rate, hip rotation is used as a power source for propulsion and to help maintain a streamlined body position. The kinematic data used in this dissertation to study the front crawl swimming were captured from a swimmer performing the hip-driven technique.

5.4.1. Results and Discussion

From the motion collected at LABIOMEP-UP, the swimmer performed three complete strokes, consisting of two right-hand strokes and one left-hand stroke. The left-hand stroke is selected to be studied in this dissertation since it has the shortest cycle time among the others and, most importantly, no loss of reflective markers registration during that period has been observed. Table 5-1 outlines the temporal key events measured in LABIOMEP-UP throughout the left-hand stroke cycle.

Table 5-1: Critical temporal events during one left-hand front crawl swimming stroke measured in LABIOMEP-UP.

Stroke phase	Time [s]	Time [%]	Description
Entry and Stretch	0.00	0	Left hand enters the water
	0.06	2.5	Left foot reaches top as right foot reaches bottom of sweep
	0.18	7.5	Right hand reaches the deepest point
	0.54	22.6	Left foot reaches bottom as right foot reaches top of sweep
	0.78	32.6	Right hand exits the water
Downsweep	0.96	40.2	Left foot reaches top as right foot reaches bottom of sweep
	1.01	42.3	Left hand starts moving downwards
	1.16	48.5	Right hand enters the water
	1.28	53.6	Left foot reaches bottom as right foot reaches top of sweep
Insweep	1.37	57.3	Left hand reaches the deepest point
	1.62	67.8	Right foot reaches bottom of sweep
Upsweep	1.73	72.4	Left hand moves outwards
	1.75	73.2	Left foot reaches top of sweep
Recovery	1.95	81.6	Left hand exits the water
	2.18	91.2	Left foot reaches bottom as right foot reaches top of sweep
	2.39	100	Left hand imminent to enter the water

The cycle time varies according to the swimmer's performance and the swimming race. For high level swimmers performing a 200-m front crawl, Sanders and Psycharakis (2009) reports an estimated cycle time of about 1.4 s, while Nakashima et al. (2007) records a stroke cycle of 1.96 s. A cycle time of 2.39

s is registered for the left-hand stroke, which is substantially higher than those reported in the literature, even though it is not recorded at the same maximal sprint race conditions.

The joint angles obtained after the kinematic analysis are compared against the data of Nakashima et al. (2007), as shown in Figure 5-8. Nakashima et al. (2007) recorded the motion of a 20-29-year-old swimmer male, performing the front crawl technique and the joint motion was constructed based on video imaging. The manual reconstruction procedure introduced errors of about ±15º in the data reported by Nakashima et al. (2007). In both works, the left-hand stroke is analysed. Since this dissertation is focused on the human lower limbs, more emphasis is given to the flexion and extension of the hip, knee, and ankle joints, which are the main motions that characterise the leg kick (Matsuda et al., 2016).

(a)

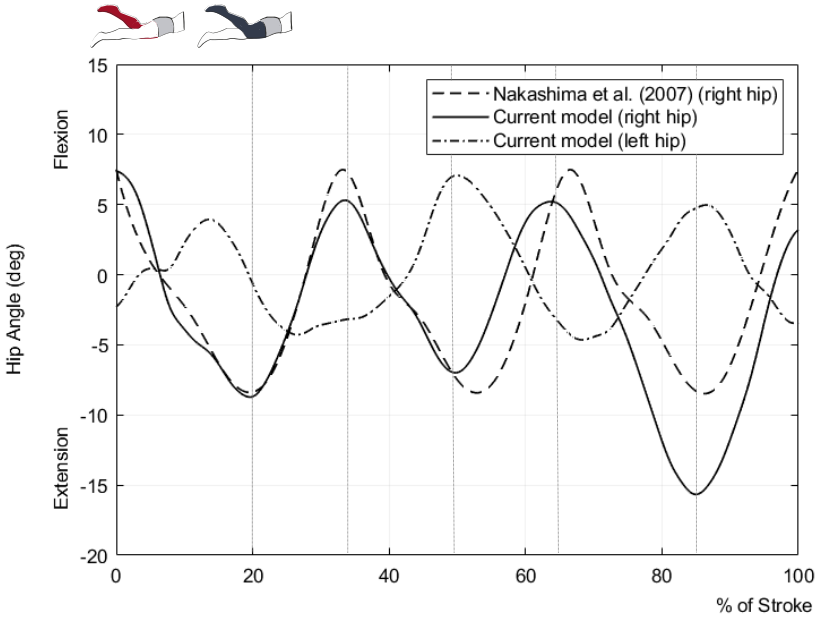

(b)

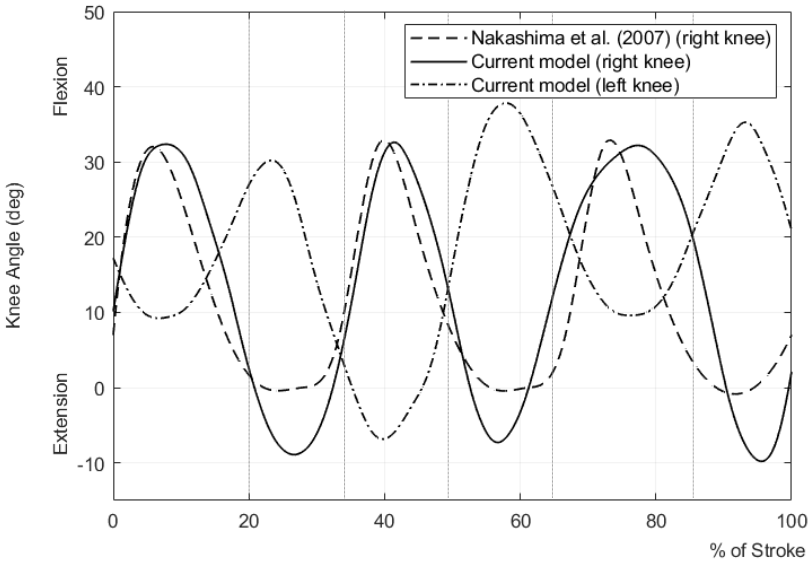

Figure 5-8: Joint angles obtained for a left-hand six-beat front crawl swimming stroke cycle performed by a male swimmer in LABIOMEP-UP (solid and dash-dotted lines): (a) hip joint, (b) knee joint and (c) ankle joint. Data of the right lower limb reported by Nakashima et al. (2007) (dashed line) is also presented for the sake of comparison. The horizontal axis corresponds to a percentage of the stroke cycle.

(c)

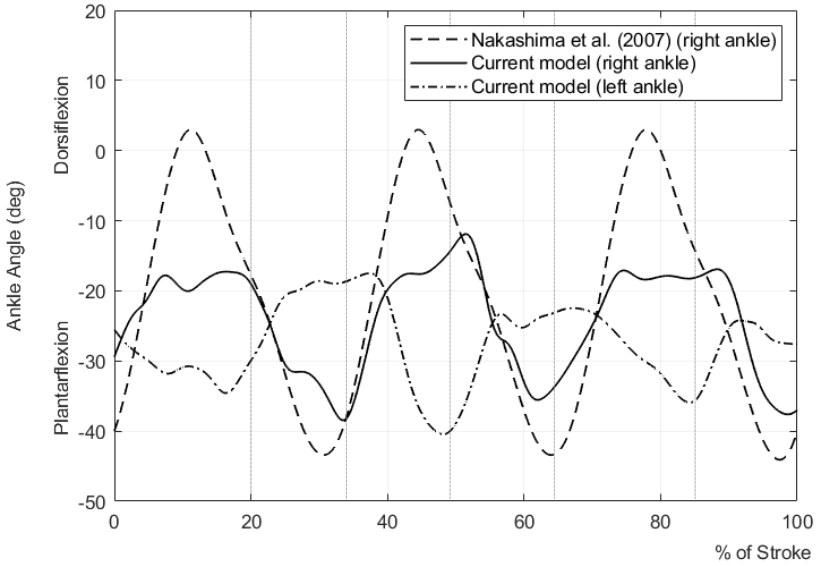

Figure 5-8: (cont.)

Three peaks and three valleys can be identified for all joints. This behaviour is related to the number of leg kicks per arm strokes, defined as the frequency ratio. In this case, for one arm stroke, i.e., one cycle, the swimmer performs three upbeats and three downbeats in each leg, which means that the motion performed is a six-beat front crawl swimming stroke. This is actually the most common technique used in front crawl swimming (Guignard et al., 2019) and the most appropriate for a hip-driven style since it allows the swimmer to move faster and propel the body forward, compensating for the lower stroke rate (TritonWear, 2020). Besides, the alternate movement of the leg kick in the current model is verified in Figure 5-8 between right (solid line), and left (dash-dotted line) sides, with small discrepancies in amplitude.

The hip and knee joint angles, shown in Figure 5-8(a) and Figure 5-8(b), respectively, are in good agreement with the literature in terms of amplitudes and phases. During the leg kick, each downbeat is expected to be coordinated with one of the three hand sweeps that composes the underwater arm stroke (Guignard et al., 2019). When the left hand is positioned to initiate the pull (0-15%), the first downbeat is performed by the ipsilateral leg (left leg), which causes extension of the left knee and flexion of the left hip, while the opposite leg moves upwards. The beginning of the push phase (53%) is coordinated by the downbeat of the contralateral leg (right leg), which causes extension of the right knee and flexion of the right hip. Finally, the upsweep is performed at the same time as the last downbeat of the ipsilateral leg (72-81%), meaning that during this time the right leg performs the upbeat.

Regarding the ankle joint, Figure 5-8(c) shows that the motion alternates between increasing and decreasing rotation in the direction of a plantar-flexed position. Higher plantar-flexed angles correspond to the downbeat sequences, in the direction of hip flexion, while lower angles occur during the upbeat, in the direction of hip extension. The alternating ankle joint motion is performed as a strategy to maximise the generation of thrust, since the downbeat is the propulsive sequence of the leg kick (Guignard et al., 2019). Hence, the contact surface area of the foot with the water is increased during the downbeat by plantar flexing the foot to its maximum amplitude, while during the upbeat the foot should hang loosely

to not counteract propulsion. The results in Figure 5-8(c) are consistent with this in strategy since the maximum plantarflexion of the left ankle occurs at approximately 19%, 50%, and 87% of the stroke cycle, corresponding to the transition between down to up kick of the left leg, represented by the peaks in Figure 5-8(a). Although the motion amplitude differs between the current data and that reported by Nakashima et al. (2007), with 26.5º variation in the right ankle and 23º variation in the left ankle versus 40.4º, respectively, the phase correlation of the right ankle peaks and valleys shows a similar pattern. A different work performed by Keys (2010) for a six-beat front crawl swimming obtained variations in the ankle flexibility of 35.3º in the right ankle compared to 42.1º in the left ankle. However, the intra-cycle variation registered peak plantarflexion angles varying by as much as 20º on some kicks, which supports the non-stationary profile of the ankle variation obtained in this work.

In general, the results obtained for the joint angles are consistent with the expected upper to lower limb coordinated dynamics reported in the literature (Guignard et al., 2019; Sanders et al., 2017). However, the joint motion profile in Figure 5-8(c) shows the existence of small oscillations at each peak of both right and left ankle joints, when the respective leg kicks upwards. During the upbeat, the foot is closer to the water surface. The difficulties associated with the measurement of the position of the reflective markers through two different mediums, of air and water, are widely depicted in the literature, representing one of the biggest limitations of motion capture systems for water motion recording (Honda et al., 2012; Keys, 2010). Since the biomechanical model is formulated based on the location of these markers, some irregularities are likely introduced in the 3D kinematic data of the markers of the foot due to refraction and surface turbulence. Nevertheless, it is interesting to note the lag between corresponding peaks and valleys of the hip, knee, and ankle joints. Regardless of its descending or ascending movement, the leg kick is described as a wave-like-motion, in which the thigh moves first, followed by the leg and then the foot. Accordingly, the transition between up and downbeats, is first imposed by the hip, and followed by the knee and ankle joints.

Besides the rotation that occurs at the hip, knee, and ankle joints about the lateral axis of the thighs, legs, and feet (Figure 5-8), respectively, additional rhythms associated with the rolling action of the trunk around its longitudinal axis, defined as body roll, seems to have important functions in swimming motion (Psycharakis and Sanders, 2008). Body roll facilitates the breathing action and influences the hand displacement relative to the water, thereby contributing to arm stroke velocity. Moreover, it helps to maintain a streamlined body position, and reduces drag by decreasing the frontal surface area of the body in the direction of motion (Barber, 2013; Psycharakis and Sanders, 2008). Several authors reported that swimmers tend to rotate their shoulders considerably more than the hips due to the increased mobility of the shoulder girdle compared to the pelvic girdle. Therefore, a separate calculation of body roll in terms of shoulder roll and hip roll is preferred (Andersen, 2019; Barber, 2013; Psycharakis and Sanders, 2008). Figure 5-9 shows the roll-time profile of the shoulders and hips obtained with the experimental data collected in LABIOMEP-UP. The calculation adopted to determine shoulder and hip roll is detailed in the work of Psycharakis and Sanders (2008). Briefly, it consists in measuring the angle between the vertical global axis, Z, and the projection of the normal to the plane of the shoulder/trunk, or hip/trunk, respectively, onto the transverse ZX plane.

(a)

(b)

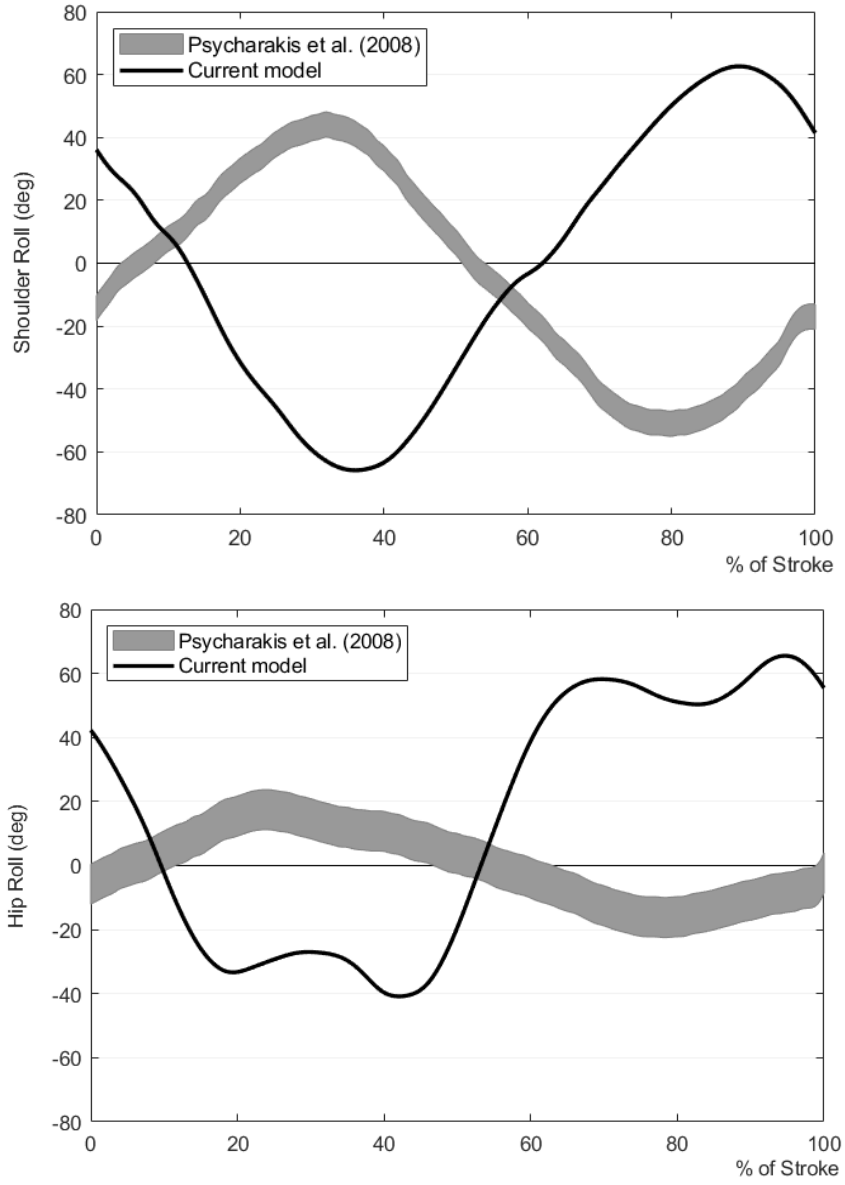

Figure 5-9: Body roll obtained for a six-beat front crawl swimming stroke cycle performed by a male swimmer in LABIOMEP-UP (solid line) and compared with the literature (shaded line): (a) shoulder roll and (b) hip roll. The solid and shaded lines represent, respectively, a left-handed and a right-handed stroke. The horizontal axis corresponds to a percentage of the stroke cycle.

The results obtained are compared with the experiments of Psycharakis and Sanders (2008), displayed as shaded curves in Figure 5-9, who established the rhythm characteristics of ten skilled front crawl male swimmers performing the 200-m front crawl swimming using a six-beat kick. The experiment was performed at a maximal effort and all subjects were instructed not to breath throughout the calibrated recording zone.

On average, the roll angles obtained for shoulder roll, depicted in Figure 5-9(a), and hip roll, shown in Figure 5-9(b), changed in a rhythmic pattern during the stroke cycle. In both cases it appears to exist symmetry with respect to the abscissa between the data reported in the current work and that in Psycharakis and Sanders (2008). This is due to the hand-stroke being analysed, noticing that this study is conducted for the left-hand stroke, while Psycharakis and Sanders (2008) studies the right-hand side.

However, since front crawl is a cyclic motion, the body roll to right and left sides is lagged by half cycles. In Figure 5-9, positive and negative angles represent rolling to the left and right side, respectively, i.e., clockwise and counter clockwise directions about the swimmer's longitudinal axis.

The results obtained for shoulder roll, shown in Figure 5-9(a), are generally in good agreement with the literature. As the left hand enters the water, the roll angle decreases until its maximum absolute magnitude, that occurs at approximately 38% of the stroke. During this period, the body rolls to the right side, counter clockwise rotation, while the right arm is moving out of the water. After the right arm reaches its highest point, the body roll decreases until the swimmer's body neutral position (0º). The rolling direction changes to the opposite side, i.e., in the clockwise direction, during the insweep of the left arm (62%). Once again, the maximum roll angle occurs during the recovery phase of the left arm, while it moves out of the water. The same pattern is observed in the study of Psycharakis and Sanders (2008), but instead of rolling first to the right, and then to the left side, the swimmer rotates in the opposite direction. The magnitudes of total shoulder roll angle, i.e., left plus right sides, found in this work range between -65º and 62º, corresponding to an amplitude of approximately 130º. Psycharakis and Sanders (2008) report a mean amplitude of 106.6º±8.4º.

For the hip roll, the computed angles are considerably greater than those presented by Psycharakis and Sanders (2008). The total amplitude of the hip roll angle in the current model is 107º, which is more than twice the magnitude of 50.4º±12.3º reported by Psycharakis and Sanders (2008). This difference in results is likely due to the instruction given to swimmers not to breath during the motion acquisitions performed by Psycharakis and Sanders (2008). Barber (2013) studies the effect of breathing on hip roll asymmetry on which experimental data are collected for twenty males and females performing the 100-m front crawl swimming at sub-maximal speed. The amplitudes found by Barber (2013) are between 108.3º-118.8º, which is consistent with the results found here. Furthermore, the profile of the hip roll shows two oscillations during 20-40% and 70-90% of the stroke, when the swimmer's body is rolling to his right and left sides, respectively. During these intervals, the swimmer performs a downbeat with the right leg, and a downbeat with the left leg, respectively. A possible reason for these small oscillations is the instantaneous kicking action of the leg, which acts in the opposite direction in which the body rotates. At the time the swimmer starts rolling his body to his right side, the first downbeat is performed with the left leg, shown in Figure 5-8(a) by left hip flexion. At approximately 20% of the stroke cycle, the body continues rolling to the right (negative hip and shoulder roll angles). However, the right hip starts flexing to initiate the first downbeat with the right leg. As the kick is an accelerated movement, the right hip is instantaneously forced downwards. The same is expected to happen, but in the opposite direction, when the body rolls to his left side and the last downbeat with the left leg is initiated (~70%).

Shoulder and hip rolls are usually analysed in terms of their magnitude, timing differences, bilateral asymmetries, and the impact of swimming velocity (Barber, 2013; Psycharakis and Sanders, 2008). On the four strokes performed, Psycharakis and Sanders (2008) observed that swimmers decreased their velocity during the test, and that hip roll was higher on the last stroke. Barber (2013) justifies the referred differences in swimming speed as a factor contributing to the higher hip roll amplitudes. Similarly, the swimming motion performed in this study was not conducted at maximal speed, which may explain the

discrepancies in total hip roll amplitudes observed. Furthermore, the deviations in hip roll magnitudes are more significant than those in shoulder roll, i.e., the shaded area is larger in Figure 5-9(b) than in Figure 5-9(a), even for skilled swimmers. Another contributing factor for the higher rolling amplitude of the pelvic girdle obtained for the data collected in LABIOMEP-UP may be related with bilateral asymmetry, namely due to breathing during the recovery phase. On his work, Barber (2013) found that total hip roll angle is significantly higher when breathing occurs. Finally, the timings of the shoulder roll and hip roll peak values is consistent with the literature, confirming that there is no out of phase between shoulder and hip rolling (Psycharakis and Sanders, 2008).

The fact that shoulder and hip rolls offer a very complete insight on the overall body kinematics makes these two important parameters that contribute to swimming performance. The most evident difference between shoulder roll and hip roll is usually related with the range of motion, indicating that there is a relative rotation between the upper and lower trunk (Psycharakis and Sanders, 2008). Even though that difference was not has high in this work has reported by Psycharakis and Sanders (2008), a difference of 23º was measured between shoulder roll and hip roll. This supports the discretisation of the biomechanical model in Chapter 3, namely the division of the human trunk in an upper and lower part, i.e., torso and pelvis, respectively.

6. Estimation of the Hydrodynamic Forces During Front Crawl Swimming

Water-based activities have received substantially less attention regarding the dynamics of human motion. The main reason for that is justified by the inherent difficulty in determining the external forces acting upon the human body in an aquatic environment. Although advances have been made in the development of pressure measurement equipment, their application is still very limited to specific body segments. Moreover, they do not precisely reflect the instantaneous points of force application (Lauer et al., 2016). Alternative methods based on numerical analysis represent the most promising alternative to overcome these difficulties.

6.1. Forces in Swimming

Swimmers move their limbs through the water to propel themselves forward. In an aquatic environment, the swimmer pushes off against a nonfixed environment, which is brought into motion because of the swimmer's actions. The combining movements of the upper and lower limbs generate hydrodynamic forces, which contribute to the swimmer's forward motion (van Houwelingen et al., 2017). In front crawl swimming, about 10-15% of the total body propulsion is due to the kicking motion of the lower limbs, while the remaining 85-90% comes from the contribution of the arm stroke (Cohen et al., 2015; Guignard et al., 2019; Mullen, 2018). Swimming hydrodynamics consists of the application of the physical principles of fluid dynamics to describe how water interacts with the body during swimming and quantify the external forces acting upon the body.

The fluid forces acting upon a swimmer's body under motion are generally of four types: (1) propulsive forces, which are related to the thrust and forward movement (positive forces); (2) resistive forces, which act opposite to the swimming direction (negative forces); (3) buoyancy forces, resulting from the reaction exerted by a fluid over a floating body; and (4) inertial forces, which are mostly related to the unsteadily fluid effects of human swimming. The force mechanisms that contribute to each type are described next.

Both upper and lower limbs produce thrust by three main mechanisms: propulsive drag, lift forces, and vortices. Newton's third law of motion accounts for forward propulsion from hydrodynamic reaction forces when portions of water mass are accelerated backwards. It is the case of the underwater arm stroke, when the arm, forearm, and hand move in the opposite direction of the body's motion, pulling the water backwards. Consequently, a reaction drag force is produced in the forward direction. The underwater trajectories of the body segments generally describe sculling movements, generating lift forces that act perpendicularly to the fluid flow, contributing to propulsion as well (Mullen, 2018).

Mathematically, the propulsive drag and lift forces are given by (Hall, 2012):

$$F_{D,L} = \frac{1}{2} C_{D,L} \rho A_p U^2 \tag{6-1}$$

where $C_{D,L}$ is the drag and lift coefficients, respectively, ρ is the fluid density (for the water: $\rho \cong 1000\ kg/m^3$ at 20°C and standard atmospheric pressure), A_p is the projected area of the body or the surface area of the body oriented perpendicular to the fluid flow, and U is the velocity of the body relative to the fluid. Drag and lift coefficients are dimensionless quantities that depend on the body's shape and flow characteristics (van Houwelingen et al., 2017). From Equation *(6-1)*, the magnitude of these two forms of thrust increase linearly with the propulsive surface area (meaning that more water is displaced), and with the square of the instantaneous velocity of the body segments. For this reason, swimmers tend to increase the speed of the hands and feet during underwater trajectories (Mullen, 2018).

Excluding some specific swimming motions in which the swimmer moves at relative low velocity and at streamlined position with the flow (e.g., gliding), in most aquatic movements, the swimmer's body segments are constantly changing their speed and direction. When these changes take place at the air-water interface or underwater, the surrounding water molecules are accelerated, generating a flow phenomenon in which rotating masses of water, known as vortices, are created (Andersen and Sanders, 2018; Sanders et al., 2017). Figure 6-1 illustrates this phenomenon during the underwater arm stroke. As vortices are shed from one side of the hand, the pressure difference between the dorsal and palm sides increases, producing a propulsive reaction force that goes from the high to low pressure side of the hand. Since the generated force has the same direction as the swimming motion, it helps propelling the body forward.

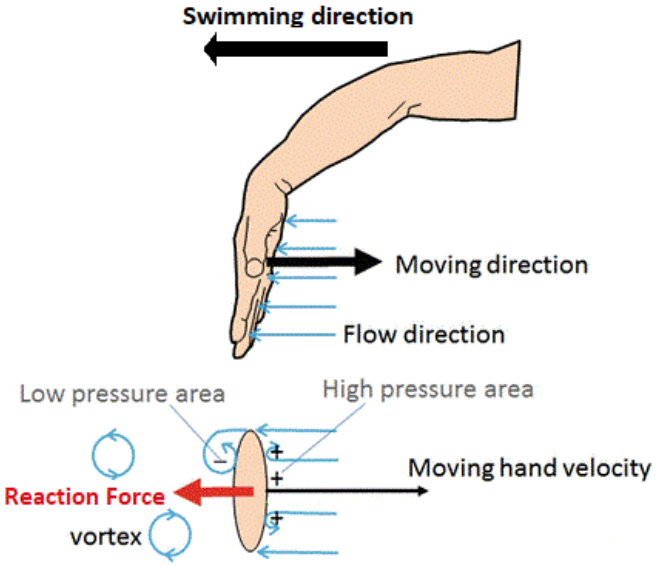

Figure 6-1: Illustration of the vortices generation during the underwater arm stroke (adapted from Sanders et al. (2017)).

The resistive, commonly known as drag, forces are responsible for slowing down the motion of a body moving through a fluid and are the main concern regarding swimming performance (Mullen, 2018). Drag forces are usually broken down into three different components: skin friction (or viscous) drag, pressure (or form) drag, and wave drag. Skin friction drag results from the interaction between the water's viscosity and the body's surface, decelerating the water particles in contact with the swimmer's skin. Pressure drag is related to the pressure differential between the leading and trailing edges of the body,

where high pressure develops at the front while low pressure exists at the bottom, meaning that particles tend to move from the front to the rear of the body, pushing it backward. The last and most significant form of resistive force is the wave drag. The combining effect of the reflected waves from the pool walls that collide with the swimmer, and the high agitation of water due to body motion, has a negative impact on swimming efficiency (Mullen, 2018). The drag forces are obtained from Equation (*6-1*), in which C_D includes all drag force components described.

Buoyancy is a fluid force that acts over a floating body, pushing it upwards. The factors that contribute to the magnitude of the buoyant force are explained by Archimedes' principle, which states that the magnitude of the buoyant force acting on a given body is equal to the weight of the fluid displaced by the body (Hall, 2012). Consequently, it depends on the density of the fluid in which the body is submerged.

A body's inertial mass is a measure of its resistance to changes in velocity, i.e., to being accelerated. Newton's second law of motion states that there is an inverse relationship between mass and acceleration. Under unsteady flow conditions, the inertial force is the sum of the swimmer's body mass times its acceleration plus the effects of the portions of water that are dragged during the accelerated body segment movements, known as the added mass of water. The unsteady-state inertial forces are computed by the following expression:

$$F_m = C_m \rho V \dot{U} = (1 + C_a) \rho V \dot{U} \tag{6-2}$$

where C_m is the inertial coefficient, C_a is the added mass coefficient, V is the body volume, and $\dot{U}$ is the time derivative of the body velocity. Analogously to drag and lift coefficients, C_m and C_a are dimensionless parameters that depend on body geometry and flow characteristics.

Understanding the propulsive and resistive characteristics of swimming is of main concern for sports analysts, coaches, and swimmers. Swimming performance is improved by maximising the propulsion, minimising the resistive drag forces, and optimising the swimming efficiency (Cohen et al., 2010; Honda et al., 2012). However, due to the non-stationary condition of the flow field in most swimming motions, it becomes extremely difficult to quantitatively describe the impact of these characteristics and how they interplay. To overcome this issue, simulation analysis tools well suited to consider the complex and dynamically changing effects of flow fields and body motions are used.

6.1.1. Challenges in Simulating Front Crawl Swimming

Front crawl swimming is not only the most complex stroke, but also the most commonly performed, both in training as well as in competition (Cohen et al., 2015; Sanders and Psycharakis, 2009; Takagi et al., 2015). The modelling challenges lie in the treatment of (1) the dynamically changing shape, with rotations of many body segments about multiple axes; (2) the out of phase motion characteristics between right and left sides of the human body; (3) the body roll asymmetries due to breathing (Psycharakis and Sanders, 2008); and (4) the air-water interface.

Current technologies are used to solve the complex non-linear equations of unsteady flow fields. The two most common numerical simulation techniques used in CFD are methods with structured meshes, such as the Finite Element Method (FEM) or Finite Differences (FD), and meshless methods, such as SPH. Both types of methods are based on fundamental fluid mechanics principles. However, FEM and FD consist of a grid-based continuum method, while SPH modelling involves a meshless particle-based approach (Cleary et al., 2013; Cohen et al., 2015). The required modelling components to perform the simulations are the swimmer's body geometry, which can be obtained from 3D laser scanning, and a computational model of the fluid, which accounts of the fluid flow regime and respective dynamic properties. Also, CFD mesh methods are established to handle large body deformations (Lauer et al., 2016), while in SPH modelling the surface representing the human body is attached to an underlying skeletal structure using commercial software (Cohen et al., 2015). The SPH is better suited to deal with the splashing free surface fluid flow as well as the added mass effects inherent to front crawl swimming due to the higher quality free surface representation (Cohen et al., 2015). Despite the arising contributions of CFD and SPH, there are still some barriers to their use. Each simulation requires too much computational time and increased computational solver capabilities (Cohen et al., 2015). Besides, a variety of input data that is not always available are required to define the body geometry.

Nakashima et al. (2007) developed an alternative computer simulation method that requires much less computation time than the commercial software programs based on FEM, FD, and SPH approaches. The analytical simulation model Swumsuit defines a simplified geometry of the swimmer's body and computes the hydrodynamic forces acting on each body segment while considering the unsteady fluid effects. This is actually a very important condition since in human swimming the unsteady effects are often more important due to the relatively high accelerations of the body segments throughout the stroke cycle when compared to relatively low velocities (Honda et al., 2012). Experimental investigations were performed by Nakashima et al. (2007) to obtain the force coefficients of the governing equations for a rotating limb motion, and a simulation for the gliding position.

6.2. Simulation Software: Swumsuit

Swumsuit is a software in which the swimming human simulation model SWUM, proposed by Nakashima et al. (2007), is implemented. The model topology and body parts' geometry are imposed, consisting of a series of truncated elliptic cones. The analysis tool allows the computation of the fluid forces acting on each segment of the whole body, including the unsteady fluid effects. The unsteady fluid forces are computed without solving the flow field (Nakashima et al., 2007; Nakashima, 2005). Instead, they are determined from the local kinematics of each part of the human body at each instant of time, and from force coefficients estimated experimentally. The simulation results has been reported to be associated with a 7.5% error compared with experimental results obtained for a standard six-beat front crawl swimming, based on the swimming speed (Nakashima et al., 2007). According to the authors, the main reason for the discrepancies stems from the modelling errors of the fluid forces and the joint motions, especially at the start or end of a stroke cycle and when close to the water surface (Nakashima et al., 2007; Takagi et al., 2015).

Due to its ability to provide the fluid forces developed over the full body while considering the contribution of the unsteady effects, Swumsuit is the method used in this dissertation to obtain the hydrodynamic forces of the front crawl swimming performed in LABIOMEP-UP.

6.2.1. Swimming Human Model (SWUM)

The human body model developed by Nakashima et al. (2007), denoted as SWUM, is divided into twenty-one body segments, as illustrated in Figure 6-2.

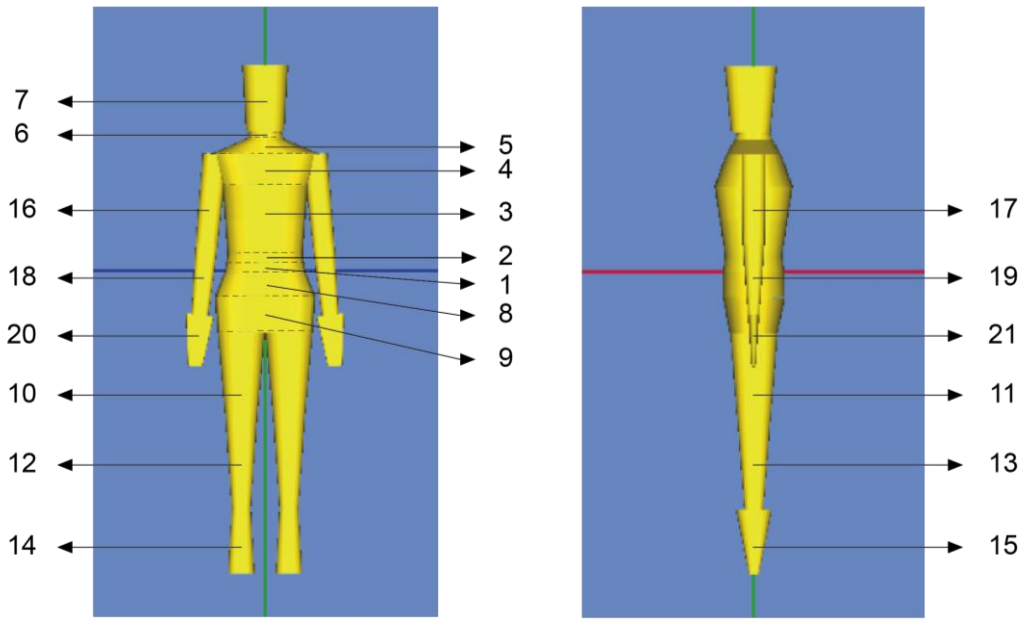

Figure 6-2: SWUM model topology: 1 – lower waist, 2 – upper waist, 3 – lower breast, 4 – upper breast, 5 – shoulder, 6 – neck, 7 – head, 8 – upper hip, 9 – lower hip, 10 – right thigh, 11 – left thigh, 12 – right shank, 13 – left shank, 14 – right foot, 15 – left foot, 16 – right upper arm, 17 – left upper arm, 18 – right forearm, 19 – left forearm, 20 – right hand, and 21 – left hand.

Each body in SWUM is represented as a truncated elliptic cone. Accordingly, for each body segment, additional geometric and anthropometric data are necessary to define the bottom and top distances of the major and minor axes of the ellipses, the body length, and body density. Nakashima et al. (2007) provided a complete dataset with all these quantities measured for a Japanese male, at the age of 20-29, with 1.705 m, and 64.9 kg. All lengths were normalised by the subject's stature, and the segments' density were obtained relative to the water. Consequently, the normalised lengths represent geometric scaling parameters of each segment of the human body model.

To obtain the corresponding data for another specific swimmer subject, in particular for that under analysis in this work (swimmer male subject at the age of 25 years old, with 1.80 m and 70.3 kg), the normalised lengths provided in the dataset of Nakashima et al. (2007) are used in the current study. By doing so, it is assumed that both subjects belong to the same percentile (Dumas et al., 2007a). Furthermore, at this point, the model topology is not consistent between SWUM and LHBM, as 21 versus 16 body segments are used to represent the full body, respectively. To be able to consider the data provided by Swumsuit in the biomechanical model developed, a relationship between the body

segments of SWUM and LHBM is defined. Table 6-1 details the association between SWUM and LHBM body topologies. Regarding the specific body density, the percentage of mass of each body segment is estimated from the literature (Dempster and Gaughran, 1967; Winter, 2009). The complete dataset computed for the current study can be consulted in Table C-2 of Appendix C.

Table 6-1: Correspondence between body models. The ID of the twenty-one rigid bodies in SWUM is consistent with Figure 6-2. The percentage of body mass is relative to the respective body in LHBM, except bodies with the superscript [3]. The body lengths in SWUM are normalised by the swimmer's stature.

LHBM		SWUM			
ID	Rigid Body	ID	Body Name	Body mass [%]	Scaling factor for body length
1	Pelvis	1	Lower_waist	35.45[1]	0.035308
		8	Upper_hip	64.55[1]	0.054417
		9	Lower_hip	(30+30)[2]	0.074896
2	Right Thigh	10	Right_thigh	70	0.187566
3	Right Leg	12	Right_shank	100	0.180938
4	Right Foot	14	Right_foot	100	0.137193
5	Left Thigh	11	Left_thigh	70	0.187566
6	Left Leg	13	Left_shank	100	0.180938
7	Left Foot	15	Left_foot	100	0.137193
8	Torso	2	Upper_waist	17[3]	0.071847
		3	Lower_breast	5.49[3]	0.071847
		4	Upper_breast	5.49[3]	0.065689
		5	Shoulder	5.27[3]	0.031202
9	Right Arm	16	Right_upper_arm	100	0.186628
10	Right Forearm	18	Right_forearm	100	0.15132
11	Right Hand	20	Right_hand	100	0.107331
12	Left Arm	17	Left_upper_arm	100	0.186628
13	Left Forearm	19	Left_forearm	100	0.15132
14	Left Hand	21	Left_hand	100	0.107331
15	Neck	6	Neck	100	0.016422
16	Head	7	Head	100	0.139062

[1]From (Winter, 2009); [2]30% of the Right Thigh and 30% of the Left Thigh (LHBM); [3]Percentage of body mass relatively to total body weight (Dempster and Gaughran, 1967).

6.2.2. Swumsuit Coordinate Systems

The simulation model considers three different coordinate systems: (1) the absolute coordinate system, $O - xyz$; (2) the body coordinate system, $O_b - x_b y_b z_b$; and (3) the camera coordinate system, $O_c - x_c y_c z_c$.

The mechanical simulation is conducted in the absolute coordinate system. In this reference frame, the swimming direction depends on the initial direction of the swimmer, which is defined in the analysis settings input data file. The z axis points vertically upwards, and the x and y direction axes define the plane of the water surface. The origin of the absolute coordinate system is located at the water surface, at $z = 0$.

The motion of the joints in SWUM are represented as rotations of body segments about their respective body coordinate system, located at the proximal joint of each body. In this reference frame, the direction axes are given as: x_b points from the posterior to anterior direction; y_b points from the right to the left side of the body; and z_b runs from inferior to superior direction. These directions are valid for all bodies in SWUM.

The camera coordinate system is a non-stationary reference frame that moves at constant velocity with the swimmer. The output data file that contains all data regarding the animation of the swimming motion in Swumsuit is described in this reference frame. However, the orientation of the camera coordinate system ($O_c - x_c y_c z_c$) is not known.

Understanding the difference between the three coordinate systems used by Swumsuit is crucial to address the correct correspondence between modelling specifications and swimmer's motion, and to be able to integrate them in both the simulation model and the MATLAB program code. Figure 6-3 provides a schematic representation of the simulation coordinate systems. Note that the representation of $O_c - x_c y_c z_c$ is only illustrative since its orientation is not provided by Nakashima et al. (2007).

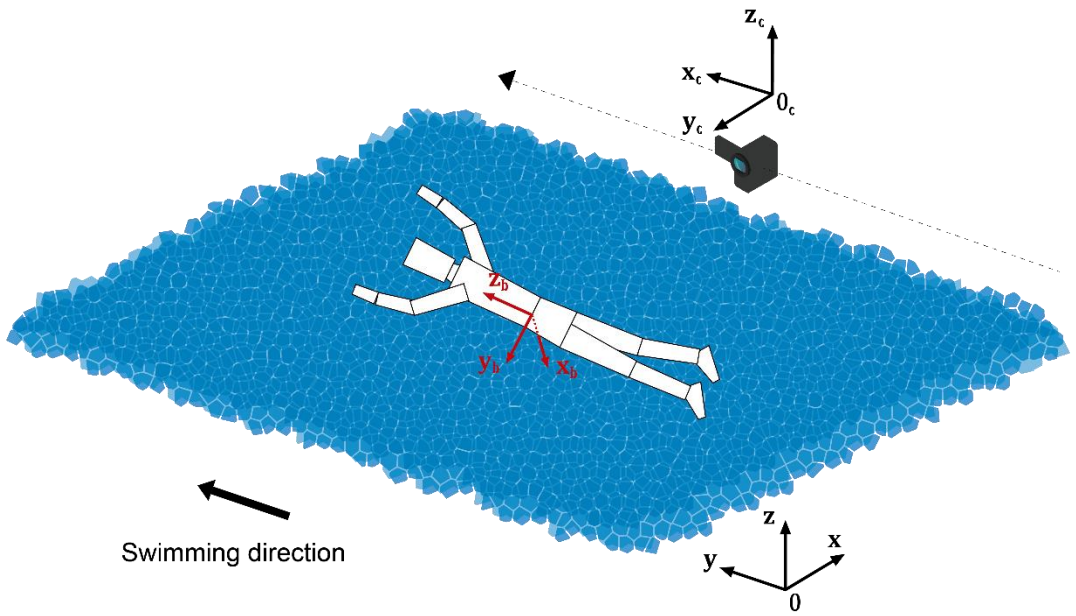

Figure 6-3: Representation of SWUM coordinate systems: absolute coordinate system ($O - xyz$), body coordinate system ($O_b - x_b y_b z_b$), and camera coordinate system ($O_c - x_c y_c z_c$). The global coordinate system in which the LHBM is defined is parallel to $O - xyz$. In this figure, one single body coordinate system is represented in red, although in SWUM each body has its own reference frame fixated at the proximal joint. The representation of $O_c - x_c y_c z_c$ is only illustrative since its orientation is not known.

6.2.3. Swumsuit Outline

The simulation software Swumsuit consists of a main program developed in Fortran that performs the analysis engine part, and a Graphical User Interface (GUI) organised as follows (Nakashima, 2005):

- A "Project folder" tab, to locate the working directory.
- An "Input" tab, to give and edit the body geometry and joint motion input data.

- An “Analysis” tab, to set and edit the simulation analysis conditions and run the simulation.
- And an “Output” tab, which allows the visualisation of the three-dimensional swimming human motion animation and the computed output data (fluid forces, swimming speed, etc).

Swumsuit is designed to solve the 6 DOF absolute motion of the swimmer’s body as one single body, given the human body geometry and relative body motion. As simulation input, the analysis engine part reads three files, each containing data of body geometry, joint motion, and analysis settings. For studies in which the body motion is obtained by a motion capture system and the only objective concerns the determination of the fluid forces acting on the swimmer’s body, Swumsuit can be set to read the absolute movement, without solving the equations of motion. In such case, six additional files are given as input regarding the linear and angular velocities of the COM of the whole body during the stroke cycle, and the whole-body COM and principal axes of inertia are respectively fixed to the lower tip of the lower waist body segment and to the body coordinate system ($O_b - x_b y_b z_b$). Since the absolute motion kinematics of the front crawl swimming performed in LABIOMEP-UP is already determined and only the computation of the fluid forces is of interest in this study, Swumsuit is used without solving the equations of motion.

According to the software requirements, the first part of the analysis consists in the definition of the input data files: (1) data of body geometry and density, `body_geometry.dat`; (2) relative body motion as rotation angles, `joint_motion.dat`; (3) analysis parameters and initial condition, `analysis_settings.dat`; and (4) absolute body motion for the whole swimmer’s body – linear velocities defined in the three directions of the absolute coordinate system, `input_vgx/vgy/vgz.dat`, plus three angular velocities defined in the body coordinate system, `input_ome1/ome2/ome3.dat`.

The body geometry data file is written for the subject under analysis following the SWUM topology. The specifications of the human body model are described in Section 6.2.1. The relative body motion in SWUM is represented through rotations of body segments about their own body coordinate system ($O_b - x_b y_b z_b$), each fixed at the proximal extremity of the respective body segment. The configuration of SWUM for which all rotations are null is with the upper limbs raised upward, the trunk and lower limbs straight, and the feet pointing downward. The resulting joint motion depends on the order of the rotations of the body segments that are provided to Swumsuit in the `joint_motion.dat` file about the x_b, y_b, and z_b direction axes (Nakashima et al., 2007). Moreover, in SWUM, the rotation of a body segment about a given axis does not affect the subsequent body segment(s), so the same rotation should be given to the consecutive body segment(s) as well to ensure the overall coordinated body motion. The analysis settings necessary to conduct the simulation are defined in a data file that includes the stroke cycle time, the number of total steps per stroke cycle, the number of cycles to perform, the coordinates of the whole-body COM at the first time step ($t = 0$) in the absolute coordinate system ($O - xyz$), the direction of the whole-body principal axes of inertia about $O_b - x_b y_b z_b$, and the linear and angular velocities of the whole-body COM at $t = 0$. Besides these parameters, the settings data file also contains a list of the fluid force coefficients used in the simulation for each body segment. If the motion kinematics

are known *a priori*, additional input data files including the linear and angular velocities of the whole-body COM about the absolute and body coordinate systems, respectively, for all time steps are required.

The simulation is conducted for the number of cycles defined. Since the front crawl stroke is a cyclic motion, the input files require data for only one single stroke cycle. The format of the nine input data files is described in the software manual and can be consulted in Appendix C of the present document (format of body geometry, joint motion, analysis settings, and linear and angular velocities data files are given, respectively, in Table C-1, Table C-3, Table C-4, and Table C-5).

The analysis engine consists in the solution of the analytical model of Swumsuit given the input files. The fluid forces acting on each body segment throughout the swimming stroke are given as output data files. The software fluid force model is depicted in Figure 6-4.

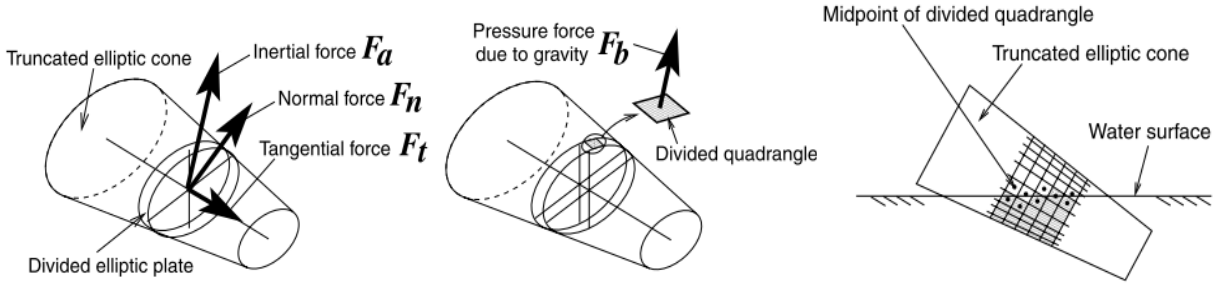

Figure 6-4: Analytical modelling of the fluid forces in Swumsuit (adapted from Nakashima et al. (2007)): (a) Fluid force components acting on a thin elliptic plate's centre (except buoyancy), (b) buoyancy is calculated by integrating the pressure force on divided quadrangles, and (c) decision on whether quadrangles are above or below the water surface.

The unsteady fluid force components acting on each truncated elliptic cone result from inertial force due to added mass of fluid (F_a), normal (F_n) and tangential (F_t) drag forces, and buoyancy (F_b), which includes the gravitational forces. Each truncated elliptic cone is divided into thin elliptic plates along the longitudinal axis, as shown in Figure 6-4(a), and all fluid force components except buoyancy are assumed to act on each centre of the thin elliptic plates (Nakashima et al., 2007).

The drag force tangential to the longitudinal axis of the cone F_t represents the resistive fluid effects, while the drag force normal to the axis F_n corresponds to the drag and lift force generated by limb motion (Nakashima, 2006). These two components plus the inertial force due to added mass F_a are computed from the local kinematics of each body segment, at each time step. From Equations (*6-1*) and (*6-2*), F_n and F_t are proportional to the local velocity at the thin plate's centre in the normal and tangential directions, respectively, whereas F_a is assumed to be proportional to the local acceleration in the normal directions. Furthermore, these fluid force components are computed using their coefficients, C_n, C_t, and C_a, respectively.

Nakashima et al. (2007) conducted an experimental investigation to identify the coefficients of the normal drag C_n, and added mass C_a. The experimental setup consisted in the measurement of the rotating angles and bending moment at the root of an artificial limb motion in water. From the 24 trials

performed, the experimental coefficients were identified as $C_a = 0.472 \sim 0.831$ and $C_n = 0.994 \sim 1.192$, and by averaging for all trials they were finally determined as $C_a = 0.651$ and $C_n = 1.077$, within 10% error (Nakashima et al., 2007). These two values are considered for all body segments of SWUM, as the authors considered this assumption not to cause significant error since the inertial force due to added mass and the drag force in the normal direction are thought to be relatively small for the trunk, including head and neck. Regarding the tangential drag coefficient C_t, it was estimated by performing a simulation in which the human body took the gliding position. From the simulation C_t was determined to be 0.036 (Nakashima et al., 2007).

Buoyancy, on the other hand, is calculated by integrating the pressure force due to gravity acting on a quadrangle, into which the side surface of the thin elliptic plate is divided in the circumferential direction, as seen in Figure 6-4(b). This force is computed only for the submerged quadrangles, as shown in Figure 6-4(c) (Nakashima, 2006; Nakashima et al., 2007).

By numerically integrating all the above-mentioned fluid forces computed for each thin plate in the longitudinal direction, the fluid force acting on each truncated elliptic cone is obtained.

Once the simulation is finished, an “Output_data” folder is created in the workspace directory containing all computed data. The external forces are given in two different types of files: (1) a `motion.dat` file with the distributed fluid forces acting at the centre of each thin plate of each body, for all time steps of the stroke cycle; and (2) 63 force files (21 body segments × 3 components), each containing, for all time steps, five columns of force data – total force, added mass, normal drag, tangential drag, and buoyancy. In both cases, the data files give the direction and the nondimensional magnitude of the fluid forces in each component of the 3D space. The data in the 63 force files are defined in the absolute coordinate system ($O - xyz$), while the forces in the `motion.dat` file are in the camera coordinate system ($O_c - x_c y_c z_c$). Since the fluid forces in `motion.dat` represent only those acting at the centre of each thin plate, buoyancy is not accounted for in this file.

6.2.4. Interface between Swumsuit and LHBM

Data output from the Swumsuit must be processed to be consistent with the biomechanical model developed and its formulation. This section addresses the procedure implemented to convert modelling specifications and motion data from LHBM to SWUM, and vice versa. The overall data flow is illustrated in Figure 6-5.

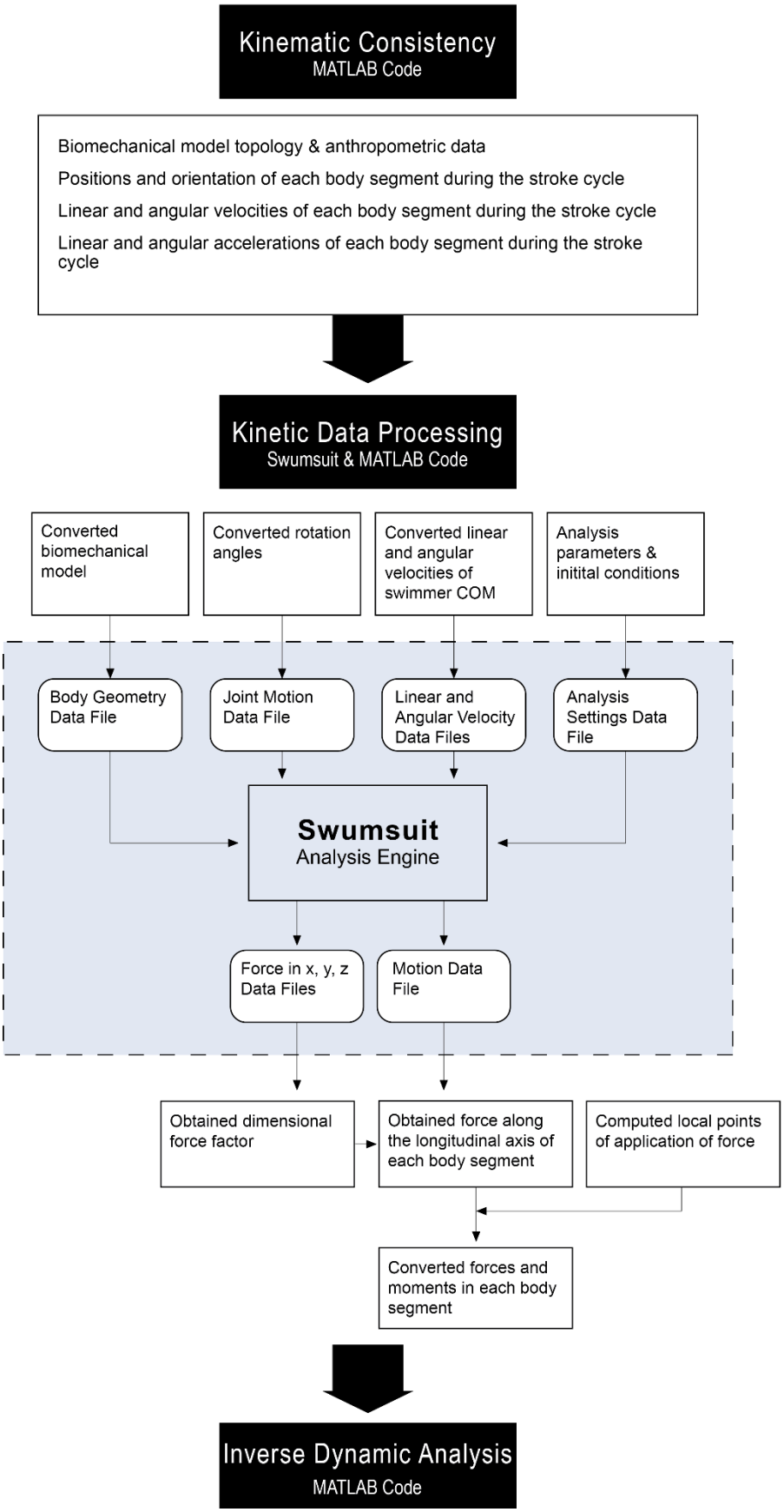

Figure 6-5: Data flow of the interface between the simulation software Swumsuit and the LHBM. The blue shaded rectangle represents the simulation analysis that is performed in Swumsuit.

As described in Section 6.2.1, the first obstacle in the application of Swumsuit is the different discretisation of its human body model. Twenty-one body segments compose the human body model in SWUM, the geometry and density of which must be defined for all. In this work, the geometric dataset of Nakashima et al. (2007), which is scaled by swimmer's stature is used considering the height and weight of the subject under analysis here. The density of the body segments relative to the water is computed considering the percentage of body mass addressed to each body described in Table 6-1.

The kinematic analysis performed for the front crawl swimming stroke measured in LABIOMEP-UP outputs the consistent positions, velocities, and accelerations of the LHBM. As explained in Chapter 4, the vector of consistent positions $\mathbf{q}$ defines the coordinates of the COM and orientation of each body segment for all time steps. The orientation is defined by Euler parameters, which describe the direction axes of the body-fixed reference frame (ξ, η, ζ) of each body. Since body motion in SWUM is given as rotations of body segments about their own body coordinate systems $(O_b - x_b y_b z_b)$, the orientations obtained in the kinematic analysis are converted to represent rotations of body segments:

(i) First, the four Euler parameters are converted to rotation angles about the ξ, η, and ζ axes. The body-fixed reference frames in LHBM follow the recommendations of the ISB (Wu et al., 2002, 2005). Consequently, the local reference frames are not the same for the right and left sides of the human body, as they are defined based on anatomical landmarks.

(ii) To transform coordinates from (ξ, η, ζ) to (x_b, y_b, z_b), a rotation matrix $\mathbf{R}_{body}$ is considered such that:

$$\begin{bmatrix} x_b \\ y_b \\ z_b \end{bmatrix} = \mathbf{R}_{body} \begin{bmatrix} \xi \\ \eta \\ \zeta \end{bmatrix} \tag{6-3}$$

For the pelvis, torso, head, neck, and right thigh, leg, foot, arm, forearm, and hand, the rotation matrix is given by:

$$\mathbf{R}_{body} = \begin{bmatrix} 1 & 0 & 0 \\ 0 & 0 & -1 \\ 0 & 1 & 0 \end{bmatrix}, \tag{6-4}$$

while for the left thigh, leg, foot, arm, forearm, and hand, it is given by:

$$\mathbf{R}_{body} = \begin{bmatrix} -1 & 0 & 0 \\ 0 & 0 & 1 \\ 0 & 1 & 0 \end{bmatrix} \tag{6-5}$$

The definition of the body coordinate system direction axes is described in Section 6.2.2.

(iii) Considering that the body model configuration in which the rotations of body segments are null in SWUM differs from that in LHBM (see Section 6.2.3), during the conversion, the rotation angles about the y_b axis of the right and left feet are subtracted by 90º, while for the right and left arms, forearms, and hands, 180º are added and subtracted to the rotation angles about the y_b and z_b axes, respectively.

Regarding the swimmer's absolute body motion given in the `input_vgx/vgy/vgz.dat` and `input_ome1/ome2/ome3.dat` input files, Swumsuit defines the whole-body COM fixed to the lower tip of the lower waist body segment, which corresponds to the pelvis in LHBM (Table 6-1), and the principal axes of inertia are settled to the body coordinate system ($O_b - x_b, y_b, z_b$), thus corresponding to the rotation matrix in Equation *(6-4*). Accordingly, the linear and angular velocities of the pelvis are taken from the vector of consistent velocities $\dot{\mathbf{q}}$ for all time steps. Note that $\dot{\mathbf{q}}$ has, for each body segment, 6 entries – three linear velocities defined in the global reference frame, and three angular velocities defined in the body-fixed reference frame. As mentioned before, the linear velocities in Swumsuit are defined in the absolute coordinate system, while the angular velocities are defined in the body coordinate system. Since the global reference frame ($O - XYZ$), in which LHBM is defined, and the absolute coordinate system ($O - xyz$), in which the simulation model is conducted, are parallel to each other (Figure 6-3), the linear velocities in $\dot{\mathbf{q}}$ can be directly applied in SWUM. Regarding the angular velocities, the rotation matrix in Equation *(6-4*) must be considered to transform the angular velocities from the pelvis body-fixed reference frame to $O_b - x_b, y_b, z_b$.

The analysis parameters in Table 6-2 are given as input to the simulation. Besides the definition of the stroke cycle time and total time steps, which come from the kinematic analysis, the direction of the whole-body principal axes of inertia about ($O_b - x_b, y_b, z_b$), the position, and the linear and angular velocities of the swimmer's body COM at $t = 0$ are also given in the input data file. Regarding the fluid force model specifications, the number of longitudinal and circumferential divisions of each truncated elliptic cone and the force coefficients used to compute the fluid forces are provided. In this work, the modelling parameters are the same as those defined by Nakashima et al. (2007) since both studies are performed for a six-beat front crawl swimming motion and the shape and geometry of both swimmers' body segments are similar.

Table 6-2: Specifications of the simulation analysis.

Stroke cycle	2.39 s
Time steps	240
Number of divisions of each truncated elliptic cone	
- For longitudinal direction	10
- For circumferential direction	36
Added mass coefficient, C_a	0.651
Normal drag coefficient, C_n	1.077
Tangential drag coefficient, C_t	0.036

All the input data are written into the respective files, following the specifications detailed in Appendix C. The MATLAB function *system* is called to execute the operating command of Swumsuit. Once the simulation is finished, the force files are read, and data are converted from SWUM to LHBM.

In LHBM, the vector of external forces $\mathbf{g}$ in Equation *(4-25*) has 6 entries: the global forces in the X, Y, and Z components, and the local moments defined in the body-fixed reference frame of the respective body. As mentioned in Section 6.2.3, the data in the 63 force files are described in the absolute

coordinate system ($O - xyz$). The dimensional force coefficient is given in the header part of each file, and the force components are described in different columns, corresponding to total force, added mass, normal drag, tangential drag, and buoyancy. Since the absolute coordinate system and the global reference frame are parallel, the "total forces" columns provide the forces in the global X, Y, and Z components of each body in SWUM, and the conversion to the LHBM is depicted in Table 6-1. However, these files do not provide enough information for the computation of the local moments as the total forces are given in the COM of each body and thus the points of application of the corresponding distributed forces are not provided.

On the other hand, the `motion.dat` file contains the distributed forces and respective points of application acting upon the longitudinal axis of each body, except buoyancy. The force data are defined in the camera coordinate system ($O_c - x_c y_c z_c$) and are scaled for the animation. Since the animation scaling coefficient is not known, a relationship between the 63 force files and `motion.dat` file is established to: obtain the dimensional local forces; convert the local forces from the camera to the absolute coordinate system; and add the contribution of buoyancy into the vector of local forces.

The methodology implemented computationally is explained in the following:

(i) The force data in the 63 force files is multiplied by the dimensional coefficient provided in the header part of the respective file, thus obtaining the fluid forces in Newton.

(ii) For each body segment, the added mass, normal drag, and tangential drag fluid forces are added in the three directions (x, y, and z). This force is hereafter denoted as $(\mathbf{f}_i)_{xyz}$, where i is the body segment in SWUM, and the subscript *"xyz"* points that the force is described in the absolute coordinate system. In this calculation the buoyancy force is not considered since the magnitude of $(\mathbf{f}_i)_{xyz}$ is to be used to identify the coefficient that converts the fluid forces in `motion.dat` file, which disregard buoyancy, into Newtons.

(iii) Similarly, the non-dimensional distributed forces acting upon the longitudinal axis of body i, $\left(\mathbf{f}_{k,i}\right)_{x_c y_c z_c}$, where k is the number of longitudinal divisions given in Table 6-2, are given in the `motion.dat` file in the x_c, y_c, and z_c components. Note that the dimensional force coefficient is not known for these forces.

(iv) In order to obtain the dimensional force magnitudes of $\left(\mathbf{f}_{k,i}\right)_{x_c y_c z_c}$, the 10 distributed forces acting along the longitudinal axis of each body segment, at each time step, are summed for the x_c, y_c, and z_c components, and the resulting non-dimensional magnitude is computed:

$$(\mathbf{f}_i)_{x_c y_c z_c} = \sum_{k=1}^{10} \left(\mathbf{f}_{k,i}\right)_{x_c y_c z_c} \Rightarrow \left\|(\mathbf{f}_i)_{x_c y_c z_c}\right\| \tag{6-6}$$

where $(\mathbf{f}_i)_{x_c y_c z_c}$ is the vector of non-dimensional fluid forces acting on body i in SWUM, $\left(\mathbf{f}_{k,i}\right)_{x_c y_c z_c}$ is the vector of non-dimensional distributed fluid forces acting in the centre of each thin plate along the longitudinal axis of that same body i, and k is the number of

longitudinal divisions. The subscript "$x_c y_c z_c$" points that these forces are described in the camera coordinate system.

(v) The force magnitudes are compared by computing the ratio r_f between $\|(\mathbf{f}_i)_{xyz}\|$ and $\|(\mathbf{f}_i)_{x_c y_c z_c}\|$.

(vi) The dimensional distributed forces are obtained by multiplying the computed ratio r_f with the corresponding non-dimensional force vector in (iii). At this point, the dimensional distributed forces $(\mathbf{f}_{k,i})_{x_c y_c z_c}$ are still defined in the camera coordinate system and do not consider the buoyancy force component.

(vii) Because the relationship between the camera and the absolute coordinate systems is unknown, the rotation matrix relating these is computed through the solution of the following system of equations:

$$(\mathbf{f}_i)_{xyz} = (\mathbf{A}_i)_{x_c y_c z_c} (\mathbf{f}_i)_{x_c y_c z_c} \tag{6-7}$$

where $(\mathbf{A}_i)_{x_c y_c z_c}$ is the rotation matrix from the camera to the absolute coordinate system.

(viii) Using the rotation matrix $(\mathbf{A}_i)_{x_c y_c z_c}$ computed through Equation *(6-7)*, the distributed forces $(\mathbf{f}_{k,i})_{xyz}$ in the absolute coordinate system are computed from $(\mathbf{f}_{k,i})_{x_c y_c z_c}$.

(ix) From the dimensional forces in step (i), the total force vector $(\mathbf{f}_i)_{xyz}^{TOTAL}$ is defined containing all fluid force components, including buoyancy. To determine the contribution of the buoyancy forces missing in the `motion.dat` file, the sum of $(\mathbf{f}_{k,i})_{xyz}$ along the 10 thin plates of body i is subtracted to $(\mathbf{f}_i)_{xyz}^{TOTAL}$. The difference represents how much of buoyancy must be added to the distributed forces vector $(\mathbf{f}_{k,i})_{xyz}$.

(x) Since all bodies are divided into 10 thin plates along the longitudinal axis, the buoyancy forces, computed in step (ix), are assumed equally distributed over all plates.

(xi) Finally, the total distributed forces in the absolute coordinate system $(\mathbf{f}_{k,i})_{xyz}^{TOTAL}$ are obtained from $(\mathbf{f}_{k,i})_{xyz}$ updated with the buoyancy components in (x). The conversion from the absolute coordinate system in SWUM to the global reference frame in LHBM is direct, and the correspondence between body segments is established in Table 6-1.

At this point, the global distributed hydrodynamic forces acting upon the longitudinal axis of the body segments are determined and converted to the LHBM. The force application points of these forces are determined as equally spaced points along the longitudinal axis of each body segment, i.e., the line that connects the proximal and the distal end points of the respective body. Each force applied in its application point produces a moment in relation to the body segment COM. Finally, the total local moment of each body is the sum of the contribution of the 10 thin plates, expressed in the body-fixed reference frame.

Note that the conversion depicted in Table 6-1 is performed twice: first, to transform the biomechanical and kinematic data from LHBM to SWUM and give them as input to the simulation analysis; once the

simulation in Swumsuit is concluded, the hydrodynamic forces are applied to the correspondent bodies in LHBM to perform the inverse dynamic analysis.

6.3. Results and Discussion

The results of the simulation performed in Swumsuit of the six-beat front crawl swimming motion are presented in Figure 6-6 for six events of the stroke cycle. These events are identified by the corresponding percentage of the total stroke cycle time. The red arrows represent the direction and magnitude of the fluid forces acting on the swimmer's body segments, except buoyancy. The distributed characteristics of the forces reflect the force in each one of the elliptic thin plates used for their evaluation. The total simulation computing time was approximately 1 minute and 38 seconds on an Intel Core i5-7200U CPU with 8GB RAM, with the analysis settings depicted in Table 6-2.

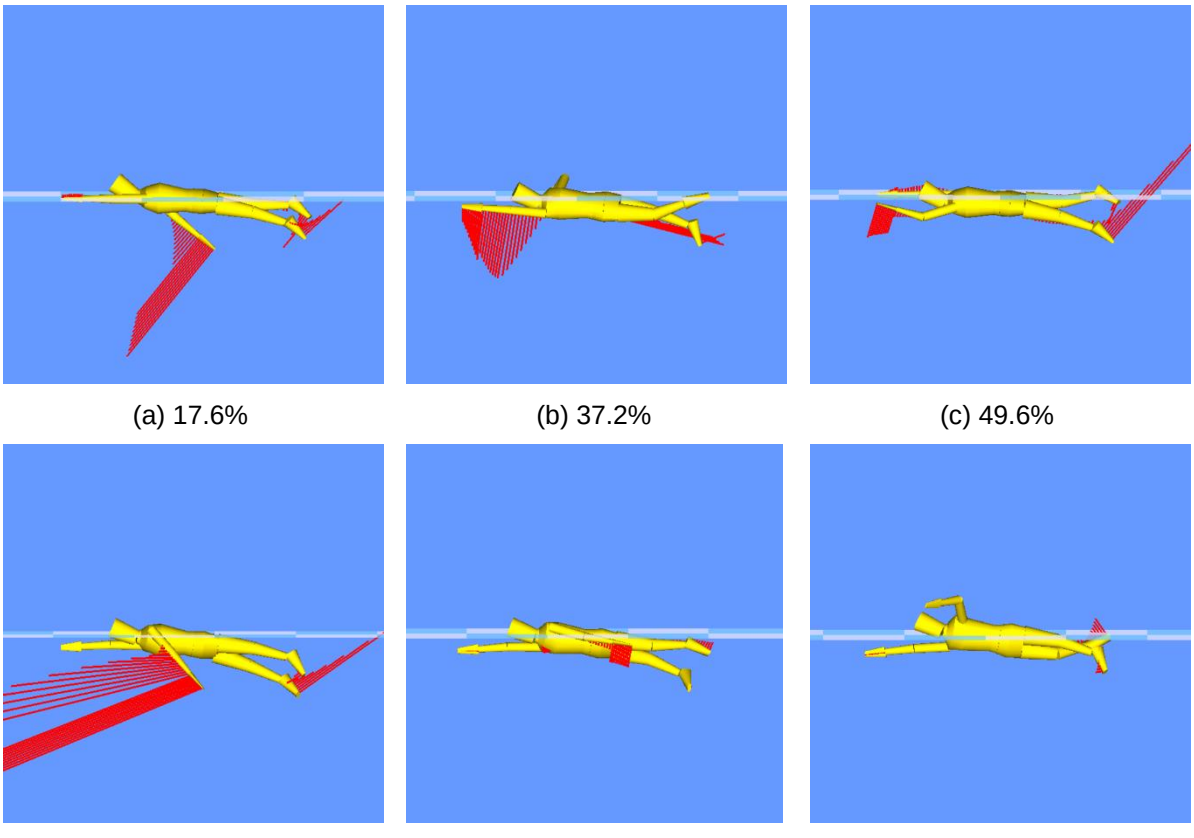

(a) 17.6% (b) 37.2% (c) 49.6%

(d) 63.2% (e) 71.2% (f) 90.4%

Figure 6-6: Simulation results of the left-hand six-beat front crawl swimming stroke in Swumsuit (lateral view). The six events are identified by the corresponding percentage of the total stroke cycle time.

The global X, Y, and Z fluid force components acting upon the right foot, leg, and thigh body segments of LHBM are shown in Figure 6-7. These results are compared to those obtained by Nakashima et al. (2007). Although the force profiles are similar among the bodies of the right lower limb, their magnitudes are generally higher in the current study than those reported in the simulation performed by Nakashima et al. (2007), especially in the three components of the foot body segment.

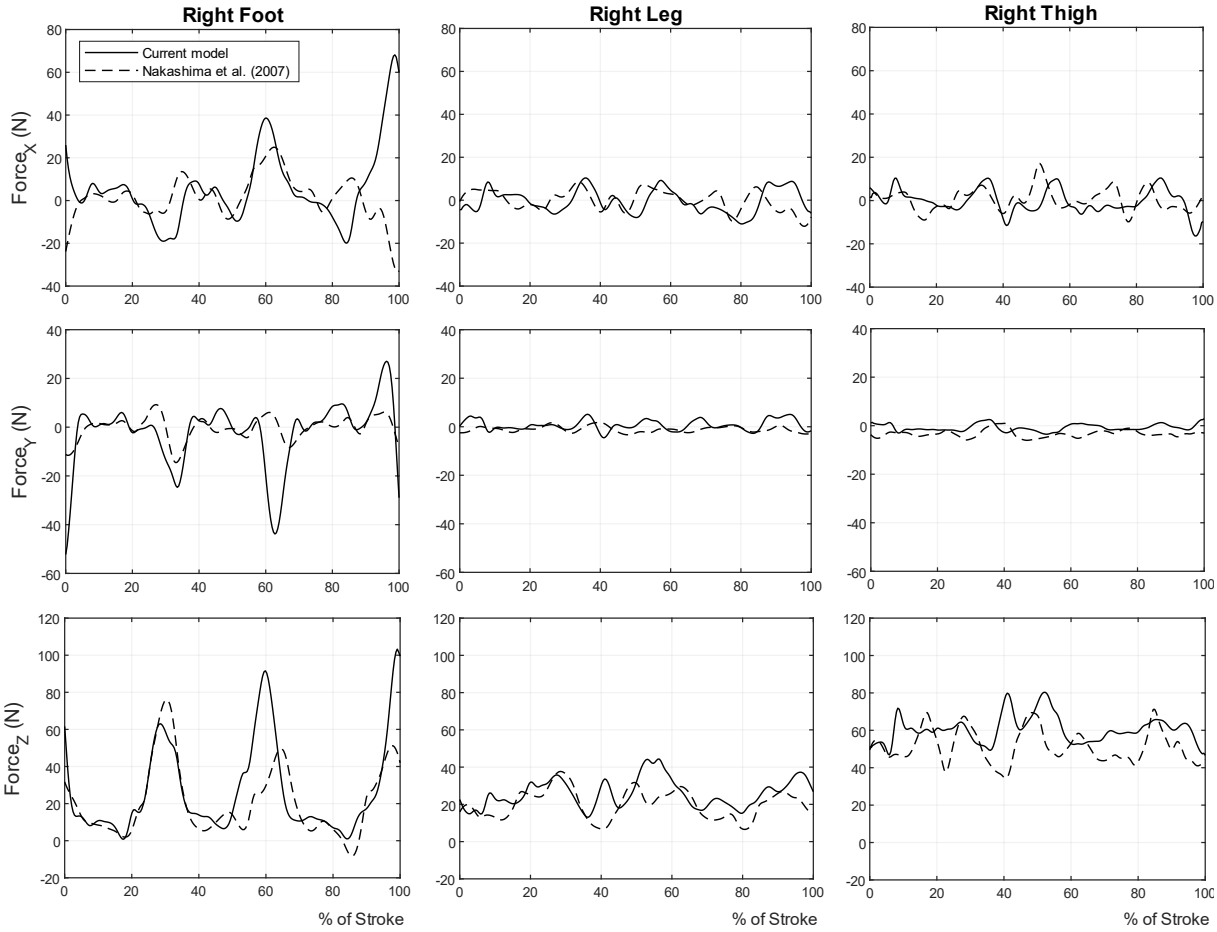

Figure 6-7: Simulation results of the hydrodynamic forces developed during a left-hand six-beat front crawl swimming stroke cycle. The global fluid forces obtained in the current study (solid line), and reported by Nakashima et al. (2007) (dashed line) are given in the X, Y, and Z components. The horizontal axis corresponds to a percentage of the stroke cycle.

Regarding the fluid forces acting on the right foot, three force peaks can be clearly identified in the vertical component, each acting approximately at 28%, 60%, and 99% of the stroke cycle, which is consistent with its motion towards the bottom of the swimming pool a few instants before, approximately at 20%, 51%, and 90%, which corresponds to frames (a), (c), and (f) in Figure 6-6. These instants of time are coincident in Figure 6-7 with the beginning of generation of propulsive force by the respective body, and the peak force is then reached a few instants later. The correlation of these peaks with the right ankle joint motion verifies the postulated assumptions in the literature that state that the maximum propulsive forces in the lower limbs occur during the downbeat, when the ankle in maximum plantarflexion (Keys, 2010; Sanders et al., 2017; Wei et al., 2014). On the other hand, the lateral and axial force components are of two types: resistive, or negative, forces, and propulsive, or positive.

Despite the similarity regarding the distribution of fluid forces throughout the stroke cycle, the force magnitudes obtained in the current work are larger, by more than 40 N, than those reported by Nakashima et al. (2007). As already mentioned, the propulsive forces in the leg kick motion are mostly generated during the downbeat. Keys (2010) studied the front crawl motion of an elite male swimmer and the hydrodynamic forces were obtained by performing a simulation analysis using a CFD commercial software. In his work, he observed that the greater flexibility on the left ankle joint resulted

in higher propulsion developed by the left foot. Analogously, the third and last downbeat of the right leg is initiated by the flexion of the right hip, at 85% of the stroke cycle. The downbeat results from the combined action of the hip flexion, followed by knee extension, and ankle plantarflexion. From Figure 5-8(a), the hip flexibility registered its maximum amplitude at that specific time, which may have contributed to the increased generation of force. Another hypothesis is related with the body roll. As shown in Figure 5-9(b), the hip roll amplitude performed by the swimmer in this work is greater than the usual interval reported in the literature. One of the objectives of a hip-driven technique is to use the hip rotation as a power source for propulsion. The transition of the swimmer's body rotation from the right to the left side occurs in the stroke cycle at approximately 53%. At that same time, the downbeat of the right leg is initiated, with the ankle joint flexing towards its maximum position, as seen in Figure 5-8(c). The combined rotation of the whole swimmer's body to the left side and the kicking action of the right leg could result in a higher peak of force, as seen in the Z component of the right foot. A third possible contribution to the high force magnitudes obtained may be related with the acceleration. In swimming motion analysis, the unsteady fluid forces are often more important due to the relatively high accelerations of the body segments. Swimmers are constantly changing the velocity and position of body segments to enhance swimming efficiency. As the pelvis linear and angular accelerations are given as input to the simulation analysis, it is possible that the acceleration of body segments is higher in this work than that obtained by Nakashima et al. (2007).

Regarding the axial and lateral force components in Figure 6-7, the forces developed at the right foot are significantly more relevant than those developed at the thigh and leg body segments. However, in the vertical component, the peak force of the right thigh and right leg in the LHBM are, respectively, 80.3 N and 44.3 N, against 71.2 N and 37.7 N in Nakashima et al. (2007). Although the maximum vertical force of 103.3 N remains in the right foot, the contribution of the remaining bodies is also important for thrust force generation. Keys (2010) obtained larger percentage of propulsion in the thighs than the feet, which reinforces the importance of entire leg movement and positioning rather than just focusing on feet propulsion.

The results shown in Figure 6-7 support the validity of the interface developed between Swumsuit and the LHBM, as the dynamic response developed at the lower limbs is similar between the results obtained here and those reported by Nakashima et al. (2007), for the same swimming motion. However, a similar analysis is required for the remaining structures of the biomechanical model to ensure consistency with the expected behaviour of the human swimming motion. Lastly, the magnitude of the fluid forces computed for LHBM shows large discrepancies during some intervals of the stroke. These discrepancies are expected to repercuss on the results of the inverse dynamic analysis.

A final remark is made regarding the biggest limitations found in the software Swumsuit:

1. The simulation model has been found to be within 7.5% error against the experimental values, as reported by Nakashima et al. (2007).
2. The fluid forces are calculated without solving the flow field. Although it becomes advantageous from the computational time point of view, it does not consider neither the effects of the surrounding walls nor the mutual interaction of limbs. In front crawl swimming analysis, the latter

aspect is tremendous since both the leg kick and the arm stroke generate vortices that characterise the motion of the body segments. Neglecting their role in the overall body motion should impact the results of the estimated fluid forces (Andersen and Sanders, 2018; Takagi et al., 2015).

3. Although Swumsuit allows importing of the swimmer's absolute body motion, i.e., the linear and angular velocities of the whole-body COM for all time steps of the stroke cycle, the simulation program cannot solve the kinematic analysis of an acquired motion. Therefore, the kinematic analysis must be performed *a priori* in a different program, and then the linear and angular velocities are provided to Swumsuit, according to the simulation software specifications.
4. As described in Section 6.2.3, the motion given as rotations of body segments in the `joint_motion.dat` file is influenced by the order in which these rotations are written, which is to be expected as rotations cannot be added, i.e., in 3D the rotations do not have the additive property. Considering that a Cartesian coordinates formulation is considered in this study, it becomes troublesome the transformation from Euler parameters to the rotation sequences expected by Swumsuit, especially due to the complexity and variety of segmental movements from upper to lower limbs. This may be a potential source of error on the estimation of fluid forces due to discontinuities in the rotation angles for some intervals of the analysis, thus suggesting that a more robust transformation of rotations should be identified.

7. Inverse Dynamic Analysis of Determinate Biomechanical Systems

In this chapter, the solution of the determinate inverse dynamic analysis of the six-beat front crawl swimming motion performed in LABIOMEP-UP is presented. In this application, the DOF of the multibody system are actuated upon by driver actuators at the joints, instead of muscles. From the physiological point of view, these results are not characteristic of a biological system. However, they represent the lumped action of the muscles about the joints during a specific human motion, thus providing insight into valuable information and biomechanical modelling requirements. The results of the swimming motion under analysis are presented and discussed for the principal joints of the human lower limbs.

7.1. Solution of the Determinate Inverse Dynamic Analysis

In an inverse dynamics approach, the equations of motion of a multibody system are solved for a set of unknown parameters, defined as Lagrange multipliers, $\boldsymbol{\lambda}$. The solution of the system of non-linear equations requires the consistent kinematic data, the global biomechanical mass matrix, and the vector of externally applied forces as input data, as expressed in Equation (*4-25*). The Lagrange multipliers consist of a measure of the intersegmental forces that are developed by the kinematic constraints. Thus, the internal product of the vector of Lagrange multipliers by the transpose of the Jacobian matrix of the multibody system provides the intersegmental joint forces and joint torques developed by the driver actuators described in Section 4.3.5 at the kinematic joints.

The global components of the intersegmental joint forces of the hip, knee, and ankle joints are discussed in the following section, along with the joint torques developed during the swimming motion.

7.2. Results and Discussion

The profile and magnitude of the intersegmental forces and joint torques during the six-beat front crawl swimming motion are shown in Figure 7-1 and Figure *7-2*, respectively, for the hip, knee, and ankle joints.

(a)

(b)

(c)

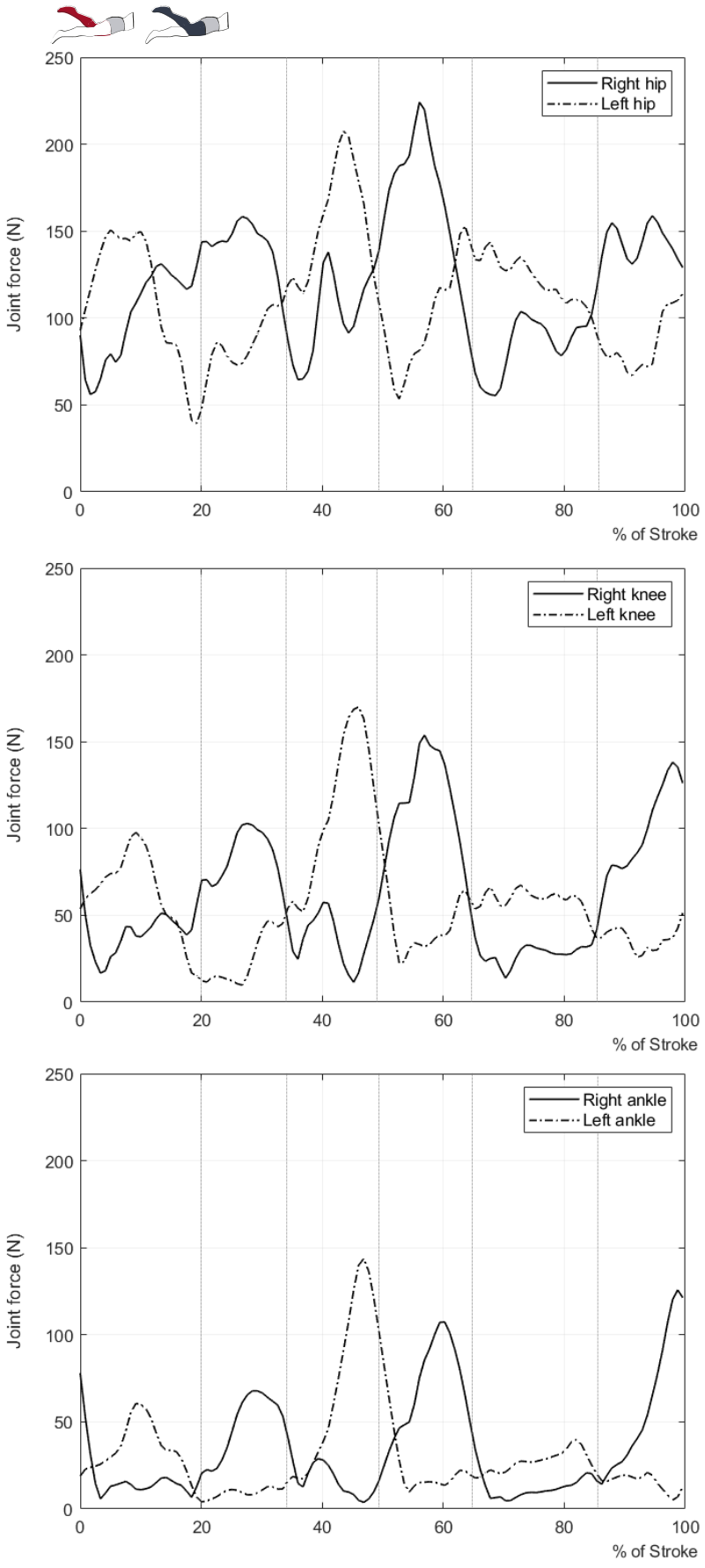

Figure 7-1: Intersegmental forces magnitude obtained during a left-hand six-beat front crawl swimming stroke cycle in the a) hip, b) knee, and c) ankle joints. The horizontal axis corresponds to a percentage of the stroke cycle.

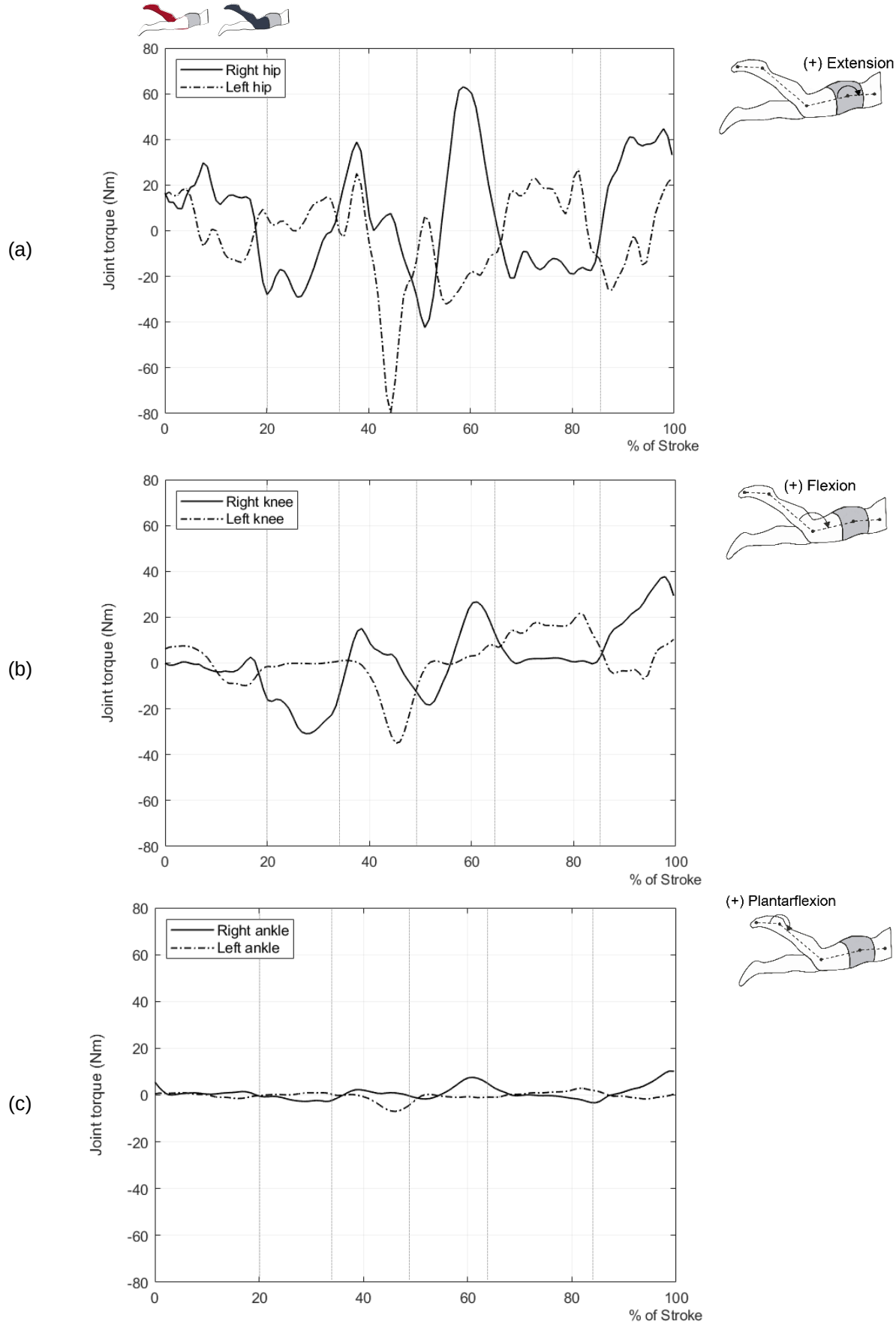

Figure 7-2: Joint torques obtained during a left-hand six-beat front crawl swimming stroke cycle in the a) hip, b) knee, and c) ankle joints. The horizontal axis corresponds to a percentage of the stroke cycle.

During the recovery phase, the arm stroke travels above the head. Due to the differences in fluid density between air and water, the force decreases by around 800 times for any body part out of the water (Keys, 2010). Therefore, the external forces acting upon the arm that moves above water during the recovery phase are nearly zero. Harrison et al. (2014) used a coupled Biomechanical-Smoothed Particle Hydrodynamics (B-SPH) model to calculate the joint torques for the arms of a male swimmer performing the front crawl stroke. The analysis proved that the joint torque is approximately zero during the recovery phase, and small, but non-zero, in the entry phase. Contrary to the upper limbs, the entire motion of the lower limbs occurs underwater. Although it highly depends on the swimmer's ability and technique, the concept of keeping the feet submerged at all time steps is expected to contribute to body propulsion and avoid wave drag (Keys, 2010). Because of that, thighs, legs, and feet are acted upon by external forces throughout the entire stroke.

The results obtained in the current work show that the intersegmental forces of the right and left joints of the lower limbs are never null. However, for the knee and ankle joints, their value is very small during some intervals of the stroke (3-18%, 44-49%, and 68-84% for the right lower limb; 20-38%, 52-68%, and 95-100% for the left lower limb). Considering the analyses in Sections 5.4.1 and 6.3, the larger and smaller peaks in Figure 7-1, correspond, respectively, to the three downbeats and three upbeats of each leg. During the upbeat, extension of the thigh occurs at the hip, followed by the upward motion of the leg and foot. Consequently, these bodies reach a position near the water surface and the joint force decreases, as is the case of the hand during the entry phase. If the ankle and knee joint forces are compared at the instants depicted in Figure 6-6, it can be observed that their magnitudes are lower when the body segments move closer to the water surface. Furthermore, the development of larger peaks during the downbeat of the lower limbs is consistent with the analysis of the external forces performed in Chapter 6 for the right lower limb, since during this phase the force created by the surrounding water over the body parts of the lower limbs is higher, propelling the body forward.

However, from the results in Figure 7-1, the magnitude of the intersegmental forces at the right knee and ankle joints ranges from nearly 0 to 150 N and 125 N, respectively, while the right hip joint forces are up to 225 N. On the other hand, the analysis performed in Section 6.3 verified that the higher hydrodynamic forces are registered for the foot. This shows that peak loads at the kinematic joints are not uniquely due to the magnitude of the external hydrodynamic forces acting upon the adjacent body segments. If it was so, the results of the ankle joint forces should correspond to the highest magnitudes. Instead, it is verified that the intersegmental forces are dependent on the combined effects of the external hydrodynamic forces plus the active joint forces necessary for controlling the joint motion, in this case, hip, knee, and ankle flexion and extension. Considering the nature of motion of the leg kick described in Section 5.4, the swimmer moves his lower limbs from the proximal to the distal bodies. Being the hip the first element of the kinematic chain of the human lower limbs, higher intersegmental forces are concentrated at this joint. Despite the intra-cycle variations among joints, the comparison between the force amplitudes of the right and the left sides is very similar for all joints. Table 7-1 details the peak-to-peak force amplitudes for all joints.

Considering the convention for the joint toques depicted in Figure 7-2, the joint torque at the hip should be positive (extension) during the upbeat, and negative (flexion) in the downbeat. The knee should produce a positive joint torque (flexion) at half of the upbeat and in the transition to downbeat. On the other hand, a negative joint torque (extension) is produced at half of the downbeat and in the transition to the upbeat sequence. The ankle joint torque is expected to be positive (plantarflexion) during the downbeat, when the propulsion from the lower limbs is maximal, and negative (dorsiflexion) at half of the upbeat.

The stroke cycle under analysis begins with the downbeat of the left lower limb. In Figure 7-2(a), the left hip joint torque changes from positive to negative, while the hip is flexing and moving towards the bottom of the swimming pool. Accordingly, the left leg follows the thigh, and the left knee is extended (negative joint toque in Figure 7-2(b)). The left ankle joint torque in Figure 7-2(c) is approximately zero during the first half of the downbeat (0-10%) and becomes negative during the second half (10-20%), which means that the articular moment has the opposite direction (dorsiflexion). As mentioned in the previous paragraph, the left ankle joint torque was expected to be positive during this interval, since it corresponds to the downbeat sequence of the respective lower limb. A possible reason for the incongruity is due to the external hydrodynamic forces acting upon the left foot during this period, i.e., although the left foot is in plantarflexion, as seen in Figure 5-8(c), the external forces cause a negative joint torque at the left ankle. Simultaneously, the right lower limb performs the upbeat. Accordingly, the right hip joint torque is positive as the right thigh moves upwards (hip extension), and the right knee changes from negative to positive torques while flexing. During the same interval, the right ankle joint torque becomes positive.

In general, the results for the hip and knee joints show agreement throughout the cycle for both sides of the lower limbs. The joint torque variation is consecutively alternating according to the downbeat and upbeat sequences. However, the variation of the right and left ankle joint torques does not follow the expected behaviour throughout the entire stroke cycle. During the first half (0-50%), the joint torques are negative on the downbeat (dorsiflexion), and positive during the upbeat (plantarflexion) of the respective lower limb, but during the second half cycle (50-100%) they change to the expected variation. For instance, the second downbeat of the right leg begins at approximately 51% of the cycle and lasts until 64%. During this interval, the right lower limb moves downwards. The external hydrodynamic forces acting upon the right foot have the opposite direction of motion, which contributes to a positive moment at the right ankle joint, and therefore corresponding to a positive torque in Figure 7-2(c). Nevertheless, the joint torques for the ankle joints are one order of magnitude lower than those for the hip and knee joints.

Analogously to the intersegmental forces, the joint torques are of greater magnitude for the hips. The amplitudes defined as the difference between maximum and minimum values for the right and left lower limbs are given in Table 7-1.

Table 7-1: Differences between the amplitudes of intersegmental forces and joint torques of the hip, knee, and ankle. The difference is computed as the measured peak-to-peak magnitude.

Joint		Intersegmental forces		Joint torques	
		Peak force [N]	Difference [N]	Peak [Nm]	Difference [Nm]
Hip	Right	224.2	169.41	62.99 (extension)	105.37
	Left	207.5	168.22	79.66 (flexion)	106.56
Knee	Right	153.8	142.35	37.67 (flexion)	68.49
	Left	170.0	158.79	35.03 (extension)	56.79
Ankle	Right	125.7	121.93	10.27 (plantarflexion)	13.59
	Left	143.8	139.76	7.02 (dorsiflexion)	9.93

Due to the lack of literature on joint torques and intersegmental joint forces in the context of human swimming motion, validation of the obtained results is not possible at this stage. The only study found in the literature in which the hip joint torques are demonstrated for a front crawl swimming motion was developed by Nakashima et al. (2015). The work aimed to investigate the effect of knee joint motion on the swimming performance of a male subject with a transfemoral prosthesis. The individual is an experienced swimmer with an acquired one-sided transfemoral amputation of the right lower limb. Consequently, only the joint torques obtained for the healthy leg (the left leg) are used for comparison in this work.

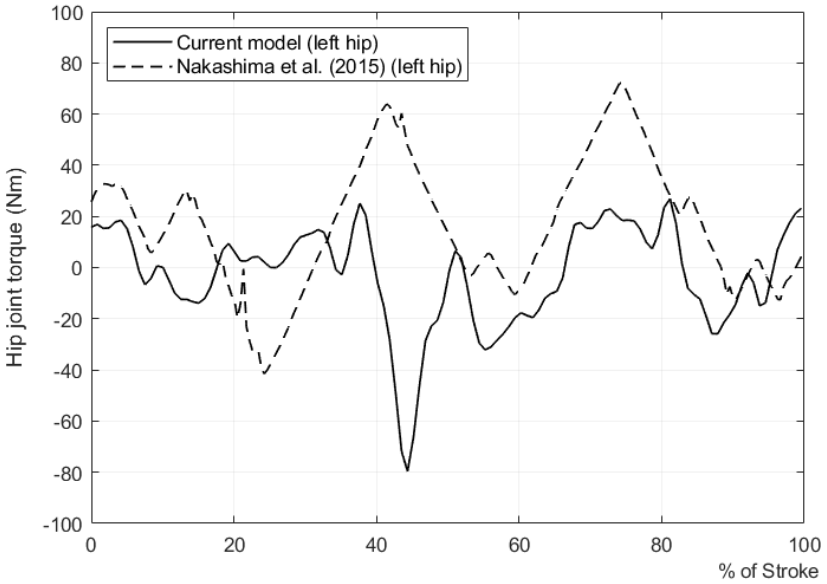

Figure 7-3: Joint torques at the left hip obtained in the current work (solid line), and reported by Nakashima et al. (2015) (dashed line). The horizontal axis corresponds to a percentage of the stroke cycle.

The results obtained reveal several differences between both models. However, one aspects related with the definition of the hip joint centre must be considered. Nakashima et al. (2015) defined the hip joint centre as the position of the markers of the trochanter (see Appendix A). This assumption has tremendous implications and repercussions in the accuracy and interpretation of results (Hara et al., 2016). With that being said, the data reported by Nakashima et al. (2015) is used only to evaluate the

expected torque amplitude of the hip joint. The difference between peak to peak resulted in a total amplitude of 113.5 Nm, against 105.37 Nm and 106.56 Nm obtained in the current work for the right and left hip joints, respectively, as depicted in Table 7-1. Both differences are of the same order of magnitude, and very similar, which provides some confidence in the results.

Additionally, the joint torques of the upper limbs reported by Harrison et al. (2014) were of greater magnitude for the proximal joints, which is identical to the results obtained in this work for the lower limbs. The joint torque magnitudes decrease from the hip to the ankle joint, as shown in Figure 7-2. On the other hand, the difference from peak-to-peak reported by Harrison et al. (2014) was 176 Nm for the shoulder, 85 Nm for the elbow, and 17 Nm for the wrist joint. As mentioned in Chapter 6, in front crawl swimming the upper limbs are responsible for the most part of the overall body propulsion. This is verified for the current results since the torque magnitudes obtained for all joints of the lower limbs are below the values reported for the upper limbs.

The results obtained from the inverse dynamic analysis performed underly the importance of considering the whole system dynamics of the human lower limbs during front crawl swimming, and not only the feet. Despite the apparent consistency of some results, the biomechanical model developed requires further validation. Although the dynamic pattern estimated seems to represent the mechanisms of front crawl swimming in the lower limbs, with the major discrepancies occurring with the ankle joints, the intersegmental forces and joint torques are expected to be greater in this work because of the high hydrodynamic forces obtained in Chapter 6 during some phases of the stroke cycle, when compared to Nakashima et al. (2007) and Keys (2010). From the analysis of those intervals in the animation of Swumsuit, they correspond to situations in which the feet are not properly positioned relative to the adjacent body. The reason for that may be due to the movement performed by the swimmer, or a more plausible source of error is related with the order of rotations given in the simulation input file. The latter has an immediate impact on the contact surface area of the feet with water, and thus in the generated joint forces. Since the vector of external forces is an explicit input of an inverse dynamic analysis, the results here obtained are certainly higher.

8. Conclusions

This work studies the dynamic behaviour of the human lower limbs during a six-beat front crawl swimming motion. The comprehensive, three-dimensional mathematical model of the full human body developed in MATLAB uses a multibody based formulation in which the position and orientation of the anatomical segments are represented by Cartesian coordinates. The model is driven through an acquired motion by joint torque actuators that drive the degrees of freedom of the anatomical articulations, represented as ideal kinematic joints. In order to determine the external hydrodynamic forces during swimming, the simulation software Swumsuit developed by Nakashima et al. (2007) is used. The second accomplishment and novel feature of the present work consists in the development of an interface between Swumsuit and LHBM. The aim of the interface is twofold: the first is to allow the computation of the kinetic data developed for the actual swimming motion and give as input to the inverse dynamic analysis; the second concerns the development of a general adjustment procedure and integration in a pre-existing program that performs data processing and kinematic consistency analysis, thus allowing the study of different subjects and types of swimming techniques obtained by motion capture systems. The results of the inverse dynamic analysis are discussed for the principal articulations responsible for the motion of the human lower limbs, i.e., the hip, knee, and ankle joints.

A three-dimensional full body biomechanical model was developed based on the dataset of Dumas et al. (2007a; 2007b), except for the head and neck anatomical segments that followed the topology presented by Pàmies-Vilà (2012). The complete dataset provides the scaling equations for the body segment inertial parameters, thus ensuring the fitting of the anthropometric data between the biomechanical model and the subject under analysis.

The kinematic data of the six-beat front crawl swimming motion provided by LABIOMEP-UP were treated and filtered to remove the noise related to the position of the anatomical markers. The kinematic joints of the hip, lumbar, cervical, shoulder, and atlanto-occipital were defined based on predictive methods to better represent the actual centres of rotation, while the remaining joints were determined as the midpoint between anatomical landmarks. A kinematic analysis was performed to ensure the kinematic consistency between the biomechanical model and the actual swimming motion. The results of the driving angles of the hip, knee, and ankle joints provided confidence with those reported by Nakashima et al. (2007). However, there is still some concern regarding the ankle joint motion, especially during the intervals in which the foot is near the water surface, i.e., in the transition from the upbeat to the downbeat of the respective lower limb. The rolling action of the swimmer's body along its longitudinal axis was also evaluated in terms of shoulder roll and hip roll. The roll-time profile of the shoulders showed similarity with the results of Psycharakis and Sanders (2008). On the other hand, the rhythm characteristics of the hips registered higher range of motion, possibly due to breathing.

The simulation software Swumsuit was used in this work to obtain the hydrodynamic forces acting upon the swimmer's body during the six-beat front crawl swimming. The simulation program allows the computation of the fluid forces acting on each segment of the human body model (SWUM). The

unsteady fluid forces are computed without solving the flow field. Instead, they are determined from the local kinematics of each part of the human body at each time step, and from the force coefficients estimated experimentally (Nakashima et al., 2007). The conversion of the software input data from LHBM to the SWUM, i.e., body geometry data, kinematic data, and analysis settings parameters, and from that to the inverse dynamics program, accordingly, external forces acting upon the body segments of LHBM, was embedded in an interface that was developed in a general-based methodology to allow future research and a larger variety of subject data and swimming motion techniques to be studied. Despite specific cases in which the researcher pretends to change the fluid force coefficients, the number of cycles to simulate, or other parameters of the analysis, the conversion procedure is fully implemented, being the computing time the only variable that differs significantly among studies. From this point of view, Swumsuit is much less time consuming than other simulation software programs, such as CFD and SPH. The forces generated at the right thigh, leg, and foot over a stroke cycle were compared to Nakashima et al. (2007). The results showed that the computed hydrodynamic forces are overestimated during some phases of the stroke cycle, especially in the X, Y, and Z components of the right foot. These intervals of overestimated forces coincide with abnormalities in the orientation of the foot as shown in the software animation. Despite any inaccuracies, larger peaks were visible during the downbeat of the lower limbs, which link the downbeat to the propulsive sequence of the leg kick, as reported in the literature (Guignard et al., 2019). Moreover, the results achieved on the overall hydrodynamic forces of the lower limbs supported the importance of considering the contribution of the thighs and legs on the generation of body propulsion rather than just the feet (Keys, 2010).

The inverse dynamic analysis was solved considering the full body biomechanical model actuated upon by driver actuators, referred to as determinate problem. The results of the intersegmental joint forces and moments acting at the kinematic articulations of the human lower limbs were analysed in the current work. Since these quantities are not generally described in the literature it was not possible to compare the results with those of other authors.

The intersegmental forces represent the net loads that act at the joints. According to Derrick et al. (2020), the external forces acting upon the body segments of the biomechanical model are often many times smaller than the actual joint contact forces. This occurs because the magnitude of the contact joint forces depends on the combined effects of the external forces, in this case, the hydrodynamic forces, plus the active joint forces necessary for controlling joint motion (flexion and extension) (Scott and Winter, 1990). The results obtained showed that the magnitude of the intersegmental forces is much higher than the magnitude of the hydrodynamic forces obtained for the lower limbs. Also, the higher magnitudes of intersegmental forces occur at the hip joints. These results are consistent with Scott and Winter (1990) in a way that the external hydrodynamic forces are not the only influence over the joint force magnitudes. Considering the motion profile of the leg kick, the swimmer moves his lower limbs from the proximal to the distal joints. Possibly the controlling action of the hip flexion/extension during the down/upbeat of the entire lower limb, respectively, contributes to the higher magnitudes at this joint.

The results of the joint forces also showed that they are higher during the downbeat sequences of the respective lower limb and smaller during the upbeat. In the transition from up to downbeat, when the leg and foot are closer to the water surface, the knee and ankle joint forces reach their minimum values.

Regarding the joint torques, the results obtained for the hip and knee joints are thought to show agreement with the expected variation from positive and negative values during the down and up kicks of the lower limbs. On the other hand, the ankle joint torques do not represent the same consistency throughout the entire stroke. Once again, one possible reason for the non-consistency is related to the incorrect position of the foot during some phases of the stroke, thus influencing the external forces acting upon the foot.

One single research paper was found in the literature that reported the hip joint torque during a six-beat front crawl swimming (Nakashima et al., 2015). However, the hip joint centre was defined as the position of the marker of the trochanter, which is a completely different definition from that considered in this work. Therefore, the results reported by Nakashima et al. (2015) were compared only in terms of joint torque amplitudes, which were very similar to those determined for both hips.

Finally, one of the difficulties found in this work remains with a robust description of the body rotations and the accurate transformation from Euler parameters to rotation sequences in Swumsuit. The animation in Swumsuit showed that during some phases of the stroke, the position of the foot relative to the leg is not correct. Simultaneously, the generated hydrodynamic forces are overestimated. It is expected that these results have influenced the intersegmental joint forces and joint torques.

Another aspect consists in the approximation performed during the conversion of the distributed forces in SWUM to the reference frame of LHBM. The force acting at the centre of each thin plate of the longitudinal axis was added by 1/10 of the total buoyancy force component missing to that body, independently from the distinction between submerged and non-submerged thin plates, using the terminology depicted in Swumsuit.

8.1. Future Work

Even if the full body biomechanical model developed in the current work provides generally good results regarding the kinematic analysis of the human lower limbs, several limitations are still present in the kinematics validation of the upper limbs. Due to the complexity of movements in front crawl swimming and wide range of motion performed, especially during the arm stroke, the LABIOMEP-UP markers setup protocol described in Appendix A was initially analysed with the objective of introducing new markers that would allow the discretisation of the biomechanical model. However, due to the COVID-19 pandemic no kinematic data acquisitions were performed during this dissertation. Therefore, the development of the biomechanical model was limited to the available data. Future work should be developed regarding the discretisation of the shoulder complex if the interest of the analysis changes for the upper limbs, or even for different swimming techniques, such as breaststroke, butterfly, or backstroke.

Furthermore, fundamental quantities of interest in human motion research are the intersegmental forces and moments acting at the joints (Derrick et al., 2020). The location of the centre of rotation of the kinematic joints is either obtained through functional or predictive methods, although the latter are most used since offer a simpler implementation while delivering good results (Hara et al., 2016; Murphy et al., 2011). The accuracy of these regression equations has a strong repercussion in the goodness of the computed intersegmental joint forces and joint moments. Simultaneously, the selection criteria of a regression equation over another depends upon the available kinematic data, namely the position of bony landmarks. Further investigations on more accurate predictions of the HJC, LJC, SJC, CJC, and OJC could be performed according to the availability of more relevant kinematic data.

In the present work, the flexion and extension of the hip, knee, and ankle joints were studied, since they represent the main motions that characterise the leg kick (Matsuda et al., 2016). However, future work should evaluate the kinematics of a wide range of motions, to validate the consistency of the kinematic analysis performed. For instance, in breaststroke, the motion of the lower limbs cannot be evaluated only in terms of flexion and extension of the anatomical joints.

A very important aspect that requires further investigation is related with the interface developed between Swumsuit and LHBM for the determination of the hydrodynamic forces during swimming. As this presents a novel feature in this work, several tests should be conducted to validate the implemented methodology. The main points for improvement found to date are depicted in the following:

1. The motion given as rotations of body segments in the `joint_motion.dat` file is influenced by the order in which these rotations are written. The complexity and variety of segmental movements from upper to lower limbs induce some discontinuities in the rotation angles for some intervals of the analysis, especially for the body segments with a higher range of motion. The conversion of the rotation angles from LHBM to Swumsuit should be improved to eliminate these discontinuities.
2. Because of (1), during the intervals of discontinuities the position of the body segments in the water does not represent the reality. The results found in this work speculate that this represents the potential source of error for the overestimated hydrodynamic forces. However, further possibilities may be investigated.
3. Since this dissertation was focused on the dynamics of the human lower limbs, it is recommended to compare the hydrodynamic forces with other studies in the literature for the remaining body segments. In front crawl swimming, several analyses using CFD and SPH numerical methods are conducted for the upper limbs, as they contribute with the most part of the total body propulsion (Cohen et al., 2015; Guignard et al., 2019; Samson et al., 2017).
4. Since Swumsuit does not solve the flow field, evaluate the impact on the computed hydrodynamic forces of not considering the unsteady fluid effects, such as the generation of vortices, the effects of the surrounding walls, and the mutual interactions of limbs.

There have been no studies of the multibody system dynamics of human swimming because external forces are very difficult to measure. Current works in the literature are more frequently focused on the analysis of specific hydrodynamic factors that contribute to performance, than on the comprehension of

internal aspects of the human body dynamics, namely intersegmental joint forces and joint torques. Because of that, there is a lack of literature that may be used to validate the results achieved in this dissertation. Future research in this area requires the development of more swimming motion analyses and improvement on the interface developed to discuss whether the results are within the expected range.

It is worth noting that joint torque and intersegmental joint forces calculations do not directly predict magnitudes of muscle forces. Future work will also involve incorporating muscle models to calculate muscle, tendon, and ligament forces and muscle work. In addition, improvements in motion capture technology will permit more detailed 3D modelling systems, including electromyography data collection to discuss more quantitatively the muscle forces during swimming.

9. References

Andersen, J. T. (2019). *Movement Characteristics of Front Crawl Swimming at Sprint Pace and Middle-Distance Pace: Establishing Demands on the Torso Muscles*. PhD Thesis, Faculty of Health Sciences, University of Sydney.

Andersen, J. T., & Sanders, R. H. (2018). A systematic review of propulsion from the flutter kick – What can we learn from the dolphin kick? *Journal of Sports Sciences*. https://doi.org/10.1080/02640414.2018.1436189

Andersen, M. S., Damsgaard, M., & Rasmussen, J. (2009). Kinematic analysis of over-determinate biomechanical systems. *Computer Methods in Biomechanics and Biomedical Engineering*, *12*(4), 371–384. https://doi.org/10.1080/10255840802459412

Arellano, R., Pardillo, S., De La Fuente, B., & García, F. (2000). A System to Improve the Swimming Start Technique Using Force Recording, Timing and Kinematic Analyses. *In XVIII Symposium of the International Society of Biomechanics in Sports*, 609–613.

Barber, M. (2013). *The Effect of Breathing on Hip Roll Asymmetry in Competitive Front Crawl Swimming*. MSc Thesis in Kinesiology and Health Studies, Faculty of Graduate Studies and Research, University of Regina.

Benjanuvatra, N., Edmunds, K., & Blanksby, B. (2007). Jumping Ability and Swimming Grab-Start Performance in Elite and Recreational Swimmers. *International Journal of Aquatic Research and Education*, *1*(3), 231–241. https://doi.org/10.25035/ijare.01.03.06

Bergmann, G., Deuretzabacher, G., Heller, M., Graichen, F., Rohlmann, A., Strauss, J., & Duda, G. N. (2001). Hip forces and gait patterns from routine activities. *Journal of Biomechanics*, *34*, 859–871.

Bixler, B., & Riewald, S. (2002). Analysis of a swimmer's hand and arm in steady flow conditions using computational fluid dynamics. *Journal of Biomechanics*, *35*(5), 713–717. https://doi.org/10.1016/S0021-9290(01)00246-9

Cascais, C., Sousa, A., Ribeiro, J., Silva, A., Pelarigo, J., Vilas-Boas, J. P., Figueiredo, P., & Fernandes, R. (2014). *Comportamento fisiológico a diferentes intensidades do VO2 máx: comparação entre nadadores especialistas em diferentes distâncias*. Lecturas: Educación Física y Deportes. https://www.efdeportes.com/efd198/comportamento-fisiologico-entre-nadadores.htm

Ceccon, S., Ceseracciu, E., Sawacha, Z., Gatta, G., Cortesi, M., Cobelli, C., & Fantozzi, S. (2013). Motion analysis of front crawl swimming applying CAST technique by means of automatic tracking. *Journal of Sports Sciences*, *31*(3), 276–287. https://doi.org/10.1080/02640414.2012.729134

Cleary, P. W., Cohen, R. C. Z., Harrison, S. M., Sinnott, M. D., Prakash, M., & Mead, S. (2013). Prediction of industrial, biophysical and extreme geophysical flows using particle methods. *Engineering Computations*, *30*(2), 157–196. https://doi.org/10.1108/02644401311304845

Cleather, D. J., & Bull, A. M. J. (2015). The development of a segment-based musculoskeletal model of the lower limb: introducing FREEBODY. *Royal Society Open Science*, *2*. https://doi.org/10.1098/rsos.140449

Cohen, R. C. Z., Cleary, P. W., & Mason, B. R. (2009). Simulations of human swimming using Smoothed Particle Hydrodynamics. *7th International Conference on CFD in the Minerals and Process Industries*.

Cohen, R. C. Z., Cleary, P. W., & Mason, B. R. (2010). Improving understanding of human swimming using smoothed particle hydrodynamics. *IFMBE Proceedings*, *31*, 174–177. https://doi.org/10.1007/978-3-642-14515-5_45

Cohen, R. C. Z., Cleary, P. W., Mason, B. R., & Pease, D. L. (2015). The Role of the Hand During Freestyle Swimming. *Journal of Biomechanical Engineering*, *137*(11). https://doi.org/10.1115/1.4031586

Cortesi, M., Giovanardi, A., Gatta, G., Mangia, A. L., Bartolomei, S., & Fantozzi, S. (2019). Inertial Sensors in Swimming: Detection of Stroke Phases through 3D Wrist Trajectory. *Journal of Sports Science and Medicine*, *18*, 438–447.

Davies, G. J., Matheson, J. W., Ellenbecker, T. S., & Manske, R. (2009). The Shoulder in Swimming. In K. E. Wilk, M. M. Reinold, & J. R. Andrews (Eds.), *The Athlete's Shoulder* (Second Edi, pp. 445–463). Churchill Livingstone. https://doi.org/10.1016/B978-044306701-3.50039-6

Dempster, W. T., & Gaughran, G. R. L. (1967). Properties of Body Segments Based on Size and Weight. *American Journal of Anatomy*, *120*, 33–54.

Derrick, T. R., van den Bogert, A. J., Cereatti, A., Dumas, R., Fantozzi, S., & Leardini, A. (2020). ISB recommendations on the reporting of intersegmental forces and moments during human motion analysis. *Journal of Biomechanics*, *99*. https://doi.org/10.1016/j.jbiomech.2019.109533

Dumas, R., Chèze, L., & Verriest, J. P. (2007a). Adjustments to McConville et al. and Young et al. body segment inertial parameters. *Journal of Biomechanics*, *40*(3), 543–553. https://doi.org/10.1016/j.jbiomech.2006.02.013

Dumas, R., Chèze, L., & Verriest, J. P. (2007b). Corrigendum to "Adjustments to McConville et al. and Young et al. body segment inertial parameters" [J. Biomech. 40 (2007) 543-553]. *Journal of Biomechanics*, *40*(7), 1651–1652. https://doi.org/10.1016/j.jbiomech.2006.07.016

Gourgoulis, V., Boli, A., Aggeloussis, N., Toubekis, A., Antoniou, P., Kasimatis, P., Vezos, N., Michalopoulou, M., Kambas, A., & Mavromatis, G. (2013). The effect of leg kick on sprint front crawl swimming. *Journal of Sports Sciences*, *32*(3), 278–289. https://doi.org/10.1080/02640414.2013.823224

Guignard, B., Chollet, D., Vedova, D. D., Rouard, A., Bonifazi, M., Hart, J., & Seifert, L. (2019). Upper to lower limb coordination dynamics in swimming depending on swimming speed and aquatic

environment manipulations. *Motor Control*, *23*(3), 418–442. https://doi.org/10.1123/mc.2018-0026

Hall, G. (2020). *Three Styles of Freestyle - Hip Driven Freestyle Technique*. Swimswam. https://swimswam.com/three-styles-of-freestyle-hip-driven-freestyle-technique/

Hall, S. J. (2012). *Basic Biomechanics* (McGraw-Hill (Ed.); Sixth Edit). William Glass.

Hara, R., McGinley, J., Briggs, C., Baker, R., & Sangeux, M. (2016). Predicting the location of the hip joint centres, impact of age group and sex. *Scientific Reports*, *6*. https://doi.org/10.1038/srep37707

Harrington, M. E., Zavatsky, A. B., Lawson, S. E. M., Yuan, Z., & Theologis, T. N. (2007). Prediction of the hip joint centre in adults, children, and patients with cerebral palsy based on magnetic resonance imaging. *Journal of Biomechanics*, *40*(3), 595–602. https://doi.org/10.1016/j.jbiomech.2006.02.003

Harrison, S. M., Cohen, R. C. Z., Cleary, P. W., Mason, B. R., & Pease, D. L. (2014). Torque and power about the joints of the arm during the freestyle stroke. *12th International Symposium on Biomechanics and Medicine in Swimming*, 349–355.

Honda, K., Keys, M., Lyttle, A., Alderson, J., Bennamoun, M., & El-sallam, A. (2012). Freestyle swimming: an insight into propulsive and resistive mechanisms. *30th Annual Conference on Biomechanics in Sports*, 96–99.

Horsman, M. D. K., Koopman, H. F. J. M., van der Helm, F. C. T., Prosé, L. P., & Veeger, H. E. J. (2007). Morphological muscle and joint parameters for musculoskeletal modelling of the lower extremity. *Clinical Biomechanics*, *22*(2), 239–247. https://doi.org/10.1016/j.clinbiomech.2006.10.003

Ishikawa, M., Komi, P. V., Grey, M. J., Lepola, V., & Bruggemann, G.-P. (2005). Muscle-tendon interaction and elastic energy usage in human walking. *Journal of Applied Physiology*, *99*, 603–608. https://doi.org/10.1152/japplphysiol.00189.2005

Jensen, R. K., & McIlwain, J. (1979). Modeling of lower extremity forces in the dolphin kick. In E. W. Bedingfield & J. Terauds (Eds.), *Swimming III: Proceedings of the Third International Symposium of Biomechanics in Swimming, University of Alberta, Edmonton, Canada* (pp. 137–147). University Park Press 1979.

Jesus, K. de, Mourão, L., Roesler, H., Viriato, N., Jesus, K. de, Vaz, M., Fernandes, R., & Vilas-Boas, J. P. (2019). 3D Device for Forces in Swimming Starts and Turns. *Applied Sciences*, *9*(17). https://doi.org/10.3390/app9173559

Keys, M. (2010). *Establishing computational fluid dynamics models for swimming technique assessment*. PhD Thesis, School of Civil and Resource Engineering/School of Sports Science, Exercise and Health, The University of Western Australia.

Langholz, J. B., Westman, G., & Karlsteen, M. (2016). Musculoskeletal Modelling in Sports - Evaluation of Different Software Tools with Focus on Swimming. *Procedia Engineering*, *147*, 281–287. https://doi.org/10.1016/j.proeng.2016.06.278

Lauer, J., Rouard, A. H., & Vilas-Boas, J. P. (2016). Upper limb joint forces and moments during underwater cyclical movements. *Journal of Biomechanics*, *49*(14), 3355–3361. https://doi.org/10.1016/j.jbiomech.2016.08.027

Lower extremity: Anatomy study course | Kenhub. (n.d.). Retrieved March 24, 2020, from https://www.kenhub.com/en/start/lower-extremity

Lund, M. E., Andersen, M. S., de Zee, M., & Rasmussen, J. (2015). Scaling of musculoskeletal models from static and dynamic trials. *International Biomechanics*, *2*(1), 1–11. https://doi.org/10.1080/23335432.2014.993706

Matsuda, Y., Hirano, M., Yamada, Y., Ikuta, Y., Nomura, T., Tanaka, H., & Oda, S. (2016). Lower muscle co-contraction in flutter kicking for competitive swimmers. *Human Movement Science*, *45*, 40–52. https://doi.org/10.1016/j.humov.2015.11.001

McConville, J. T., Churchill, T. D., Clauser, C. E., Cuzzi, J., & Kaleps, I. (1980). Anthropometric relationships of body and body segment moments of inertia. In *AFAMRL-TR-80-119, Aerospace Medical Research Laboratory, Wright-Patterson Air Force Base, Dayton, Ohio*.

Mullen, G. J. (2018). Swimming science: optimizing training and performance. In G. J. Mullen (Ed.), *University of Chicago Press*. Susan Kelly. https://doi.org/https://doi.org/10.7208/chicago/9780226287980.001.0001

Murphy, A. J., Bull, A. M. J., & McGregor, A. H. (2011). Predicting the lumbosacral joint centre location from palpable anatomical landmarks. *Proceedings of the Institution of Mechanical Engineers, Part H: Journal of Engineering in Medicine*, *225*(11), 1078–1083. https://doi.org/10.1177/0954411911416859

Nakashima, M. (2005). *Development of Computer Simulation Software "Swumsuit" to Analyze Mechanics of Human Swimming*. http://www.swum.org/Nakashima_ISCSB2005.pdf

Nakashima, M. (2006). "SWUM" and "SWUMSUIT" - A modelling technique of a self-propelled swimmer. *Portuguese Journal of Sport Sciences*, *6*(Supl. 2), 66–68.

Nakashima, M., Hasegawa, T., Kamiya, S., & Takagi, H. (2013). Musculoskeletal Simulation of the Breaststroke. *Journal of Biomechanical Science and Engineering*, *8*(2), 152–163. https://doi.org/10.1299/jbse.8.152

Nakashima, M., Ono, A., & Nakamura, T. (2015). Effect of knee joint motion for the transfemoral prosthesis in swimming. *Journal of Biomechanical Science and Engineering*, *10*(3), 1–12. https://doi.org/10.1299/jbse.15-00375

Nakashima, M., Satou, K., & Miura, Y. (2007). Development of Swimming Human Simulation Model Considering Rigid Body Dynamics and Unsteady Fluid Force for Whole Body. *Journal of Fluid Science and Technology*, *2*(1), 56–67. https://doi.org/10.1299/jfst.2.56

Nikravesh, P. E. (1988). *Computer-Aided Analysis of Mechanical Systems* (P. Hall (Ed.); First Edit).

Englewood Cliffs, New Jersey.

Oliveira, H. (2016). *Inverse Dynamic Analysis of the Human Locomotion Apparatus for Gait*. MSc Thesis in Mechanical Engineering, Instituto Superior Técnico, Universidade de Lisboa.

Pàmies-Vilà, R. (2012). *Application of Multibody Dynamics Techniques to the Analysis of Human Gait*. PhD Thesis in Biomedical Engineering, Universitat Politècnica de Catalunya.

Psycharakis, S. G., & Sanders, R. H. (2008). Shoulder and Hip Roll Changes during 200-m Front Crawl Swimming. *Medicine and Science in Sports and Exercise*, *40*(12), 2129–2136. https://doi.org/10.1249/MSS.0b013e31818160bc

Quental, C. (2013). *Biomechanical Tools for the Analysis of the Native and Prosthetic Shoulders*. PhD Thesis in Biomedical Engineering, Instituto Superior Técnico, Universidade de Lisboa.

Quental, C., Folgado, J., & Ambrósio, J. A. C. (2016). A window moving inverse dynamics optimization for biomechanics of motion. *Multibody System Dynamics*, *38*, 157–171. https://doi.org/10.1007/s11044-016-9529-4

Quental, C., Folgado, J., Ambrósio, J. A. C., & Monteiro, J. (2015). Critical analysis of musculoskeletal modelling complexity in multibody biomechanical models of the upper limb. *Computer Methods in Biomechanics and Biomedical Engineering*, *18*(7), 749–759. https://doi.org/10.1080/10255842.2013.845879

Rajagopal, A., Dembia, C. L., DeMers, M. S., Delp, D. D., Hicks, J. L., & Delp, S. L. (2016). Full-Body Musculoskeletal Model for Muscle-Driven Simulation of Human Gait. *IEEE Transactions on Biomedical Engineering*, *63*(10), 2068–2079. https://doi.org/10.1109/TBME.2016.2586891

Reed, M. P., Manary, M. A., & Schneider, L. W. (1999). Methods for Measuring and Representing Automobile Occupant Posture. *SAE International Technical Paper*. https://doi.org/10.4271/1999-01-0959

Samson, M., Bernard, A., Monnet, T., Lacouture, P., & David, L. (2017). Unsteady computational fluid dynamics in front crawl swimming. *Computer Methods in Biomechanics and Biomedical Engineering*, *20*(7), 783–793. https://doi.org/10.1080/10255842.2017.1302434

Sanders, R. H., Andersen, J. T., & Takagi, H. (2017). The Segmental Movements in Front Crawl Swimming. In B. Müller & S. I. Wolf (Eds.), *Handbook of Human Motion*. Springer, Cham. https://doi.org/10.1007/978-3-319-30808-1_132-1

Sanders, R. H., & Psycharakis, S. G. (2009). Rolling rhythms in front crawl swimming with six-beat kick. *Journal of Biomechanics*, *42*(3), 273–279. https://doi.org/10.1016/j.jbiomech.2008.10.037

Scott, S. H., & Winter, D. A. (1990). Internal forces at chronic running injury sites. *Medicine and Science in Sports and Exercise*, *22*(3), 357–369.

Silva, M. P. T. (2003). *Human Motion Analysis Using Multibody Dynamics and Optimization Tools*. PhD

Thesis in Mechanical Engineering, Instituto Superior Técnico, Universidade de Lisboa.

Silva, M. P. T., & Ambrósio, J. A. C. (2002). Kinematic data consistency in the inverse dynamic analysis of biomechanical systems. *Multibody System Dynamics*, *8*, 219–239. https://doi.org/10.1023/A:1019545530737

Silva, M. P. T., & Ambrósio, J. A. C. (2003). Solution of Redundant Muscle Forces in Human Locomotion with Multibody Dynamics and Optimization Tools. *Mechanics Based Design of Structures and Machines: An International Journal*, *31*(3), 381–411. https://doi.org/10.1081/SME-120022856

Takagi, H., Nakashima, M., Sato, Y., Matsuuchi, K., & Sanders, R. H. (2015). Numerical and experimental investigations of human swimming motions. *Journal of Sports Sciences*, *34*(16), 1564–1580. https://doi.org/10.1080/02640414.2015.1123284

Takagi, H., & Sanders, R. (2002). Measurement of propulsion by the hand during competitive swimming. *The Engineering of Sport*, *4*, 631–637.

TritonWear. (2020). *The Blueprint on How to Swim Freestyle Faster*. https://blog.tritonwear.com/the-blueprint-on-how-to-swim-freestyle-faster

van Houwelingen, J., Schreven, S., Smeets, J. B. J., Clercx, H. J. H., & Beek, P. J. (2017). Effective Propulsion in Swimming: Grasping the Hydrodynamics of Hand and Arm Movements. *Journal of Applied Biomechanics*, *33*(1), 87–100. https://doi.org/10.1123/jab.2016-0064

Von Loebbecke, A., Mittal, R., Mark, R., & Hahn, J. (2009). A computational method for analysis of underwater dolphin kick hydrodynamics in human swimming. *Sports Biomechanics*, *8*(1), 60–77. https://doi.org/10.1080/14763140802629982

Walker, A. (2020). *Freestyle Swimming Technique - Using Hip Rotation As a Power Source*. https://www.realbuzz.com/articles-interests/swimming/article/freestyle-swimming-technique-using-hip-rotation-as-a-power-source/

Washino, S., Mayfield, D. L., Lichtwark, G. A., Mankyu, H., & Yoshitake, Y. (2019). Swimming performance is reduced by reflective markers intended for the analysis of swimming kinematics. *Journal of Biomechanics*, *91*, 109–113. https://doi.org/10.1016/j.jbiomech.2019.05.017

Wei, T., Mark, R., & Hutchison, S. (2014). The Fluid Dynamics of Competitive Swimming. *Annual Review of Fluid Mechanics*, *46*, 547–565. https://doi.org/10.1146/annurev-fluid-011212-140658

Winter, D. A. (2009). *Biomechanics and Motor Control of Human Movement* (Fourth Edi). John Wiley & Sons, Inc. Hoboken, New Jersey. https://doi.org/10.1002/9780470549148

Wu, G., Siegler, S., Allard, P., Kirtley, C., Leardini, A., Rosenbaum, D., Whittle, M., D'Lima, D. D., Cristofolini, L., Witte, H., Schmid, O., & Stokes, I. (2002). ISB recommendation on definitions of joint coordinate system of various joints for the reporting of human joint motion - Part I: ankle, hip, and spine. *Journal of Biomechanics*, *35*(4), 543–548. https://doi.org/10.1016/s0021-9290(01)00222-6

Wu, G., van der Helm, F. C. T., Veeger, H. E. J., Makhsous, M., Van Roy, P., Anglin, C., Nagels, J., Karduna, A. R., McQuade, K., Wang, X., Werner, F. W., & Buchholz, B. (2005). ISB recommendation on definitions of joint coordinate systems of various joints for the reporting of human joint motion - Part II: shoulder, elbow, wrist and hand. *Journal of Biomechanics*, *38*(5), 981–992. https://doi.org/10.1016/j.jbiomech.2004.05.042

Xiao, T., & Fu, Y. F. (2016). Biomechanical Modeling of Human Body Movement. *Journal of Biometrics & Biostatistics*, *7*(3), 5–8. https://doi.org/10.4172/2155-6180.1000309

Appendix A: Marker Setup Protocol

The full body anatomical markers setup protocol for swimming applications in the Porto Biomechanics Laboratory (LABIOMEP-UP) are listed in Table A-1 and illustrated in Figure A-1.

Table A-1: Markers description and location on the subject's skin. The column labelled as "Used" identifies whether the marker was used to define the biomechanical model or not.

ID	Marker Name	Location	Used
1	C7	7th Cervical Vertebrae	✓
2	HEADFRONT	Forehead, above the nose	✓
3	HEADTOP	On the top of the head, vertically above the ears	✓
4	LAC	Left acromial edge of the scapula	✓
5	LASIS	Left Anterior Superior Iliac Spine	✓
6	LBACK	Left mid-distance between the scapula and pelvis	✗
7	LCA	Distal end of the posterior aspect of the left Calcaneus. Should be vertically aligned with LFM2	✓
8	LFA1	Left forearm cluster marker 1	✗
9	LFA2	Left forearm cluster marker 2	✗
10	LFA3	Left forearm cluster marker 3	✗
11	LFM1	Lateral aspect of the 1st metatarsal head of the left foot	✓
12	LFM2	Dorsal aspect of the 2nd metatarsal head of the left foot. Calcaneus marker should be vertically aligned	✗
13	LFM5	Lateral aspect of the 5th metatarsal head of the left foot	✓
14	LHEAD	Above the left ear centre	✓
15	LLA	Prominence of the left lateral Malleolus	✓
16	LLELB	Lateral Epicondyle of the Left Humerus	✓
17	LLH	Lateral portion of the 2nd metatarsal head of the left hand	✓
18	LLK	Lateral Epicondyle of the Left Femur	✓
19	LMA	Prominence of the left medial Malleolus	✓
20	LMELB	Medial Epicondyle of the Left Humerus	✓
21	LMH	Medial portion of the 5th metatarsal head of the left hand	✓
22	LMK	Lateral Epicondyle of the Left Femur	✓
23	LPSIS	Left Posterior Superior Iliac Spine	✓
24	LRAD	Left Radio-Styloid Process	✓
25	LSHIN	In front of the left shin	✗
26	LSHOULDERBACK	Over the left scapula	✗
27	LSK1	Left shank cluster marker 1	✗
28	LSK2	Left shank cluster marker 2	✗
29	LSK3	Left shank cluster marker 3	✗
30	LTH1	On the left thigh, above the kneecap	✗

31	LTROC	Left Trochanter	✗
32	LUA1	Laterally on the left arm, between the biceps and the triceps	✗
33	LULN	Left Ulna-Styloid Process	✓
34	RAC	Right acromial edge of the scapula	✓
35	RASIS	Right Anterior Superior Iliac Spine	✓
36	RBACK	Right mid-distance between the scapula and pelvis	✗
37	RCA	Distal end of the posterior aspect of the right Calcaneus. Should be vertically aligned with RFM2	✓
38	RFA1	Right forearm cluster marker 1	✗
39	RFA2	Right forearm cluster marker 2	✗
40	RFA3	Right forearm cluster marker 3	✗
41	RFM1	Lateral aspect of the 1st metatarsal head of the right foot	✓
42	RFM2	Dorsal aspect of the 2nd metatarsal head of the right foot. Calcaneus marker should be vertically aligned	✗
43	RFM5	Lateral aspect of the 5th metatarsal head of the right foot	✓
44	RHEAD	Above the right ear centre	✓
45	RLA	Prominence of the right lateral Malleolus	✓
46	RLELB	Lateral Epicondyle of the Right Humerus	✓
47	RLH	Lateral portion of the 2nd metatarsal head of the right hand	✓
48	RLK	Lateral Epicondyle of the Right Femur	✓
49	RMA	Prominence of the right medial Malleolus	✓
50	RMELB	Medial Epicondyle of the Right Humerus	✓
51	RMH	Lateral portion of the 5th metatarsal head of the right hand	✓
52	RMK	Medial Epicondyle of the Right Femur	✓
53	RPSIS	Right Posterior Superior Iliac Spine	✓
54	RRAD	Right Radio-Styloid Process	✓
55	RSHIN	In front of the right shin	✗
56	RSHOULDERBACK	Over the right scapula	✗
57	RSK1	Right shank cluster marker 1	✗
58	RSK2	Right shank cluster marker 2	✗
59	RSK3	Right shank cluster marker 3	✗
60	RTH1	On the right thigh, above the kneecap	✗
61	RTROC	Right Trochanter	✗
62	RUA1	Laterally on the right arm, between the biceps and the triceps	✗
63	RULN	Right Ulna-Styloid Process	✓
64	ST1	Sternum cluster marker 1	✓
65	ST2	Sternum cluster marker 2	✗
66	ST3	Sternum cluster marker 3	✗

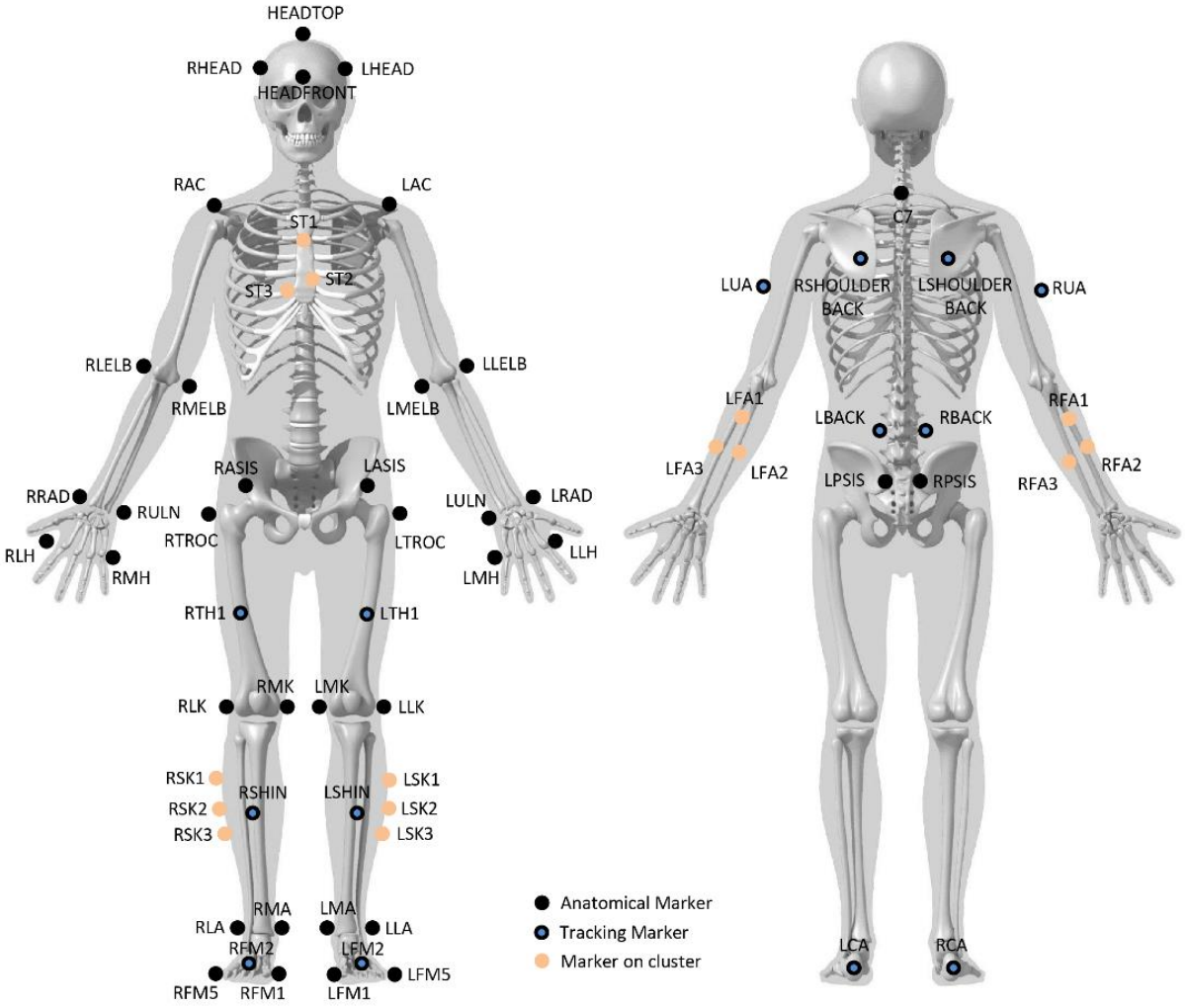

Figure A-1: Anterior and posterior view of the human skeleton. Location of the sixty-six markers placed on the subject's skin.

Appendix B: LABIOMEP-UP Layout

The schematic of the Porto Biomechanics Laboratory (LABIOMEP-UP) layout, shown in Figure 5-1, is as follows.

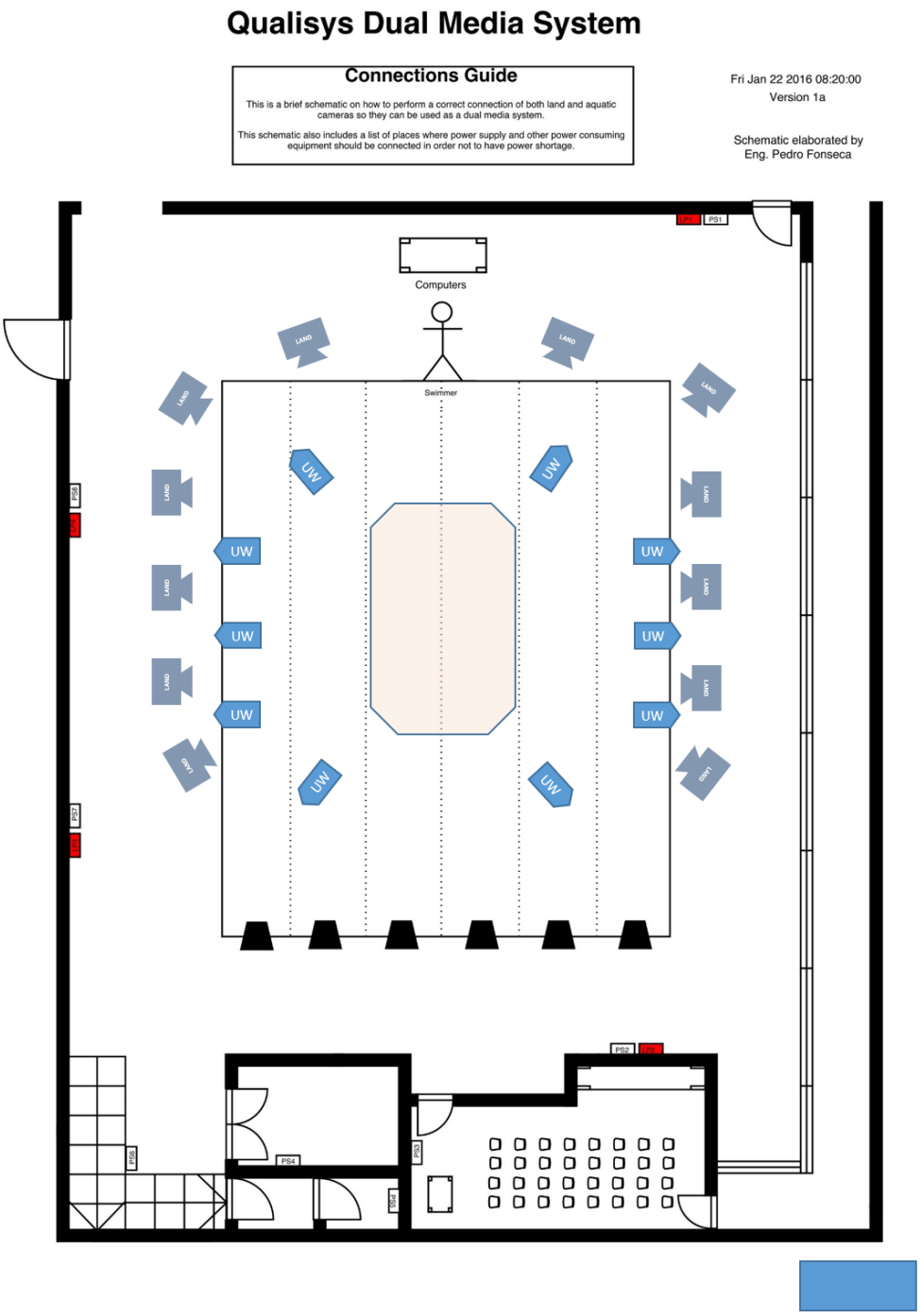

Figure B-1: Top view overall configuration of the LABIOMEP-UP layout. UW stands for underwater cameras, and LAND stands for above water cameras. The coloured rectangle in the centre of the swimming pool corresponds to the calibrated volume covered by the 22 cameras.

Appendix C: Swumsuit Input Data Files Format

The format of the body geometry, joint motion, analysis settings, and linear and angular velocities input data files of the simulation program Swumsuit, respectively denominated as `body_geometry.dat`, `joint_motion.dat`, `analysis_settings.dat`, `input_vgx.dat`, `input_vgy.dat`, `input_vgz.dat`, `input_ome1.dat`, `input_ome2.dat`, and `input_ome3.dat`, is described next. All data files are in written in DAT format.

Note that the joint motion, and linear and angular velocities data files are written for one single stroke cycle, even if the number of cycles set in the analysis settings data file is greater than one.

Body geometry data file: `body_geometry.dat`

Table C-1: Format of body geometry data file.

1	Root depth of body segment 1	Root width	Tip depth	Tip width	Length	Density
2	Root depth of body segment 2	Root width	Tip depth	Tip width	Length	Density
:	(repeat for all bodies)					
21	Root depth of body segment 21	Root width	Tip depth	Tip width	Length	Density
22	Distance between shoulder joint and upper arm's root in y_b direction					
23	Distance between shoulder joint and upper arm's root in z_b direction					
24	Distance between neck's tip and head's root in x_b direction					
25	Distance between lower hip's tip and hip joint in y_b direction					
26	Distance between lower hip's tip and hip joint in z_b direction					
27	Distance between shank's tip and foot joint in z_b direction					
28	Rotating angle of upper and lower hip parts [rad]					
29	Subject's height [m]					
30	Subject's weight [kg]					

All quantities are nondimensionalised by the subject's height, except the data in lines 28 to 30 (i.e., the rotating angle of upper and lower hip parts, and the subject's height and weight). The x_b, y_b, and z_b directions correspond to the base coordinate system direction axes described in Section 6.2.2.

Nakashima et al. (2007) measured the widths and depths of the root and tip of the body segments and the body lengths from captured images of frontal and sagittal views of a swimmer subject male at age 20-29 years old, with 1.705 m height, and 64.9 kg weight. Since the geometric data was scaled by the subject's stature, the same dataset was used in this work by adjusting it to the swimmer's anthropometry under analysis (male subject at the age of 25 years old, with weight 70.3 kg, and 1.80 m height). By

doing so, it is assumed that both subjects belong to the same percentile, which is a reasonable assumption (Dumas et al., 2007a). The order of the bodies in SWUM is as described in Section 6.2.1.

Table C-2: Body geometry data.

1	0.064633	0.084696	0.060020	0.078768	0.035308	1.072631
2	0.060020	0.078768	0.071138	0.084677	0.071847	1.783209
3	0.071138	0.084677	0.082255	0.090587	0.071847	0.453868
4	0.082255	0.090587	0.058592	0.113724	0.065689	0.336663
5	0.058592	0.113724	0.040660	0.040660	0.031202	1.964305
6	0.040660	0.040660	0.033903	0.033903	0.016422	2.246407
7	0.041393	0.040572	0.055191	0.048686	0.139062	0.725793
8	0.064640	0.084691	0.065402	0.105926	0.054417	0.928367
9	0.065402	0.105926	0.050020	0.100030	0.074896	0.666456
10	0.050015	0.050015	0.034428	0.032959	0.187566	1.009118
11	0.050015	0.050015	0.034428	0.032959	0.187566	1.009118
12	0.034428	0.032959	0.020359	0.020359	0.180938	1.346060
13	0.034428	0.032959	0.020359	0.020359	0.180938	1.346060
14	0.037848	0.020359	0.010698	0.028241	0.137193	0.303078
15	0.037848	0.020359	0.010698	0.028241	0.137193	0.303078
16	0.026034	0.026034	0.023355	0.023355	0.186628	0.808331
17	0.026034	0.026034	0.023355	0.023355	0.186628	0.808331
18	0.023355	0.023355	0.011965	0.018005	0.151320	1.002346
19	0.023355	0.023355	0.011965	0.018005	0.151320	1.002346
20	0.011965	0.029413	0.004106	0.015015	0.107331	1.032411
21	0.011965	0.029413	0.004106	0.015015	0.107331	1.032411
22	-0.00779373233					
23	0.0131378299					
24	0.00599197012					
25	0.0500147909					
26	0.068856305					
27	0.0374193548					
28	0.0140119644					
29	1.80					
30	70.3					

Joint motion data file: `joint_motion.dat`

The relative body motion in SWUM is given as rotations of body segments about joints, described in the respective body coordinate system ($O_b - x_b y_b z_b$). Although SWUM does not have an explicit articular system, each coordinate system is located at the proximal extremity of each body segment.

Table C-3: Format of the joint motion data file.

Total number of frames in one cycle	
ID of the rotating body	Index of the rotating axis
Angle on the 1st frame	
Angle on the 2nd frame	
:	
(repeat for all frames)	
:	
Angle on the last frame	
ID of the next rotating body	Index of the next rotating axis
Angle on the 1st frame	
Angle on the 2nd frame	
:	
(repeat for all frames)	
:	
Angle on the last frame	
:	
Angle on the last frame for the last rotation	
0 0	

All angles in the joint motion data file are given in degrees. The ID of the rotating body segments is the same as in the body geometry data file. The indices of the rotating axes are: 1 (x_b axis), 2 (y_b axis), 3 (z_b axis), 4 (x_b axis right shoulder elevation), 5 (y_b axis right shoulder elevation), 6 (z_b axis right shoulder elevation), 7 (x_b axis left shoulder elevation), 8 (y_b axis left shoulder elevation), and 9 (z_b axis left shoulder elevation).

Note that each rotation is performed in the same order in which it is written in this file. Besides, the rotation angles are not relative but absolute, meaning that the rotation of a body segment about a given axis does not affect the adjacent bodies. Consequently, to rotate the subsequent body segment(s) for the same angle, the same rotation must be given to the latter.

Analysis settings data file: `analysis_settings.dat`

The analysis settings data file consists in a free format list of names of analysis parameters and respective values. Changes in the order of the parameters do not interfere with the interpretation of the data file. However, the name of the parameter must be consistent with that established in the software program. For that, a standard six-beat front crawl swimming stroke simulation performed by Nakashima et al. (2007) is available in the software web page. The folder includes the input data files and output data, so it can be consulted as an example.

Table C-4: Format of the analysis settings data file.

Name of the parameter=
Value of the parameter
:
(repeat for all analysis parameters)
:

Linear and angular velocity data files: `input_vgx.dat`, `input_vgy.dat`, `input_vgz.dat`, `input_ome1.dat`, `input_ome2.dat`, `input_ome3.dat`

The swimmer's absolute motion captured in LABIOMEP-UP, and processed by a kinematic analysis method, is given as input to the simulation. The whole-body centre of mass (COM) and principal axes of inertia are respectively fixed to the lower tip of the lower waist segment, which corresponds to the pelvis in the LHBM, and to the body coordinate system ($O_b - x_b y_b z_b$). Each file is written separately in the absolute coordinate system ($O - xyz$) for the x, y, and z linear velocities, while the angular velocities are written in the body coordinate system, $O_b - x_b y_b z_b$.

Table C-5: Format of the linear and angular velocities data files.

Linear/Angular velocity of the whole body's COM on the 1st frame
:
(repeat for all frames)
:
Linear/Angular velocity of the whole body's COM on the last frame

The linear velocities at each instant of time are given in m/s, while the angular velocities are given in deg/s.